UNIVERSITY OF CALGARY

Study of the Methane Chemical Looping Combustion Process Using Supported Metal Carriers for Carbon Capture

by

Mansour Mohammedramadan Ahmed A. Tijani

A THESIS

SUBMITTED TO THE FACULTY OF GRADUATE STUDIES

IN PARTIAL FULFILMENT OF THE REQUIREMENTS FOR THE

DEGREE OF DOCTOR OF PHILOSOPHY

GRADUATE PROGRAM IN CHEMICAL AND PETROLEUM ENGINEERING

CALGARY, ALBERTA

AUGUST, 2018

Abstract

Global warming caused by greenhouse gases (GHGs) has in the recent years become a great concern internationally. Recent changes in weather patterns can be attributed as one of the possible results of global warming. The emission portion of carbon dioxide (CO_2) is one of the highest among the GHGs. Accordingly, carbon capture technology is needed to decrease CO_2 emission to the atmosphere. The Chemical Looping Combustion (CLC) process is an alternative and immature process to capture CO_2. This process produces a concentrated stream of CO_2 that does not require any further expensive separation unit.

To commercialize this technology, this thesis presents a comprehensive study of the methane CLC process using supported mixed metals oxygen carriers. In the first part of the study, synthesis and reactivity evaluation of monometallic carriers were conducted, assessing and discussing the effect of various operating conditions on reactivity. Interaction between monometallic precursors (Ni & Co) and alumina support was observed, resulting in forming intermediate phases such as $CoAl_2O_4$ and $NiAl_2O_4$; the $CoAl_2O_4$ phase was successfully reduced but the $NiAl_2O_4$ did not reduce. By varying the temperature (800°C-950°C), the highest observable oxygen capacity for all 16 samples was found to be between 900°C and 950°C.

In the second part of the study, optimum operating conditions obtained previously were applied to the supported bimetallic carriers, leading to novel findings. The redox reactions pathways were determined, with a main conclusion being that once the chemical stability between precursors and supports maximized, negligible interaction could be anticipated. The Ni-Co/ZrO_2, Ni-Cu/ZrO_2, and Ni-Fe/ZrO_2 samples showed stable oxygen capacities compared to others and negligible interaction between precursors and supports.

In the last part of the study, Aspen Plus computer software was used to examine the feasibility and sustainability of the process. It was found that the loading percentage of precursor (Ni-Cu/ZrO_2) showed no significant effect on conversion in the fuel reactor, but conversion increased by 39% in the air reactor. Finally, the case study was compared with other competing processes. The overall efficiency of the case study was found to be higher than that of the competing processes, suggesting its potential for commercialization.

Preface

This thesis is a result of my strong passion for education. It all started with being pragmatic and objective about a problem we all face every day. Growing energy demand worldwide has put us in a situation where we unintentionally harm our beautiful planet. Damage done to the environment varies from plastic products found in oceans to emission of hurtful gases to the atmosphere and foundation of toxic landfills. How will we mitigate or eliminate these bad actions? It is my duty as a human being to contribute and be an activist toward addressing these hurtful actions to our planet. It is my duty to develop and demonstrate good actions without compromising our energy needs.

Honestly, I would not be able to present my work without thanking first and foremost Allah, then my parents (Aisha Mohammed Ali, and Mohammedramadan Ahmed Tijani) who brought me to this life, raised, and took care of me. I am truly thankful to all individuals who helped and motivated me throughout my BSc, MSc, and PhD journeys. Thank you all.

Acknowledgements

Oh boy! I will need another thesis to acknowledge all and everyone but I will make it short.

I acknowledge Allah (SWT) for the health, motivation, and blessings He gives me every day and every time I breathe. I always thank Allah (SWT) for the guidance in every step and decision I take in my life. I obey Him and his messenger, Prophet Mohammed Ibn Abdul Mutalib (peace and blessings be upon him).

Throughout my PhD study at the University of Calgary, Canada, many individuals deserve appreciation and thanks for their role of supporting, motivating assisting, and providing valuable feedback. It is with my gratitude pleasure to acknowledge:

- My supervisor Professor Nader Mahinpey for accepting me as a PhD student. Professor Mahinpey, there are no words to describe my grateful appreciation of your guidance, support and assistance throughout my studies. You gave me the opportunity to work under your supervision to advance my academic and engineering skills. Many thanks for your support, especially the last couple of months when I thought I would never finish my degree and that I would have to leave Canada empty handed. Thank you, Professor Mahinpey. I will always be your student.
- My co-supervisor Dr. Hector De la Hoz Siegler for his co-supervision, helpfulness, and assistance during my studies. All the good feedback and brilliant ideas received from Dr. Siegler are appreciated and acknowledged. Many thanks for the advice you gave me in the last couple of days of my thesis writing. Thanks for the encouragement you provided to overcome the hardship of completing my degree in Canada.

- My defense committee: Dr. Matthew Clarke, Dr. Hassan Hassanzadeh, Dr. Abdulmajeed Mohamad, and Dr. Jaafar Soltan Mohammadzadeh for agreeing to be on my PhD defense committee at short notice. Thank you all for your valuable feedback that I will take toward my future career.
- Dr. Robin Yates from the Faculty of Graduate Studies (FGS) for his advice and assistance, especially when my situation got really complicated and I thought I would not be able to finish my PhD degree in Canada. Thank you so much, Dr. Yates. I really appreciate your support and that the fact FGS facilitated and helped all impacted Saudi students.
- Dr. Aqsha for his support and help during my PhD studies. I really appreciate your patience, motivation, and unlimited guidance.
- Dr. Lakshmi Katta for her training and advice during my early days in the lab. I truly appreciate your valuable input toward my research.
- Mr. William Hatherell for providing suggestions and respected feedback toward the grammar and language used in this thesis.
- All my teachers throughout my BSc, MSc, and PhD studies for their efforts, moral support and their interaction with me.
- The Energy and Environment Research Group (EERG) members: Dr. Davood Karami, Dr. Ehsan Mostafavi, Dr. Mahesh Nair, Negar Manafi, Amir Hassan Soleimani Salim, Yusuke Uehara, Toufigh Bararpour, Seyed Mojtaba Hashemi, Amr Abdalla, Nima Khakpour, Ningyu Yu, Pradeep Shresta, Xueqin (Amy) Wu, Chenxu (David) Shi, Camilla Fernandes de Oliveira, Babak Labbaf, Moheddin Mohamed Elgarni, and Garima Jain for creating a fun and motivated research environment. I wish the best of luck to you all.

- The graduate office at the Schulich School of Engineering led by Dr. Matthew Clarke. Especial thanks to Mr. Arthur De Vera, and Ms. Suha Abusalim for their assistance.
- The internship students I mentored and trained: Tommy Chu, Steve Lee, Alan Kim, Jun Daniel Jeong, Tristan Hannequin, and Marion Vaussy.
- Dr. Gerardo Vitale Rojas, and Dr. Azfar Hassan for providing assistance with the XRD and H_2-TPR analysis.
- Our industrial partners who provided financial support: The Natural Sciences and Engineering Research Council (NSERC) of Canada ─ Industrial Research Chairs (IRC) program, Canadian Natural Resources Limited (CNRL), and Devon Energy Corporation Canada.
- Last but not the least, I would like to thank everyone who helped me that I have not previously mentioned by name, especially those who motivated me during the course of writing my PhD thesis.

Dedication

I dedicate this thesis to my beloved parents (Aisha Moahmmed Ali, and Mohammedramadan Ahmed Tijani), future wife, kids, and grandkids

Table of Contents

List of Tables

List of Figures and Illustrations

List of Symbols, Abbreviations and Nomenclature

Symbol	Definition
A	Adsorption coefficients, [-]
$A_{i,x}$	Cross-sectional area of AR, [m^2]
B	Adsorption coefficients, [-]
C	Adsorption coefficients, [-]
C_i	Concentration, [mol/m^3]
D	Adsorption coefficients, [-]
d_p	Particle diameter, [m]
E_A	Activation energy, [kJ/mol]
f(X)	Conversion dependent function
g	Gravity acceleration, [m/s^2]
G(X)	Conversion dependent function
H_i	Heating value, [J/kg]
h_k	Bed height, [m]
ΔH_o	Enthalpy of oxidation reaction, [J]
ΔH_r	Enthalpy of reduction reaction, [J]
k_0	Frequency factor, [$mol^{1-n}\,g^{n-2}/min$]
k	Oxygen de-attachment factor, [-]
k	Reaction rate constant, [$mol^{1-n}\,g^{n-2}/min$]
K_i	Equilibrium constant, [m^3/mol]
k_{SCM}	Shrinking core model reaction rate constant, [$mol^{1-n}\,g^{n-2}/min$]
M	Molar mass, [kg/kmol]
$\dot{m}$	Mass flow rate, [kg/s]
n	Reaction order, [-]
P	Pressure, [bar]
P_x	Fuel power, [W]
ΔP_k	Pressure drop across the reactor, [bar]

r	Reaction rate, [mol/g*min]
R	Universal gas constant, [J/mol K]
R_r	Recirculation ratio of total gas fed to FR and fuel flow, [-]
Re	Reynold's number, [-]
S_r	Stoichiometric ratio of oxygen to fuel, [-]
T_0	Reference temperature, [K]
T_a	Ambient temperature, [K]
T	Absolute temperature, [K]
t	Time, [min]
u_{ix}	Gas velocity, [m/s]
W_k	Solid inventories, [kg]
W_O	Weight of de-attached oxygen, [g]
$W_{O.O.C}$	Weight of fully oxidized oxygen carrier, [g]
X	Conversion, [-]
y_i	Molar fraction, [-]

Subscripts *(x)*

Symbol	**Definition**
a	Parameter in Redlich-Kwong equation, [-]
b	Parameter in Redlich-Kwong equation, [-]
c	carrier
g	gas
i	i^{th} component
m	number of atoms
m	mass of oxygen carrier sample
mf	minimum fluidization
n	number of atoms
o	oxidized
r	reduced
s	solid

x	number of atoms
y	number of atoms
z	number of atoms

Abbreviations

Symbol	**Definition**
AR	Air Reactor
Al_2O_3	Aluminum Oxide
BET	Brunauer–Emmett–Teller theory
C	Carbon
CCPP	Combined Cycle Power Plant
CeO_2	Cerium Oxide
CLC	Chemical Looping Combustion
Co	Cobalt
Cu	Copper
DFT	Density Functional Theory
Fe	Iron
FR	Fuel Reactor
H	Hydrogen
H_2-TPR	Hydrogen Temperature Programmed Reduction
Me	Metal-based oxygen carrier
MeO	Metal oxide-based carrier
Ni	Nickel
O	Oxygen
OC	Oxygen Carrier
PC	Pulverized Coal
TGA	Thermogravimetric Analyzer
TiO_2	Titanium Oxide
XRD	X-Ray Diffraction
ZrO_2	Zirconium Oxide

Greek letters

ε_{mf}	Voidage at minimum fluidization velocity, [-]
η	Effectiveness factor, [-]
η_c	Efficiency of combustion, [-]
η_o	Efficiency of oxidation, [-]
λ	Air ratio, [-]
μ	Dynamic viscosity of fluidizing fluid, [kg/m·s]
Ψ	Solid particle sphericity, [-]
ρ	Density, [kg/m^3]

CHAPTER ONE: INTRODUCTION

1.1. Overview

Global warming caused by greenhouse gas (GHG) emissions has as of late become a great concern for many. Recent changes in weather patterns can be attributed as one of the possible results of global warming. Greenhouse gases, including carbon dioxide (CO_2), methane (CH_4), water vapour (H_2O), ozone (O_3), nitrogen oxides (NOx) and fluorinated gases (F-gases), are directly tied to global warming as a result of their increasing concentrations in the atmosphere [1]. Carbon dioxide (CO_2) is the highest (~64.3%) contributor to GHG emissions [2], [3]. This is due in part to industrialization that initially developed in the late 18^{th} century, which in turn boosted agricultural output and fossil fuel consumption [4].

Historically, CO_2 concentrations in the atmosphere have been steadily increasing over the past 60 years [5]. CO_2 concentrations have increased from 277 ppm in 1700 to 408.71 ppm in mid-2018 [6], [7], that is a 47.55% increase. Cautious estimates predict that CO_2 concentrations will continue to increase in the future [8]. Fig. 1.1 shows the projected climb of CO_2 concentrations in the atmosphere up until the year of 2100. Both the Bern-CC and ISAM models estimate CO_2 concentrations based on the Intergovernmental Panel on Climate Change (IPCC) scenarios data, as shown in Fig. 1.1a (IS92a, [8]). As can be seen, the Bern-CC model (Fig. 1.1b), which accounts for bounding assumptions, shows a projected CO_2 concentration range of between 890 ppm and 610 ppm in 2100. That is an increase of between 118.7% and 49.9% increase over today's atmospheric CO_2 concentration (407 ppm). The ISAM model (Fig. 1.1c), however, shows a projected CO_2 concentration of between 800 and 640 ppm in 2100, which is an increase of between 96.6% and 57.2% over today's atmospheric CO_2 concentration.

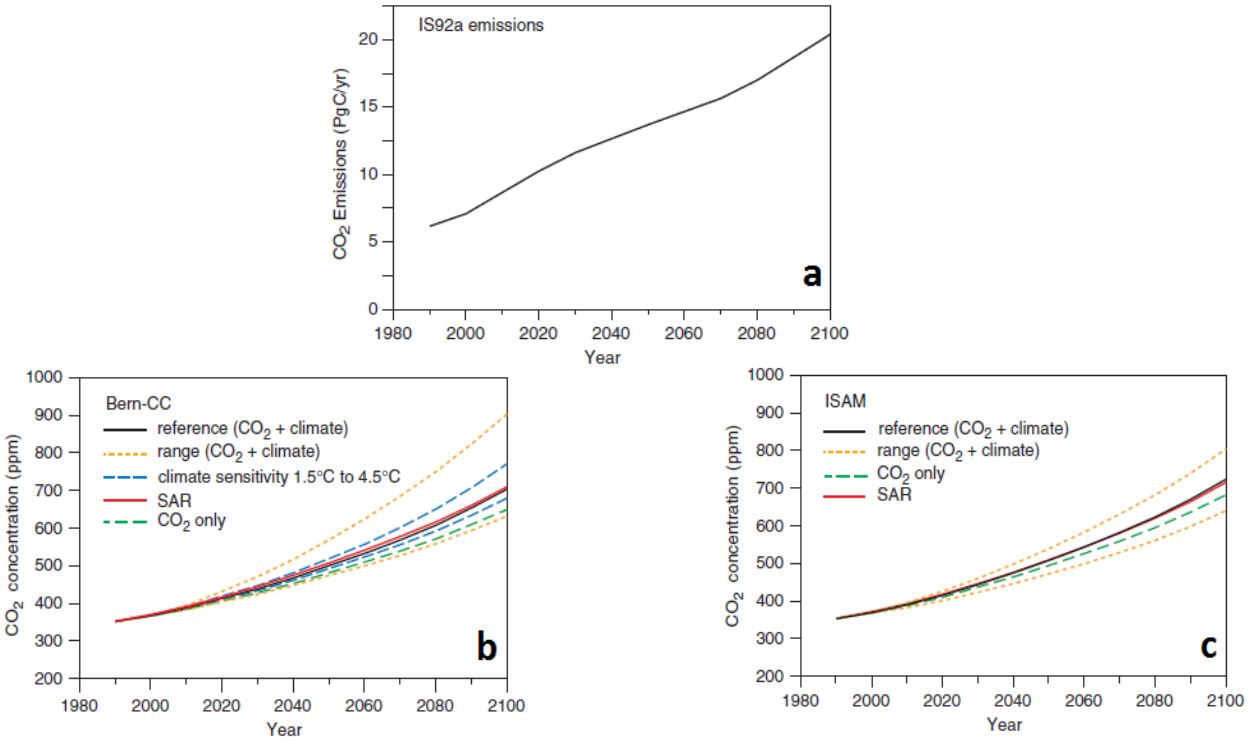

Fig. 1.1. CO_2 concentration growth in the atmosphere: a) IS92a emission trend, b) Bern-CC model, c) ISAM model, [9].

In fossil fuel power plants, there are three ways to capture CO_2: pre-combustion, post-combustion, and oxy-fuel [10]. Pre-combustion CO_2 capture separates CO_2 and H_2 gases from the produced syngas before combusting the H_2-rich gas in a turbine to generate electricity. The temperature utilized in the pre-combustion CO_2 capture process is highly dependent on the sorbents; for example, Zeolite is used for temperatures below 200°C, Layered Double Hydroxides (LDH) for temperatures 200–400 °C, and calcium-based sorbents for temperatures higher than 400°C [11], [12]. Hence, sorbents play an important role. They either react with or dissolve CO_2 [13]; therefore, when the temperature is increased in the re-generation unit, the CO_2 gas is released by the sorbents. Examples of sorbents used in this process include amines, calcium and limestone. The pre-combustion process reduces overall efficiency anywhere between 6.5 and 8.6 % [14], a

reduction that has triggered research into lowering energy consumption through means such as sorbents development, high pressure H_2/CO_2 separation membranes, and heat recovery [15]. An example of a widely used pre-combustion process is the Integrated Gasification Combined Cycle technology (IGCC), which can produce electricity from either liquid or solid fuels.

In the post-combustion process, CO_2 is captured from flue gases at atmospheric pressure and temperatures usually lower than 80°C [16]. Sorbents, in this case, are divided into physisorbents and chemisorbents. Physiosorbents (also called physical sorbents) are materials that form a weak Van der Waals force to bond sorbents and sorbates without causing perturbation to the molecules [17]. Physiosorbents are usually porous materials that reduce the free energy of CO_2 molecules. Physiosorbents drive CO_2 molecules from the gas-bulk to attach inside the sorbents' pores [18]. Chemiosorbents (also called chemical sorbents) are materials that react with sorbates to form chemical bonds [17]. They follow the same mechanism as physiosorbents, except for forming strong chemical bonds between the CO_2 molecules and the internal surface of the chemiosorbents [18]. Regeneration of these sorbents usually occurs at temperatures higher than 100°C in order to recover the adsorbed CO_2 gas [19]. Examples of physiosorbents and chemiosorbents are microporous polymers and amino acids, respectively. Post-combustion CO_2 capture accounts for approximately 70–80% of the total cost of carbon capture and storage [20]. This is because of the cost of the sorbent regeneration process. Many researchers have investigated cost-effective sorbents in order to reduce this regeneration cost [20], [21]. The most widely used post-combustion CO_2-capture technology is the Monoethanolamine (MEA) process. Although this process has been adopted by many companies such as KBR Inc. Texas (a construction company) and Alstom France (a transport company), it is still costly in terms of regenerating the aqueous amine solution as well as being toxic to the environment once it starts degrading into nitrosamines and nitramines [22].

Finally, the oxy-fuel CO_2-capture technique involves oxy-fuel combustion (short name for oxygen fuel combustion) in which a fuel such as natural gas is burned in a pure oxygen environment. This process not only eliminates nitrogen oxides (NOx) and other pollutants but also reduces the fuel consumption rate, as well as increasing the flame temperature [23]. Chemical Looping Combustion (CLC) uses solid oxygen carriers and is an example of an oxy-fuel combustion process that has the potential to become a cost-effective, efficient and clean technology.

The CLC process produces a concentrated stream of CO_2 due to the combustion of fuel with pure oxygen. This process usually consists of a packed-bed reactor or interconnected fluidized-bed reactors (Fig. 1.2). The concept of using a fluidized-bed reactor for CLC was initially suggested by Lyngfelt, *et al* in 2001 [24]. Since then, this approach has been the subject of extensive research, system analyses and reactor design [25]. In the fluidized-bed system, the first reactor is called the "air reactor", where the solid oxygen carriers are in contact with air in order to adsorb oxygen (oxidation). These carriers are then transferred to the second reactor, known as the "fuel reactor", where combustion of solid, liquid or gas fuels occurs. The combustion of fuel occurs in a pure oxygen environment. The reason for combusting fuel in pure oxygen is to stop the formation of gases such NOx, as those gases make the CO_2 separation process expensive and difficult. The products of this process are usually water and CO_2. They can be separated by reducing the gas temperature below 100°C "condensation". Additional units are sometimes required, such as a gasifier/water gas shift (WGS) unit when solid fuels (biomass or coal) are used [26].

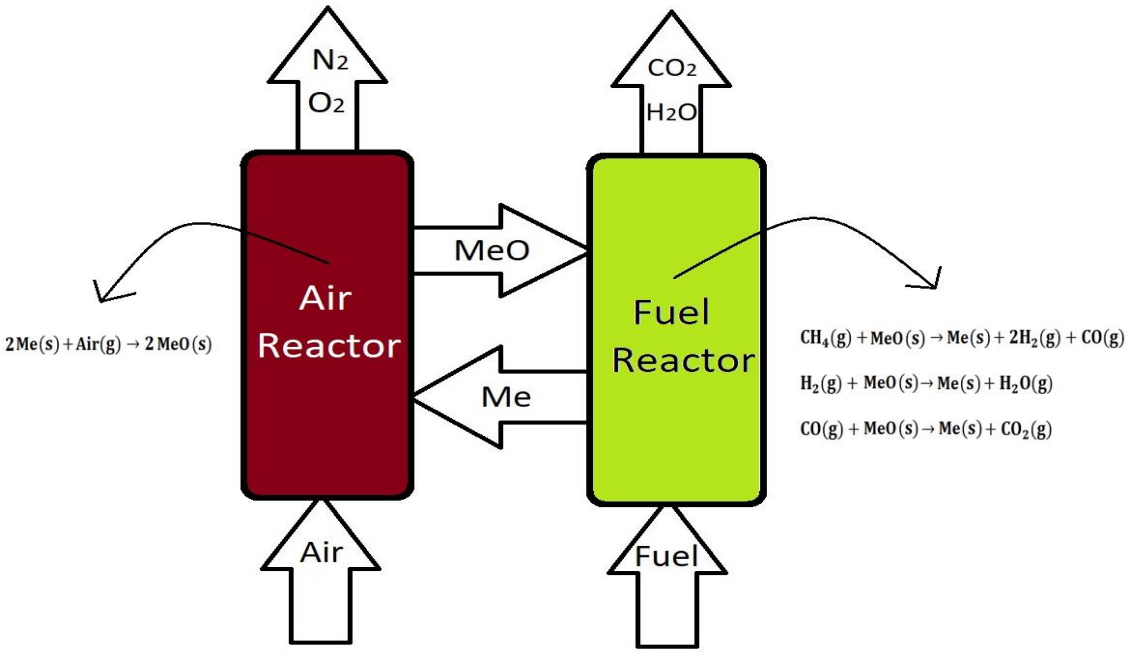

Fig. 1.2. Typical CLC technique using solid oxygen carriers in two interconnected fluidized-bed reactors.

Oxygen carriers play a crucial role in the CLC system. They are required to ensure very high reactivity and stability during the CLC oxidation/reduction cycles. For example, oxidation in the AR and reduction in the FR of a novel oxygen carrier should be fast with short residence times in order to achieve a high fuel conversion rate. The most widely used oxygen carriers in the past decade are metal-based oxides materials. These materials are not only cheap and easy to fabricate, but also have resistance to attrition and good fluidization properties [26].

In spite of the large number of studies on CLC processes, the commercialization success of the CLC process is limited due to some vital challenges related to the science and role of the oxygen carriers: specifically, the kinetics of restructuring the active sites on different supports, the effect of oxygen carriers' structure on the reaction rate, the synthesis energy effect of oxygen carriers on the oxidation/reduction reactions, the effect of the phase changes of metal on the

reactivity and reaction kinetics, and the determination of governing pathways of oxidation/reduction reactions for mixed oxides oxygen carriers. Investigation of the reaction rate and the intrinsic and global kinetics of the transition metals (Cu, Fe, Ni, Co) that deposit on supports (Al_2O_3, CeO_2, TiO_2, ZrO_2) is needed to tackle these challenges.

1.2. Literature review

1.2.1. Chemical Looping Combustion (CLC)

Chemical looping combustion was introduced as a means of reducing the greenhouse gases effect (i.e. CO_2 emission) [23]. It was chosen among others because of its potential to reduce the cost of the CO_2-capture process by 50% [27]. In the CLC process, a solid oxygen carrier is oxidized at high temperatures inside a reactor called the "air reactor". The reactants are the air and oxygen carrier. The oxygen carrier is then transferred to the fuel reactor. In the case of fixed-bed reactors, it is exposed to the fuel. Conversion of fuel and reduction of the oxygen carrier are then carried out. The process is then repeated in multiple cycles (i.e. oxidation/reduction reactions). The following reactions describe the general CLC process.

$$(OC)_r + Air \rightarrow (OC)_o \; ; \quad \Delta H_o \tag{1.1}$$

$$(OC)_o + Fuel \rightarrow CO_2 + H_2O + (OC)_r \; ; \quad \Delta H_r \tag{1.2}$$

where:

OC: Oxygen Carrier

ΔH_o enthalpy of oxidation reaction (J).

ΔH_r enthalpy of reduction reaction (J).

r & o subscripts: reduced and oxidized, respectively.

The combustion process can be carried out using either a gaseous or a solid fuel. CLC of both types of fuel is explained in the following two sections.

1.2.1.1. *CLC of gaseous fuels*

This process is used to separate CO_2 from N_2 when gaseous fuel is combusted. The oxygen reacts with the gaseous fuel to produce mainly CO_2 and H_2O. After the condensation of H_2O, a highly concentrated stream of CO_2 can be obtained. This process reduces the penalties (heat loss and CO_2 capture/separation unit) that are usually associated with the combustion of gaseous fuel in an air environment [28]. The global equations that describe this process are as follows:

Oxidation reaction:

$$\left(\frac{2n+m}{z}\right) Me_xO_{y-z} + \left(n+\frac{m}{2}\right) O_2 \rightarrow \left(\frac{2n+m}{z}\right) Me_xO_y \; ; \Delta H_o (J) \tag{1.3}$$

Reduction reaction:

$$\left(\frac{2n+m}{z}\right) Me_xO_y + C_nH_{2m} \rightarrow \left(\frac{2n+m}{z}\right) Me_xO_{y-z} + \left(\frac{n}{z}\right) CO_2 + \left(\frac{m}{z}\right) H_2O \; ; \Delta H_r \; (J) \tag{1.4}$$

Overall reaction:

$$C_nH_{2m} + \left(n+\frac{m}{2}\right) O_2 \rightarrow n\, CO_2 + m\, H_2O; \Delta H_{ov.all}(J) = \Delta H_o + \Delta H_r \tag{1.5}$$

In order to investigate the CLC of gaseous fuels, two approaches can be considered: pilot-scale and lab-scale approaches.

1.2.1.1.1. Pilot-scale CLC of gaseous fuels

There are several different concepts pertaining to the design of reactors used for gaseous fueled chemical looping combustion. Fig. 1.3 shows some common reactor concepts that can be considered for a CLC process.

The rotating reactor concept (Fig. 1.3a) was proposed by Dahl *et al* in 2009. The feed gases are injected in the radial direction (blue section) [29]. The green grid represents the solid oxygen

carriers, which move from the air sector to the inert sector (steam), then to the fuel sector (CH_4), and finally return again to the inert sector. The main challenge of this reactor is the separation of gases (i.e. air and fuel), which was reported by Dahl *et al* [29]. The concept of a circulating fluidized-bed reactor for CLC was first proposed by Lyngfelt *et al* in 2001 (Fig. 1.3b) [24]. This reactor consists of a riser that functions as an air reactor and a bubbling fluidized-bed reactor which

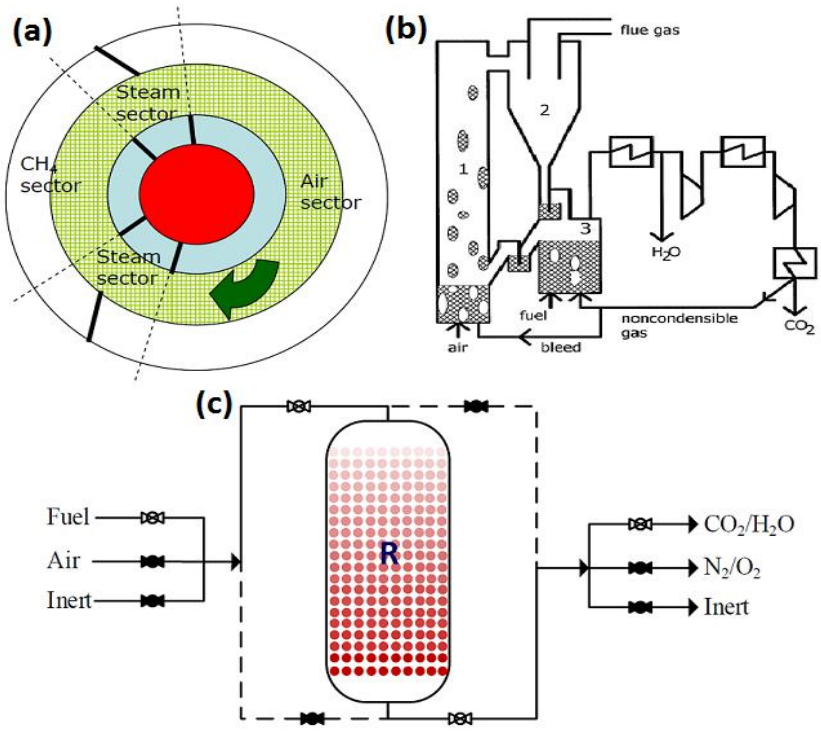

Fig. 1.3. Reactor concepts for gaseous fueled chemical looping combustion: a) rotating reactor [29], b) circulating fluidized-bed reactors [24], c) fixed-bed reactor [30].

makes up the fuel reactor. The riser must have a fast fluidization regime (i.e. particles' velocity ≥ terminal velocity) so that solid oxygen carrier particles can move upward to the fuel reactor. The main challenge facing the circulating fluidized-bed concept is finding oxygen carriers that have good fluidization properties (e.g. attrition, mechanical strength) as well as high reactivity

(oxidation and reduction rates). Another common concept is that of the fixed-bed reactor (Fig. 1.3c). In most cases, it consists of a single reactor packed with solid oxygen carriers. The gases are then switched between air and gaseous fuel, and as a result, the oxidation and reduction reactions of the oxygen carrier occur in the same reactor. The challenges facing the fixed-bed concept revolve around the pressure drop within the reactor and the regeneration of the oxygen carriers.

1.2.1.1.2. Lab-scale CLC of gaseous fuels

Semi-batch systems such as a thermogravimetric analyzer (TGA) are primarily used to study CLC processes using gaseous fuels. A TGA can be used in a small-scale experiment to study the oxidation and reduction reactions of a CLC process by recording weight loss versus time at different reaction temperatures and gas compositions. The reaction order, activation energy, and numerous other kinetics/behaviours can be estimated using the TGA instrument.

Donat *et al* studied different Cu-based oxygen carriers over the course of 100 cycles of oxidation and reduction reactions (800-950 °C) in a TGA, using air and H_2, CO as oxidizing and reducing gases, respectively [31]. The maximum oxygen capacity was found to be around 8.04 wt% (first cycle). Early reductions in the cyclic performance were also observed and attributed to the agglomeration of the support ($CaO\text{-}Al_2O_3$). Ksepko studied strontium cuprate ($SrCuO_2$) as an oxygen carrier in a TGA, with an oxygen capacity of 8.02 wt% reported at 800°C [32]. Wang *et al* proposed the use of Chinses sulfur-containing lean iron ore as an oxygen carrier for CLC and also studied the effect of temperature, gaseous fuel concentration and composition using a TGA [33]. The influence of temperature on CH_4 reduction was significant as a reaction temperature of 800°C showed a 22% conversion, while a temperature of 950°C resulted in a 95% conversion. As the CH_4 concentration increased from 50% to 100%, only modest increases in conversion were

observed (37-55 %); however, coke formation was only noticeable at 50% and 100% CH_4 concentrations. Monazam *et al* synthesized mixed metal oxides (CuO-Fe_2O_3/Al_2O_3) and examined them using CH_4-fueled CLC in a TGA at differing temperatures [34]. It was reported that as the temperature increased, so did the CH_4 conversion. The reduction of Cu-ferrite to Cu was found to be chemically controlled, while Cu- ferrite to Cu-Fe_3O_4 and Cu-Fe were found to be controlled by the nucleation and growth model. The activation energies for reductions of CuO-ferrite to Cu-ferrite, Cu-ferrite to Cu-Fe_3O_4 and, CuO-ferrite to Cu-Fe were around 55.32, 70 and 165 kJ/mol respectively. Mei *et al* studied four different types of manganese minerals using gaseous fuels (CH_4, CO, H_2) for their potential use in CLC [35]. Results showed that all four samples showed high reactivity when CO and H_2 fuels were used compared to CH_4. Then the four samples started losing their reactivity after the 10^{th} cycle, which was attributed to the reformation of particles and/or production of fine particles during the oxidation/reduction reactions.

A laboratory bench-scale reactor represents another approach to investigate the reactions/behaviours of the gaseous-fuelled CLC process. Zheng *et al* studied different combinations of Cu as an active site, as well as SiO_2 and Al_2O_3 supports for their capability to produce a high concentration stream of H_2 in a fixed-bed reactor (270 cm^3), reporting that a 95% conversion of H_2 was observed at 500°C [36]. The Cu with 36.1% loading was found to exhibit the highest oxygen capacity of 9%. Harper *et al* studied copper-based oxygen carriers in a packed-bed reactor at 400°C [37]. It was found that mixing different copper oxides and oxygen carriers in the fuel reactor at a ratio of 1:6 (Al_2O_3) could prevent the agglomeration between the active site (Cu) and inert support (Al_2O_3) in the solid particles. Zhu *et al* investigated the use of Fe_2O_3/Al_2O_3 (3:2) in a newly proposed configuration of a CLC-packed-bed reactor at 850°C [38]. High concentrations of H_2 (95 vol.%) were achieved after 20 cycles of oxidation/reduction reactions.

Hamers *et al* examined the effect of pressure (2-7.5 bar at 600°C) on the performance of the $NiO/CaAl_2O_4$ oxygen carrier in a packed-bed reactor [39]. It was concluded that changes in pressure have a small effect on the outlet molar fractions of O_2 and H_2, which were observed in both oxidation and reduction cycles (8.75% and 12.5%, respectively). Song *et al* investigated the effect of temperature, gas flow rate, initial sample weight and particle size on a novel $CaSO_4$ oxygen carrier for methane combustion [40]. It was found that a reaction temperature of 950°C showed the highest methane reduction rate with 0.4-0.6 mm average particle size of $CaSO_4$. The 90 g initial weight of $CaSO_4$ showed a 28.6% higher conversion rate of CH_4 as well as a 21.4% higher conversion for CH_4 with a flow rate of 50 ml/min.

1.2.1.2. *CLC of solid fuels*

Solid fuels can also be utilized in chemical looping combustion processes as a means of producing a pure stream of CO_2. There are three approaches to process solid fuels: ex-situ gasification CLC, in-situ gasification CLC, and Chemical Looping with Oxygen Uncoupled (CLOU).

Ex-situ gasification CLC (Fig. 1.4a) consists of a gasification reactor that is attached to the CLC system in order to process the solid fuels. The solid fuel, such as coal, biomass or pet-coke, is first fed into the gasifier and allowed to react with nitrogen-free gasifying agents such as O_2 or steam. The gasification produces syngas (H_2, CO, CO_2) and ash. The syngas is then combusted in the fuel reactor of a CLC system. In-situ gasification/CLC (Fig. 1.4b), on the other hand, is when the gasification reaction occurs inside the CLC system, specifically within the fuel reactor. The solid fuel, as well as the gasifying agent (i.e. stream), is first fed into the fuel reactor in the presence of a solid oxidized oxygen carrier. The solid fuel is then gasified in the presence of a gasifying

agent, producing volatile matters, char and, steam. At this moment, the combustion reaction takes place, resulting in a mix of gases, CO_2, and steam.

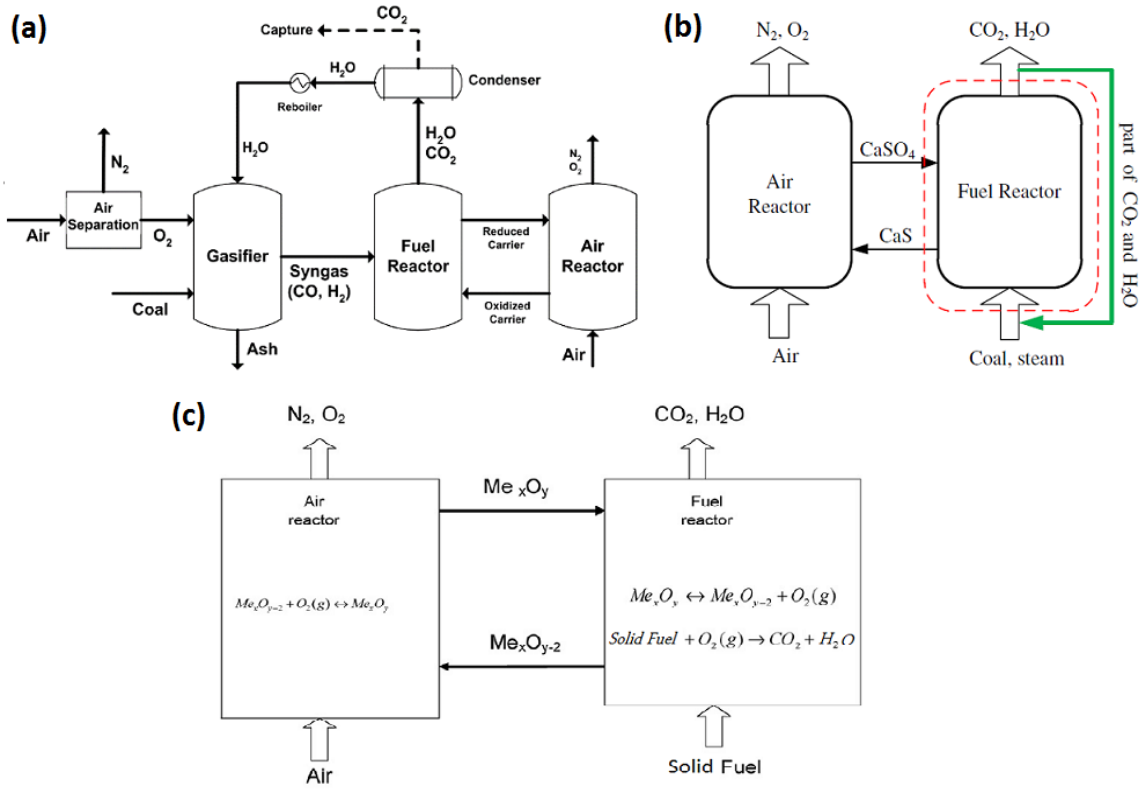

Fig. 1.4. Typical solids fueled chemical looping combustion systems: a) ex-situ gasification CLC [41], b) in-situ gasification CLC [42], c) CLOU.

Chemical Looping with Oxygen Uncoupled (CLOU) (Fig. 1.4c) is similar to gaseous CLC system except that a solid fuel is utilized, which is usually fed into the fuel reactor and allowed to react with the oxygen gas made available from the reduction of the oxygen carriers in the fuel reactor. This process eliminates the use of the gasification unit; however, the reaction mechanisms involved in this process are highly complicated due to the series of complex reactions that occur simultaneously.

Dennis and Scott investigated in-situ gasification/CLC utilizing Cu /Al_2O_3 as an oxygen carrier and Hambach mix (coal/ash) as a fuel in a fluidized-bed reactor [43]. Results showed a fast rate of gasification in which the higher rates occurred at a temperature of 900°C. In addition, at 900°C, O_2 gas was formed (from CuO) and reacted with syngas to produce CO_2 and H_2O. Dennis and Scott reported that although the BET surface area decreased after 20 cycles of oxidation/reduction from 60 m^2/g to nearly 6 m^2/g, the reactivity of the oxygen carrier was not affected. Wang and Zhao studied in-situ gasification CLC using solid plastic wastes to analyze the effect of a CaO-Fe_2O_3/Al_2O_3 oxygen carrier on the conversion of plastic wastes [44]. Results revealed that the optimum conditions to reach a maximum carbon conversion of 98.8% were 900°C, 2.5 supply oxygen ratio and 2:3 steam-to-N_2 fluidizing agent ratio. They also reported that the synthesis of CaO-Fe_2O_3/Al_2O_3 (5-55/40 wt%) oxygen carriers prevented the agglomeration of the active site on the support after 10 oxidation/reduction cycles. Zheng *et al* examined the use of binary $CaSO_4$-Fe_2O_3 carriers for in-situ gasification/CLC of coal [42]. The CO_2 yield increased from 0.65 to 0.85 as the Fe_2O_3 weight fraction increased from 0 to 12%. They reported that this increase was attributed to the reduction of Fe_2O_3 to Fe_3O_4, which was controlled thermodynamically compared to the reduction of Fe_2O_3 to either FeO or Fe. The maximum achievable CO_2 concentration was found to be 95.35% at 900°C.

Jin and Ishida proposed a new type of ex-situ gasification chemical looping combustion of coal [45]. The proposed reactor was a high-pressure fixed-bed reactor packed with a Ni-based oxygen carrier and fed with gasified coal gas. As the temperature increased from 600°C to 700°C, the CO_2 concentration profile increased by only 18%. Additionally, as the temperature and pressure increased to 3 atm. and 1000°C, respectively, the CO_2 concentration profile was remarkably increased by 77.8%. Hamers *et al* simulated a new packed-bed reactor configuration

for the chemical looping combustion of syngas using Ni-, Cu-, Fe- and Mg-based oxygen carriers [46]. The proposed configuration consists of two reactors in series, which utilize two stages of oxidation/reduction reactions. The first oxygen carrier material is used in the first reactor, which operates at lower temperatures (<900°C), followed by the second oxygen carrier material in the second reactor at higher temperatures (>1100°C). The reason behind this configuration is the higher melting point of the second materials when compared to the first. It was found that after the third cycle, steady state operation was achieved with noticeable hot spots in the bed. Hamers *et al* reported that the syngas counter-current feeding technique could be used to reduce energy consumption because heat is recycled back into the reactor instead of being dumped out of the reactor.

Frick *et al* studied mixed metal oxides for their reactivity and fluidization properties when used in CLOU [47]. It was found that the samples' calcination temperature did not show a significant effect on their reactivity. The metal oxides supported by titanium and calcium, however, showed higher methane conversion (99%) at a reaction temperature of 1050°C when compared to the others tested. In addition, titanium- and calcium-supported metals showed lower attrition indexes (weight percentage of fines lost) when evaluated against other samples (<1%). Zhang *et al* proposed a new system for coal pyrolysis coupled with CLOU [48]. Simulated results showed that the proposed system could produce high CO_2 concentration (92.87%) compared to the conventional CLOU system. Moreover, a batch fluidization experiment was conducted to verify this new system where both semi-cokes samples reported CO_2 yield of >99.5% at 850°C and intermediates (i.e. H_2, CO) yields of <1.5% and <0.5% at 850°C, respectively.

1.2.2. Chemical Looping Reforming (CLR)

Chemical looping Reforming is also known as CO_2 capture technology integrated with H_2 production. It is a process that can produce H_2 from carbonaceous fuels without emitting CO_2. The H_2 produced from this process is considered to be a clean alternative fuel. Chemical looping reforming can be divided into steam reforming integrated with chemical looping combustion CLR(s) and auto-thermal chemical looping reforming CLR(a).

1.2.2.1. CLR (s)

Steam reforming integrated with chemical looping combustion technology was first proposed by Ryden and Lyngfelt in 2006 (Fig. 1.5) [49]. The steam reforming reaction takes place inside catalytic reactor tubes that are placed inside the fuel reactor of a CLC system such as the one described earlier (gaseous-fueled CLC process). The combustion reaction that occurs inside the fuel reactor is exothermic while the steam reforming reaction of carbonaceous fuels is endothermic. Thus, the produced heat from the combustion reaction is used to initiate the steam reforming reaction. The overall products from this technology are concentrated and separated streams of CO_2, H_2 and H_2O.

Pans *et al*, attempted to optimize H_2 production in a steam reforming chemical looping combustion process using CH_4 as a fuel and Fe as an oxygen carrier [50]. Results showed that when the reformer tubes were inside the air reactor, a maximum H_2 yield (2.45 mol./CH_4 mol.) was achieved at 880°C. The conversion of CH_4 was 80% in the fuel reactor with 90% efficiency of the pressure swing adsorption unit. Jiang *et al* investigated the use of Ni-based oxygen carrier for H_2 production in the steam reforming of glycerol chemical looping combustion system [51]. An H_2 concentration of 90% was achieved at 600°C; however, the glycerol conversion decreased (~34%) in addition to a drop in the conversion of NiO to Ni (~17%) after five oxidation/reduction

cycles at 550°C. Ortiz *et al* studied the use of iron waste products as an oxygen carrier in steam reforming CH_4-fueled chemical looping combustion [52]. The highest oxygen capacity was found to be 2.4%; however, the methane combustion efficiency was determined to be 90% when a solid inventory of 800 kg/MW was used. They reported that the optimal oxygen carrier-to-fuel ratio was found to be 1.5.

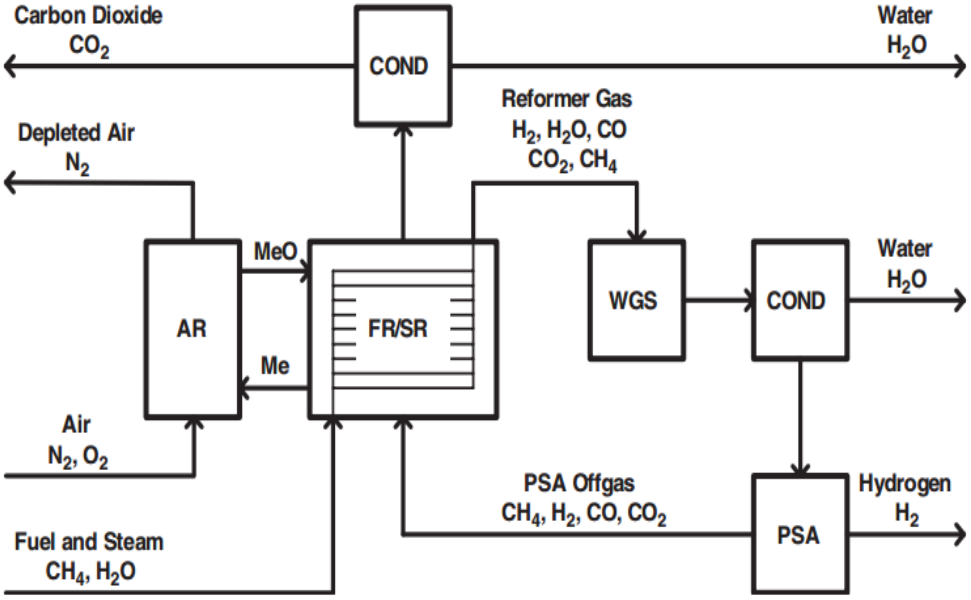

Fig. 1.5. Schematic diagram of steam reforming chemical looping combustion (CLR(s)) process. (AR) air reactor, (FR/SR) fuel reactor and steam reforming units, (COND) condenser, (WGS) water-gas shift reaction unit, (PSA) pressure swing adsorption unit [49].

1.2.2.2. CLR (a)

The auto-thermal chemical looping reforming CLR(a) process was first proposed by Mattisson and Lyngfelt in 2001 (Fig. 1.6) [53]. It utilizes the same reactor configuration as the previously described CLC process (Fig. 2.1b) except that the available oxygen from the oxidized oxygen carriers is limited by lowering the air/fuel ratio in order to achieve partial oxidation status. Thus, the gas products mainly consist of CO_2, H_2O, H_2 and CO. A shift reactor

$(CO + H_2O \rightarrow CO_2 + H_2)$ is then used to produce a stream containing high concentrations of H_2 and CO_2.

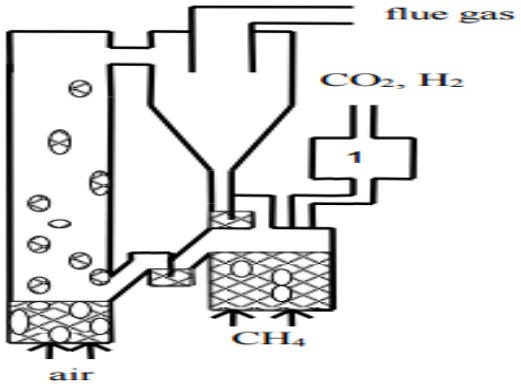

Fig. 1.6. Methane gas auto-thermal chemical looping reforming technology; (1) shift reactor [53].

Garcia-Diez *et al* studied the optimization of an auto-thermal bioethanol chemical looping reforming process using a Ni-based oxygen carrier [54]. It was reported that carbon deposition could be prevented if an H_2O/fuel ratio of 3 was used. Moreover, high H_2 production (4.62 H_2 mol./bioethanol mol.) could be obtained at 715°C in the fuel reactor. Zhao *et al* investigated the auto-thermal chemical looping reforming of biomass using a Cu-based oxygen carrier [55]. The aim of their study was to produce syngas from biomass. At 800°C, the tar content decreased by up to 54% when using a Cu ore material as an oxygen carrier. As the temperature increased from 600 to 850 °C, the gas yield and carbon conversion efficiency increased to 72% and 65%, respectively. Ortiz *et al* studied H_2 production using a Ni-based oxygen carrier in the auto-thermal chemical looping reforming process [56]. It was observed that decreasing the O_2/CH_4 molar ratio could enhance H_2 production. They reported that the maximum H_2/CH_4 yield ratio was determined to be 2.75. Additionally, an increase in the temperature difference between the air and fuel reactors could result in the reduction of H_2 production and increase the needed O_2/CH_4 molar ratio.

1.2.3. Chemical Looping Air Separation

Chemical looping air separation technology is used to produce a highly concentrated stream of O_2. It was first proposed by Moghtaderi in 2010 (Fig. 1.7) [57]. This process is similar to the gaseous-fueled chemical looping combustion process, but steam is used instead of gaseous fuels. Hence, the product from the fuel reactor is a mixture of steam and oxygen, which is then separated using condensation in order to obtain a stream of high pure oxygen. The oxygen produced from this technology can then be used to feed other processes such as oxy-fuel combustion engine and Integrated Gasification Combined Cycle (IGCC) technology.

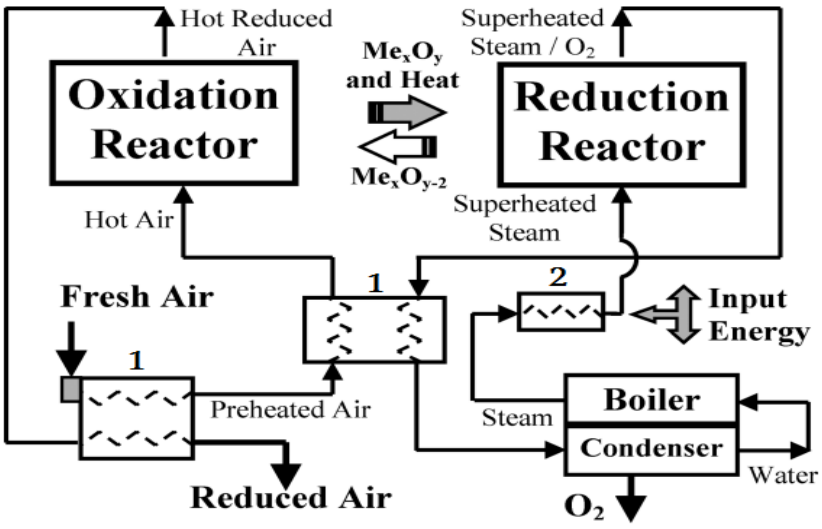

Fig. 1.7 Process diagram of chemical looping air separation technology; (1) heat exchanger, (2) heater [57].

Wang *et al* prepared and examined Cu/Mg-Al_2O_4 as an oxygen carrier for chemical looping air separation in a TGA and fixed-bed reactor [58]. It was observed that even at high temperatures the active site and support did not interact with each other. The effect of particle size on the oxygen transport was also found to be negligible. Additionally, Cu/$MgAl_2O_4$ began releasing the absorbed

O_2 at 400°C; however, the highest O_2 desorption temperature was found to be 1010°C, and the highest obtained oxygen concentration (20%) was reported at 950°C. Wang *et al* studied Co/ZrO_2 for its potential use in chemical looping air separation systems [59]. The optimum oxidation temperature was found to be 800°C whereas the reduction temperature was between 800 and 1000 °C. Changes in the reactivity, agglomeration and deterioration of pores were not observed even after 23 cycles of oxidation/reduction reactions. Zhou *et al* assessed the techno-economic of a 500 MW chemical looping air separation coal-fired plant [60]. It was suggested that the air reactor could be operated at lower temperatures than the fuel reactor, while the transfer of heat from the air reactor to fuel reactor could be achieved using an additional heat source such as a solar system or CH_4 firing unit. This, in turn, would reduce the overall energy requirement for O_2 production. Zhou *et al* reported that the new proposed process could be made economically feasible, especially with lower natural gas prices.

1.2.4. Role of Oxygen Carriers in the Technology of Chemical Looping Combustion

Oxygen carriers in chemical looping combustion technologies are considered catalysts, as they can neither be consumed nor produced during the oxidation and reduction reactions. They are, however, the most important elements in chemical looping combustion processes because they circulate the needed oxygen from the air reactor to the fuel reactor. As a result, there are some restrictions when it comes to choosing the suitable oxygen carriers for the previously explained technologies. One of these restrictions is the physical state of the oxygen carriers. They cannot be liquid or gas as the vast majority of the chemical looping combustion processes are operated at high temperature (>600°C), which makes the use of liquids and gases impractical due to the phase changes and the additional gas separation units that would be required. Therefore, solid oxygen carriers are most likely to be used. Another restriction is that these solids should resist high

temperatures, pressures, and others materials/fluidization properties (in the case of fluidized-bed reactors) so as to obtain high yields of the desired products (i.e. CO_2, H_2, O_2). Thus, the scope of most studies has been toward metal-based oxygen carriers due to their potential to meet all of the above-mentioned restrictions.

Solid metal-based oxygen carriers can be synthesized using numerous different combinations of metal elements. Although most of the chemical looping combustion studies focus on the use of metal-based oxygen carriers, there is still room to develop the best and most novel combinations of these metals [23], [26]. The factors that are usually used to assess these metal-based oxygen carriers are surface area, resistance to agglomeration and attrition, tolerance of high temperature and sulfur, and oxygen capacity.

Surface area is defined as the available areas on the surface of the solid particles. The supports have a higher surface area when compared to the active site. This allows a uniform dispersion of the active sites on the support, which can increase the reactivity and stability of these solid oxygen carriers as a whole. Therefore, in theory, the higher the surface area and the even dispersion of the active site, the higher the catalytic reactivity.

Agglomeration of oxygen carriers means that the active site on the inert support tends to reallocate itself and center on one spot, while attrition means that the solid oxygen carriers lose their strength and break down into small pieces. Both agglomeration and attrition are signs of catalyst decay. They usually result in a decrease in the catalytic reactivity of oxygen carriers. Agglomeration is most likely to occur when the oxygen carriers are exposed to high temperatures [61]. The most feasible reason for this phenomenon is that the bonds energy between the active site and support becomes weaker than those bonds energy between the active site and the particles.

The reallocation and centering of the active site on the support could possibly be attributed as a means to balance these bonds energies.

Attrition, on the other hand, usually occurs when the oxygen carrier is in continuous movement during the course of reactions (oxidation/reduction) such as the conditions found in a fluidized-bed reactor. The movement of the particles breaks down the weaker particles into smaller pieces, which changes the uniformity of the active site on the inert support/s. Attrition can be measured using a variety of different techniques to estimate the particles' resistance to breakage [62], [63].

Temperature and sulfur tolerance must also be considered during the oxygen carrier screening process. Since most of the industrial chemical looping combustion processes take place at high oxidation and reduction temperature (>600°C), the presence of small contaminations (i.e. sulfur compounds) in either solid of gaseous fuels can poison (stop the reactivity) the oxygen carriers. Thus, both the melting points and sulfur resistance of oxygen carriers must be considered. Usually solid metals with lower melting temperatures are excluded due to these criteria, for example lead (m.p. ~328°C). The reason is that at higher temperature, these metals start melting, which can result in changes to structure, porosity and kinetics, meaning that incorrect behaviours are measured. Sulfur poisoning is the reaction that occurs between the active sites and sulfur, resulting in the deposition of sulfur particles on the active sites and in turn blocking or lowering their catalytic activity. An example of oxygen carriers sulfur poisoning is the nickel-based catalyst ($Ni_{14\%}/Al_2O_3$) that was poisoned by sulfur and its reactivity decreased up to 45% within 15 hrs. of methanation reaction [64].

Oxygen capacity can be defined as the ratio of gained oxygen weight to the weight of the oxygen carrier. It can be measured using different techniques, including use of a

Thermogravimetric Analyzer (TGA), in which weight changes are recorded as a function of temperature with different reacting gases. Theoretical oxygen capacity can be calculated by dividing the weight of reduced oxygen molecules by the weight of the oxidized oxygen carrier. For example, if the oxidized copper (2CuO) gives oxygen (O_2), its oxygen capacity is 0.2011 or 20.11%. Oxygen capacity plays an important role in the screening process of oxygen carriers, as higher oxygen capacity allows for a decrease in the solid recirculation rate, as well as reduced inventories. In this way, higher fuel conversion rates can be obtained, increasing the overall efficiency of the CLC process and, in turn, lowering its capital cost.

Numerous variants of metal-based oxygen carriers have been mentioned in the literature, such as Fe, Cu, Co, and Ni; however, very modest modifications have been carried out so far to maximize the fuel conversion rate to CO_2 and H_2O. Iron is the most abundant metal when compared to Cu, Co, and Ni and its oxygen capacity is the lowest (~3%). Although Cu, Co and Ni may have some economic and environmental concerns, their oxygen capacities are considered to be the highest among their counterparts. Therefore, combinations of Fe, Cu, Co, and Ni oxygen carriers provide promising developmental outlooks due to their high oxygen capacity, cost-effectiveness, and the overall environmental sustainability of chemical looping combustion technology.

Frick *et al* investigated the use of mixed metal-based oxygen carriers (Fe-Cu and Mn-Ni) in a chemical looping combustion process using CO, H_2 and CH_4 as fuels [65]. The samples were prepared by the spray-drying method. The mixed metals oxygen carrier (Fe-Cu) showed higher fuel conversion with average CO_2 yields >90% at 1050°C, while the CO_2 yield of the mixed metals oxygen carrier (Mn-Ni) was >85% at 1050°C. Frick *et al* reported that as the calcination temperature increased, the crushing strength for most mixed metal samples increased; however,

calcination temperature did not show a significant effect on the attrition index. Guo *et al* tested Fe-based oxygen carriers for in-situ gasification chemical looping combustion using coal as solid fuel in a batch fluidized-bed reactor [66]. The oxygen carriers were prepared using the sol-gel method. Results revealed that a surface area of 4.92 m^2/g was observed when the sol-gel preparation method was used. The surface area was then attributed to the high CO_2 selectivity (>95%). Mohamed *et al* synthesized and evaluated NiO/Ce-Al_2O_3 for its oxygen capacity in a CH_4-fueled CLC system [67]. They reported that the contact time of 60 seconds at 650°C resulted in more than 80% conversion of NiO. Abad *et al* derived a model that evaluated different operating parameters in a bubbling fluidized-bed reactor (fuel reactor) of a CLC system using CH_4 as fuel [68]. With only 14 wt% of active site on the CuO grain, the optimum ratio of oxygen carrier to fuel was found to be between 1.7-4, with a combustion efficiency of 99.9% at 700°C. Bakare *et al* studied the kinetics of VOx-MoOx/Al_2O_3 as an oxygen carrier in a C_2H_6-fueled fluidized-bed reactor to investigate the effect of temperature and residence time [69] and found that a temperature of 650°C and residence time of 30s favoured COx among other gases. Hossain and Lasa investigated the kinetics of the bimetallic Co-Ni/Al_2O_3 oxygen carrier using O_2-TPO and H_2-TPR (Temperature Programmed Oxidation/Reduction) [70]. The oxidation and reduction kinetics followed the nucleation and nuclei growth model. The reaction order was assumed to be 1, where the activation energies for oxidation and reduction reactions were found to be 44 and 45 kJ/mol., respectively, at temperatures that ranged from 550 to 650 °C. They reported that the addition of promoter (Co) lowers the activation energy by up to 45 kJ/mol. compared to the unprompted sample (i.e. Ni/Al_2O_3). Xu *et al* synthesized copper-based mixed metal oxides (Cu/Al_2O_3-TiO_2) oxygen carriers and tested them for the CH_4-fueled chemical looping combustion process [71]. The samples were prepared using the core-shell method and examined on both a TGA and fluidized-bed reactor. Results revealed

that the highest oxygen capacity (~7.8%) was observed with a $CuO_{77.5\%}/TiO_{2\,5\%}Al_2O_{3\,17.5\%}$ sample. Xu *et al* reported that the addition of TiO_2 prevented the interaction between CuO and Al_2O_3 as well as CuO grains agglomeration on the mixed support oxides.

1.3. Objectives

The main concern in ensuring the commercialization success of the CLC process is to determine novel oxygen carriers that are chemically and thermally stable for multi-cyclic redox reactions. Various attempts to do this have been made in literature, yet several challenges have not been resolved: specifically, the kinetics of restructuring the active sites on different supports, the effect of oxygen carriers' structure on the reaction rate, the effect of attraction energy between precursors and supports on the oxidation/reduction reactions, the effect of phase changes of metal on the reactivity and reaction kinetics, and determination of governing pathways of oxidation/reduction reactions for mixed metals oxygen carriers. Therefore, the main objective of this thesis is to address all the above-mentioned challenges from lab synthesis of oxygen carriers to pilot-scale testing.

The following are the specific objectives of this thesis:

1. To synthesize and study the kinetics of oxidation and reduction reactions for transition metals (Cu, Fe, Ni, Co) deposited on supports (Al_2O_3, CeO_2, TiO_2, ZrO_2) under different parameters such as temperature, initial sample weight, methane concentration, metal transition phases, and metal loading percent (Chapter 3).
2. To synthesize and investigate the effect of bimetallic precursors (Ni-Co, Ni-Cu, Ni-Fe) on supports (Al_2O_3, CeO_2, TiO_2, ZrO_2) and the kinetics (intrinsic and global) of redox reaction to determine the redox pathways (Chapter 4).

3. To evaluate and simulate the kinetics and thermodynamics of the CLC process when nickel oxide supported by alumina is used in Aspen Plus software to mitigate potential problems associated with the use of NiO/Al_2O_3 carrier (Chapter 5).
4. To study and simulate the CLC process scale-up in Aspen Plus software for the techno-economic and reactivity assessments of bimetallic carrier ($Ni\text{-}Cu/ZrO_2$) to produce 50 MW of power (Chapter 6).

1.4. Layout of the thesis

This thesis consists of six chapters, organized and consecutively formatted in a paper-based thesis. Chapters 2 to 5 are presented in a paper-based format. Chapters 2 and 3 are already published peer-reviewed papers, while chapter 4 has already been submitted to a peer-reviewed journal. Chapter 5 will be submitted to a peer-reviewed journal soon. A brief descriptive summary of chapters 1 to 6 is as follows:

- Chapter 1 introduces the thesis by providing overall background to date about the research and an overview of the selected research topic. A literature review about the research is offered to summarize recent findings, challenges found to date, and progress with the chemical looping combustion process in the last 15 years. By the end of chapter, the overall and specific objectives of the thesis, and outcomes in term of published papers are presented.
- Chapter 2 presents the synthesizing method used to prepare the supported monometallic oxygen carriers for the CLC process. It is the first experimental chapter of this thesis, intended to screen potential oxygen carriers for further development and stability testing. It shows and explains the effect of different operating conditions such as temperature,

methane concentration, and sample initial weight on the reactivity of the synthesized carriers. The methodology to obtain the kinetics parameters is discussed and explained.

- There has been reported work in the literature on the use of bimetallic oxygen carriers for the methane CLC process, but little work explaining the reaction pathways of these carriers. Hence, Chapter 3 investigates and comprehensively evaluates the use of bimetallic precursors (Ni-Co, Ni-Cu, Ni-Fe) supported by (Al_2O_3, CeO_2, TiO_2, ZrO_2) in the methane CLC process. Breakthrough findings about mass transfer limitations, interaction between precursors and supports, and reduction reaction pathways of supported bimetallic carriers are found and presented.
- The use of nickel oxide support by alumina is considered an economic option for the methane CLC process because alumina is the cheapest option compared to the others available (ceria, titania, zirconia). However, there are challenges associated with the use of nickel oxide support by alumina such as carbon deposition, formation of intermediate phase ($NiAl_2O_4$), and mass transfer effects on kinetics. Hence, Chapter 4 investigates the kinetics and thermodynamics of the methane CLC process to overcome potential problems found in nickel oxide support by alumina carrier. It introduces the CLC reactor system (air and fuel reactors) where the kinetics, thermodynamics, and sensitivity analysis assessments are conducted. Optimum operating conditions such as temperature, pressure and flowrates are obtained and explained.
- Chapter 5 presents the scale-up CLC process where a supported bimetallic carrier (Ni-Cu/ZrO_2) is used to simulate the entire CLC process for the purpose of producing 50 MW of power. The air reactor is considered to be a circulating fluidized-bed reactor, and the fuel reactor is considered to be a bubbling fluidized-bed reactor. Intensive calculations for

the reactor design, hydrodynamics, and kinetics are performed on both reactors, then the process flowsheet in Aspen Plus is constructed and the process is tested. The advantages found with this process are the production of a pure CO_2 stream, and a considerably higher efficiency than the Combined Cycle Power Plant (CCPP) and Pulverized Coal (PC) power plant processes; however, considerable challenges remain to be investigated, such as the regeneration of decaying carriers, economic feasibility, and the attrition index of carriers.

- In Chapter 6, the main conclusions that can be drawn from the thesis are summarized, and the relation between chapters is explained. The recommendations and suggestions for future work within the field of methane CLC processes are discussed and presented.

1.5. Relation between chapters and overall achievement

In this work, three topics were researched related to the study of the methane CLC process. The first topic is the synthesis of supported monometallic oxygen carriers as a baseline to study the effect of different operating parameters such as temperature, concentration, and initial sample weight (Chapter 2). Chemical looping combustion was conducted in the thermogravimetric analyzer (TGA), and it was found that different phases during the experiment, as well as the variation of temperature, affected the oxygen capacity of all samples. Some intermediates formed, with some being reducible within our experiment condition while others did not reduce. Kinetic parameters such as activation energy, pre-exponential factor and reaction order were estimated, which are essential for the next stage of the research.

The second topic covers the synthesis and reactivity evaluation of bimetallic oxygen carriers for the methane CLC process (Chapter 3). The bimetallic samples were synthesized using the incipient wetness impregnation method and tested for their reactivity in the thermogravimetric

analyzer (TGA). The optimum operating conditions found previously applied, with breakthrough results in the redox reaction pathways obtained and explained in detail. The most stable and promising oxygen carriers were then selected to be tested in the third topic.

In the third topic, Aspen Plus computer software is used to assess the reactivity and process feasibility. Two case studies were outlined, with the first being a micro-reactor system (Chapter 4) to assess the thermodynamics and kinetics of supported nickel oxide carriers to overcome potential problems such as formation of carbon and mass transfer limitations. The second case study was a pilot plant of the best-found supported bimetallic carrier (Ni-Cu/ZrO_2) to produce 50 MW of power (Chapter 5). The complete process flowsheet was constructed in Aspen Plus and the effect of various parameters on the conversion in the air and fuel reactors units was assessed. At the optimum operating conditions, the overall process efficiency was estimated and compared to other competing processes, with our case study showing the best efficiency compared to the others.

Below is a schematic showing relation between chapters presented in this work:

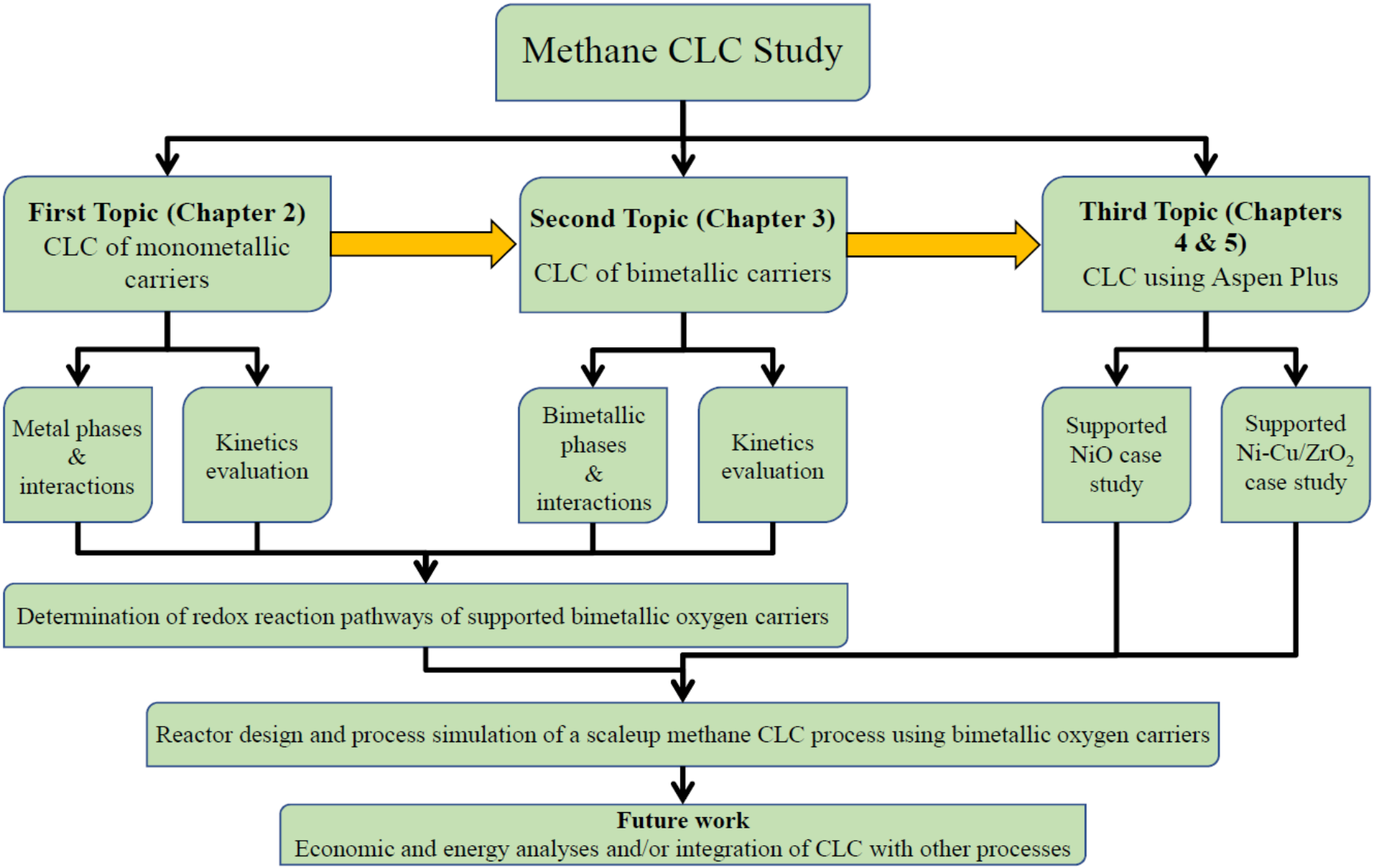

Fig. 1.8. Relation between chapters.

1.6. Outcome of the thesis

The candidate has published three peer-reviewed journal papers (Chapters 2 and 3) as first author and three peer-reviewed national/international conference proceedings as first author, submitted a manuscript as first author to a peer-reviewed journal (Chapter 4), and will submit a manuscript as first author to a peer-reviewed journal (Chapter 5). In addition, the candidate has published two peer-reviewed papers as second author.

Published peer-reviewed journal papers (First author):

1) **Tijani, M. M.,** Siegler, H., and Mahinpey, N., Reactivity and economic assessments of a 50 MW methane fuelled chemical looping combustion process using supported bimetallic (Ni-Cu/Al_2O_3) oxygen carrier. To be submitted.
2) **Tijani, M. M.,** Mostafavi, E., and Mahinpey, N., Process simulation and thermodynamic analysis of a chemical looping combustion system using methane as fuel and NiO as oxygen carrier in a moving bed reactor. Chemical Engineering and Processing - Process Intensification. Submitted (2018).
3) **Tijani, M. M.,** Aqsha, A., and Mahinpey, N., Synthesis and study of metal-based oxygen carriers (Cu, Co, Fe, Ni) and their interaction with supported metal oxides (Al_2O_3, CeO_2, TiO_2, ZrO_2) in a chemical looping combustion system. Energy. 138 (2017) 873-882.
4) **Tijani, M. M.,** Aqsha A., and Mahinpey, N., X-ray Diffraction and TGA kinetic analyses for Chemical Looping Combustion Applications. Data in Brief. 17 (2017) 200-209.
5) **Tijani, M. M.,** Aqsha, A., Yu, N., and Mahinpey, N., Determination of redox pathways of supported bimetallic oxygen carriers in a methane fuelled chemical looping combustion system. Fuel. 233 (2018) 133-145.

Published peer-reviewed conference proceedings (First author):

1) **Tijani, M. M.,** and Mahinpey, N., Techno-economic and reactivity assessments of a methane-fuelled chemical looping combustion process using supported bimetallic oxygen carrier (Cu-Ni/Al_2O_3): A case study to produce 50 MW power. The International Conference on Negative CO_2 Emissions. Chalmers University of Technology, Gothenburg, Sweden. Conference Proceeding. (2018).
2) **Tijani, M. M.,** and Mahinpey, N., Investigation of metals/mixed metals (Ni, Co, Cu, Fe) and Al_2O_3, CeO_2, TiO_2, ZrO_2 supports as oxygen carriers for the methane chemical looping combustion process. Impacts of Fuel Quality on Power Production and the Environment. Lake Louise, AB, Canada. Conference Proceeding. (2018).
3) **Tijani, M. M.,** Aqsha, A., and Mahinpey, N., Reactivity assessment and kinetic measurements of methane-fueled chemical looping combustion using supported mixed metals (Ni-Co, Ni-Cu, Ni-Fe) and Al_2O_3, CeO_2, TiO_2, and ZrO_2 supports as oxygen carriers. Greenhouse Gas Control Technologies (GHGT) conference. Melbourne, Australia. Conference Proceeding. (2018).

Published peer-reviewed journal papers (Second author):

1) Aqsha A., **Tijani, M. M.,** Moghtaderi, B., and Mahinpey, N., Catalytic pyrolysis of straw biomasses (wheat, flax, oat and barley) and the comparison of their product yields. Journal of Analytical and Applied Pyrolysis. 125 (2017) 201-208.
2) Aqsha A., **Tijani, M. M.,** and Mahinpey, N., Catalytic pyrolysis of straw biomasses (wheat, flax, oat and barley straw) and the comparison of their products yield. Energy Production and Management in the 21st Century, WIT Press. 2 (2014) 1007-1016.

1.7. References

[1] Jancovici, J-M., Manicore. What are the greenhouse gases? Available at https://www.manicore.com/anglais/documentation_a/greenhouse/greenhouse_gas.html Date accessed: [09-19-2016].

[2] Watson, R.T., Rodhe, H., Oeschger, H., and U. Siegenthaler. "GREENHOUSE GASES AND AEROSOLS." *Scientific Assessment of Climate Change: Report* (1990): 1.

[3] U.S. Environmental Protection Agency. Greenhouse Gases. A student guide to global climate change. Available at https://www3.epa.gov/climatechange/kids/basics/today/greenhouse-gases.html Date accessed: [09-19-2016].

[4] Le Treut, H., 2007. Historical overview of climate change. Climate Change 2007: The Physical Science Basis. Contribution of Working Group I to the Fourth Assessment Report of the Intergovernmental Panel on Climate Change.

[5] Prentice, I.C., Farquhar, G.D., Fasham, M.J.R., Goulden, M.L., Heimann, M., Jaramillo, V.J., Kheshgi, H.S., LeQuéré, C., Scholes, R.J. and Wallace, D.W., 2001. The carbon cycle and atmospheric carbon dioxide. Cambridge University Press.

[6] Johnston, W. R., 2013. Historical data relating to global climate change. (2016, July 21). Retrieved from http://www.johnstonsarchive.net/environment/co2table.html

[7] US Department of Commerce, National Oceanic and Atmospheric Administration / NOAA Research. (2018, August 15). Retrieved from http://www.esrl.noaa.gov/gmd/ccgg/trends/

[8] Leggett, J., Pepper, W., Swart, R.J., 1992. Emissions Scenarios for the IPCC: An Update. Contributors: Edmonds, J. A., Meira Filho, L.G., Mintzer, I., Wang, M. –X., Wasson, J.

Climate Change 1992: The Supplementary Report to the IPCC Scientific Assessment. Cambridge, United Kingdom.

[9] Farquhar, G. D., Fasham, M.J.R., Goulden, M.L., Heimann, M., Jaramillo, V.J., Kheshgi, H.S., Le Quéré, C., Scholes, R.J., Wallace, D.W.R., 2001. Climate Change 2001: The Scientific Basis. Chapter 3: The Carbon Cycle and Atmospheric Carbon Dioxide Content. Cambridge, United Kingdom.

[10] Leung, D. Y. C., Caramanna, G., Maroto-Valer, M. M., 2014. An overview of current status of carbon dioxide capture and storage technologies. Renewable and Sustainable Energy Reviews. 426-443.

[11] Kumar G. S., Viswandham M., Gupta. A.V.S.S.K.S., Kumar, G.S., 2013. A review of pre-combustion CO_2 capture in IGCC. International Journal of Research in Engineering and Technology. (2) 847-853.

[12] Huang, L., Wang, J., Gao, Y., Qiao, Y., Zheng, Q., Guo, Z., Zhao, Z., O'Hared, D., Wang, Q., 2014. Synthesis of LiAl2-layered double hydroxides for CO2 capture over a wide temperature range. Journal of Materials Chemistry A. (2) 18454-18462.

[13] Zarogiannis, T., Papadopoulos, A. I., Seferlis, P., 2016. Systematic selection of amine mixtures as post-combustion CO2 capture solvent candidates. Journal of Cleaner Production.159-175.

[14] Maurstad, O., 2005. An Overview of Coal based Integrated Gasification Combined Cycle (IGCC) Technology (MIT LFEE 2005-002 WP). Laboratory for energy and the environment. MIT. MA. USA.

[15] Global Carbon Capture and Storage Institute. 2011. CO_2 Capture Technologies: pre-combustion capture. Canberra, Australia. Retrieved from:

http://www.globalccsinstitute.com/publications/co2-capture-technologies-pre-combustion-capture

[16] Hedin, N., Andersson, A., Bergström, L., Yan, J., 2013. Adsorbents for the post-combustion capture of CO_2 using rapid temperature swing or vacuum swing adsorption. Applied Energy. (104) 418-433.

[17] International Union of Pure and Applied Chemistry (IUPAC). 2001. Chemisorption and physisorption. Adsorption and spread monolayers. Retrieved from: http://old.iupac.org/reports/2001/colloid_2001/manual_of_s_and_t/node16.html

[18] Xu, C., Hedin, N., 2014. Microporous adsorbents for CO_2 capture – a case for microporous polymers. Materials Today. (17) 397-403.

[19] Kumar, A., Madden, D.G., Lusi, M., Chen, K., Daniels, E.A., Curtin, T., Perry, J.J., Zaworotko, M. J., 2015. Direct Air Capture of CO2 by Physisorbent Materials. Angewandte Chemie International Edition. (54) 14372-14377.

[20] Lee, S. Y., Park, S. J. A review on solid adsorbents for carbon dioxide capture, Journal of Industrial and Engineering Chemistry, 2014.

[21] IEA Energy Technology Essentials. 2006. CO2 Capture and Storage. (2016, July 20). Retrieved from https://www.iea.org/publications/freepublications/publication/essentials1.pdf

[22] Luis, P., 2016. Use of monoethanolamine (MEA) for CO_2 capture in a global scenario: Consequences and alternatives. Desalination. (380) 93-99.

[23] Hossain, M. M., de Lasa H. I., 2008. Chemical-looping combustion (CLC) for inherent CO_2 separations—a review. Chemical Engineering Science. (63) 4433-4451.

[24] Lyngfelt, A., Leckner, B., Mattisson, T., 2001. A fluidized-bed combustion process with inherent CO_2 separation; application of chemical-looping combustion. Chemical Engineering Science 3101–3113.

[25] Johansson, M., Mattisson, T., Rydén, M., Lyngfelt, A., 2006. Carbon capture via chemical looping combustion and reforming. International seminar on carbon sequestion and climate change. Rio de Janeiro, Brazil: PUC Rio.

[26] Adánez, J., Abad, A., García-Labiano, F., de Diego, L, F., Gayán, P., 2012. Progress in Chemical-Looping Combustion and Reforming Technologies. A review. Progress in Energy and Combustion Science 215-282.

[27] Kerr HR. Capture and separation technology gaps and priority research needs. In: Thomas DC, Benson SM, editors. Carbon dioxide capture for storage in deep geologic formations results from the CO_2 capture project, vol. 1. Oxford, UK: Elsevier; 2005 [chapter 38].

[28] Ishida, M., Zheng, D., Akehata, T., 1987. Evaluation of a chemical-looping-combustion power-generation system by graphic exergy analysis. Energy. 147-154.

[29] Dahl, I. M., Bakken, E., Larring, Y., Spjelkavik, A. I., Håkonsen, S. F., Blom, R., 2009. On the development of novel reactor concepts for chemical looping combustion. Energy Procedia. 1513-1519.

[30] Han, L., Bollas, G. M., 2016. Chemical-looping combustion in a reverse-flow fixed bed reactor. Energy. 663-681.

[31] Donat, F., Hu, W., Scott, S. A., Dennis, J. S., 2015. Characteristics of Copper-based Oxygen Carriers Supported on Calcium Aluminates for Chemical-Looping Combustion with Oxygen Uncoupling (CLOU). Industrial & Engineering Chemistry Research 6713−6723.

[32] Ksepko, E., 2015. "Examining $SrCuO_2$ as an oxygen carrier for chemical looping combustion." J. Therm Anal Calorim 621–633.

[33] Wang, X., Liu, H., Jin, B., Zhao, J. Sun, C., Snape, C. E., 2015. Experimental Evaluation of a Chinese Sulfur-Containing Lean Iron Ore as the Oxygen Carrier for Chemical-Looping Combustion. Industrial & Engineering Chemistry Research. 428-435.

[34] Monazam, E. R., Breault, R. W., Tian, H., 2Siriwardane, R., 2015. Reaction Kinetics of Mixed $CuO{-}Fe_2O_3$ with Methane as Oxygen Carriers for Chemical Looping Combustion. Industrial & Engineering Chemistry Research.11966-11974.

[35] Mei, D. Mendiara, T., Abad, A., de Diego, L. F., García-Labiano, F., Gayań, P., Adańez, J., Zhao, H., 2015. Evaluation of Manganese Minerals for Chemical Looping Combustion. Energy and Fuels. 6605-6615.

[36] Zheng, X., Su, Q., Mi, W., 2015. "Study of a Cu-Based Oxygen Carrier Based on a Chemical Looping Combustion Process." Energy & Fuels 3933−3943.

[37] Harper, R. N., Boyce, C. M., Scott, S. A., 2013. "Oxygen carrier dispersion in inert packed beds to improve performance in chemical looping combustion." Chemical Engineering Journal 464–474.

[38] Zhu, J., Wang, W., Hua, X. N., Wang, F., Xia, Z., Deng, Z., 2015. "Phase distribution and stepwise kinetics of iron oxides reduction during chemical looping hydrogen generation in a packed bed reactor." International Journal of Hydrogen Energy 12097-12107.

[39] Hamers, H. P., Gallucci, F., Williams, G., Annaland, M. VS., 2015. "Experimental demonstration of CLC and the pressure effect in packed bed reactors using $NiO/CaAl_2O_4$ as oxygen carrier." Fuel 828–836.

[40] Song, Q., Xiao, R., Deng, Z., Zhang, H., Shen, L., Xiao, J., Zhang, M., 2008. "Chemical-looping combustion of methane with CaSO4 oxygen carrier in a fixed bed reactor." Energy Conversion and Management journal homepage: 3178–3187.

[41] Wang, P., Means, N., Shekhawat, D., Berry, D., Massoud, M., 2015. Chemical-Looping Combustion and Gasification of Coals and Oxygen Carrier Development: A Brief Review. Energies. 10605-10635.

[42] Zheng, M., Shen, L., Feng, X., 2014. In situ gasification chemical looping combustion of a coal using the binary oxygen carrier natural anhydrite ore and natural iron ore. Energy Conversion Management. 270-283.

[43] Dennis, J. S., Scott, S. A., 2010. In situ gasification of a lignite coal and CO_2 separation using chemical looping with a Cu-based oxygen carrier. Fuel. 1623-1640.

[44] Wang, J., Zhao, H., 2016. Evaluation of CaO-decorated Fe_2O_3/Al_2O_3 as an oxygen carrier for in-situ gasification chemical looping combustion of plastic wastes. Fuel. 235-243.

[45] Jin, H., Ishida, M., 2004. A new type of coal gas fueled chemical-looping combustion. Fuel. 2411-2417.

[46] Hamers, H. P., Gallucci, F., Cobden, P. D., Kimball, E., van Sint Annaland, M., 2013. A novel reactor configuration for packed bed chemical-looping combustion of syngas. International Journal of Greenhouse Gas Control. 1-12.

[47] Frick, V., Ryden, M., Leion, H., Mattisson, T., Lyngfelt, A., 2015. Screening of supported and unsupported Mn-Si oxygen carriers for CLOU (chemical-looping with oxygen uncoupling). Energy. 544.554.

[48] Zhang, Y., Jin, B., Zou, X., Zhao, H., 2016. A clean coal utilization technology based on coal pyrolysis and chemical looping with oxygen uncoupling: Principle and experimental

validation. 181-189.

[49] Rydén, M., Lyngfelt, A., 2006. Using steam reforming to produce hydrogen with carbon dioxide capture by chemical-looping combustion. International Journal of Hydrogen Energy. 1271-1283.

[50] Pans, M. A., Abad, A., de Diego, L. F., Garcia-Labiano, F., Gayan, P., Adanez, J., 2013. Optimization of H_2 production with CO_2 capture by steam reforming of methane integrated with a chemical-looping combustion system. International Journal of Hydrogen Energy. 11878-11892.

[51] Jiang, B., Dou, B., Song, Y., Zhang, C., Du, B., Chen, H., Wang, C., Xu, Y., 2015. Hydrogen production from chemical looping steam reforming of glycerol by Ni-based oxygen carrier in a fixed-bed reactor. Chemical Engineering Journal. 459-467.

[52] Ortiz, M., Gayán, P., de Diego, L. F., García-Labiano, F., Abad, A., Pans, M. A., Adánez, J., 2011. Hydrogen production with CO_2 capture by coupling steam reforming of methane and chemical-looping combustion: Use of an iron-based waste product as oxygen carrier burning a PSA tail gas. Journal of Power Sources. 4370-4381.

[53] Mattisson, T., Lyngfelt, A., 2001. Applications of chemical-looping combustion with capture of CO_2. Second Nordic Minisymposium on Carbon Dioxide Capture and Storage, Göteborg, October 26, 2001.

[54] García-Díez, E., García-Labiano, F., de Diego, L.F., Abad, A., Gayán, P., Adánez, J., Ruíz, J. A. C., 2016. Optimization of hydrogen production with CO_2 capture by autothermal chemical-looping reforming using different bioethanol purities. Applied Energy. 491-498.

[55] Zhao, H., Guo, L., Zou, X., 2015. Chemical-looping auto-thermal reforming of biomass using Cu-based oxygen carrier. Applied Energy. 408-415.

[56] Ortiz, M., Abad, A., de Diego, L.F., Garcia-Labiano, F., Gayan, P., Adanez, J., 2011. Optimization of hydrogen production by Chemical-Looping auto-thermal Reforming working with Ni-based oxygen-carriers. International Journal of Hydrogen Energy. 9663-9672.

[57] Moghtaderi, B., 2010. Application of Chemical Looping Concept for Air Separation at High Temperatures. Energy and Fuels. 190-198.

[58] Wang, K., Yu, Q., Qin, Q., Duan, W., Wu, T., 2015. Study of the sorption property of copper oxygen carrier used for chemical looping air separation. Journal of Thermal Analysis and Calorimetry 1627–1633.

[59] Wang, K., Yu, Q., Qin, Q., Duan, W., 2014. Feasibility of a Co Oxygen Carrier for Chemical Looping Air Separation: Thermodynamics and Kinetics. Chemical Engineering Technology. 1500-1506.

[60] Zhou, C., Shah, K., Song, H., Zanganeh, J., Doroodchi, E., Moghtaderi, B., 2015. Integration Options and Economic Analysis of an Integrated Chemical Looping Air Separation Process for Oxy-fuel Combustion. Energy and Fuels. 1741-1755.

[61] Contreras, J. L., Fuentes, G. A., 2012 Sintering of Supported Metal Catalysts, Sintering - Methods and Products, Dr. Volodymyr Shatokha (Ed.), ISBN: 978-953-51-0371-4.

[62] Werther, J., Reppenhagen, J., 1999. Catalyst Attrition in Fluidized-Bed Systems. AIChE Journal. 2001-2010.

[63] Rydén, M., Moldenhauer, P., Lindqvist, S., Mattisson, T., Lyngfelt, A., 2014. Measuring attrition resistance of oxygen carrier particles for chemical looping combustion with a customized jet cup. Powder Technology. 75-86.

[64] Barthoolomew, C. H., Weatherbee, G. D., Jarvi, G.A., 1979. Sulfur Poisoning of Nickel

Methanation Catalysts I. In Situ Deactivation by H_2S of Nickel and Nickel Bimetallics. Journal of Catalysis. 257-269.

[65] Frick, V., Rydén, M., Leion, H., 2016. Investigation of Cu–Fe and Mn–Ni oxides as oxygen carriers for chemical-looping combustion. Fuel Processing Technology. 30-40.

[66] Guo, Q., Yang, M., Liu, Y., Yang, Q., Zhang, Y., 2016. Multicycle Investigation of a Sol-Gel-Derived Fe_2O_3/ATP Oxygen Carrier for Coal Chemical Looping Combustion. AIChE Journal. 996-1006.

[67] Mohamed, S. A., Quddus, M. R., Razzak, S. A., Hossain, M. M., de Lasa, H. I., 2015. Fluidizable NiO/Ce-γAl_2O_3 Oxygen Carrier for Chemical Looping Combustion. Energy & Fuels. 6095−6103.

[68] Abad, A., Adánez, J., García-Labiano, F., de Diego, L. F., Gayán, P., 2010. Modeling of the chemical-looping combustion of methane using a Cu-based oxygen-carrier. Combustion and Flame 602–615.

[69] Bakare, I. A., Mohamed, S. A., Al-Ghamdi, S., Razzak, S. A., Hossain, M. M., de Lasa, H. I., 2015. Fluidized bed ODH of ethane to ethylene over VOx–MoOx/c-Al_2O_3 catalyst: Desorption kinetics and catalytic activity. Chemical Engineering Journal 207–216.

[70] Hossain, M. M., de Lasa, H. I., 2010. Reduction and oxidation kinetics of Co–Ni/Al_2O_3 oxygen carrier involved in a chemical-looping combustion cycles. Chemical Engineering Science. 98-106.

[71] Xu, Z., Zhao, H., Wei, Y., Zheng, C., 2015. Self-assembly template combustion synthesis of a core–shell CuO@TiO_2–Al_2O_3 hierarchical structure as an oxygen carrier for the chemical-looping processes. Combustion and Flame. 3030-3045.

CHAPTER TWO: Synthesis and study of metal-based oxygen carriers (Cu, Co, Fe, Ni) and their interaction with supported metal oxides (Al_2O_3, CeO_2, TiO_2, ZrO_2) in a chemical looping combustion system

Energy 138 (2017) 873-882

2.1. Presentation of the article

This paper provides a detailed and comprehensive study of the monometallic oxygen carriers for the methane fuel chemical looping combustion process. The synthesized samples were Cu/Al_2O_3, Cu/CeO_2, Cu/TiO_2, Cu/ZrO_2, Co/Al_2O_3, Co/CeO_2, Co/TiO_2, Co/ZrO_2, Fe/Al_2O_3, Fe/CeO_2, Fe/TiO_2, Fe/ZrO_2, Ni/Al_2O_3, Ni/CeO_2, Ni/TiO_2, and Ni/ZrO_2. All samples were synthesized using the incipient wetness impregnation technique and tested for their BET surface area, XRD, TGA oxygen capacity, and TGA oxidation and reduction reactions. Two kinetic models were adopted and verified before estimating the kinetic parameters for all samples. The effect of various operating conditions on the reactivity of all samples was tested, such as initial sample weight, methane concentration, transition phases, and temperature. The results showed that interaction between precursors (Ni & Co) and alumina support existed and resulted in forming intermediate phases $CoAl_2O_4$ and $NiAl_2O_4$ that the $CoAl_2O_4$ successfully reduced but the $NiAl_2O_4$ did not reduce. Moreover, as the temperature increased, the oxidation reaction rate decreased but the reduction reaction rate increased for all samples. The highest reported oxygen capacities for all samples were between 900°C and 950°C.

The majority of this work was conducted by Tijani, M. M., including the design of experiments, testing, calculations, and interpretation of results. Aqsha A. provided suggestions and assisted in the analytical interpretation. Prof. Mahinpey supervised, advised and refined this work.

Synthesis and study of metal-based oxygen carriers (Cu, Co, Fe, Ni) and their interaction with supported metal oxides (Al_2O_3, CeO_2, TiO_2, ZrO_2) in a chemical looping combustion system

This article has been published in Energy Journal 138 (2017) 873-882. Reprinted with permission.

Mansour Mohammedramadan Tijani[a], *Aqsha Aqsha*[b] *& Nader Mahinpey*[a]

[a] Department of Chemical and Petroleum Engineering, Schulich School of Engineering, University of Calgary, Calgary, AB, T2N 1N4, Canada

[b] Department of Chemical Engineering, Faculty of Engineering, Universiti Teknologi PETRONAS, 32610 Seri Iskandar, Perak Darul Ridzuan, Malaysia

2.2. Abstract:

Methane-fueled chemical looping combustion was investigated using transition metals (Cu, Co, Fe, Ni) that were deposited on support oxides (Al_2O_3, CeO_2, TiO_2, ZrO_2) as oxygen carriers to find potential oxygen carrier candidates that had less interaction between the active-sites and supports. Less interaction between the active-sites and supports could help increasing the selectivity of CO_2 among other gases (CO, H_2) and to reduce the solid inventories in the CLC reactor system. The results showed that the average particle size for the synthesized samples was in the range of 8 to 119 nm. The effect of the sample initial weight in the TGA showed no significant effect on the oxidation/reduction reactions of metals. As the CH_4 concentration increased, the reduction rate of oxygen carriers and coke formation increased. Highest oxygen detachment of supported oxygen carriers was reported to be 3.12% for Cu/CeO_2 at 900°C, 6.14% for Co/TiO_2 at 950°C, 6.83% for Fe/CeO_2 at 950°C, and 5.00% for Ni/CeO_2 at 950°C. Support

oxides showed a significant effect on the oxidation and reduction activation energies, where Cu/Al_2O_3, Co/CeO_2, Fe/ZrO_2, and Ni/ZrO_2 samples showed an improved performance among other combinations.

2.3. Introduction

The oxy-fuel combustion process is a technique used to capture CO_2 that involves burning fuel, such as natural gas, in a pure oxygen environment. The oxy-fuel combustion process eliminates the formation of nitrogen oxides (NOx) and other pollutants, reduces the fuel consumption rate by increasing the flame temperature [1]. Chemical looping combustion (CLC) uses solid oxygen carriers and produces a concentrated stream of CO_2 due to the combustion of fuel with pure oxygen. It is an example of an oxy-fuel combustion process that has the potential to be a cost-effective, efficient, and clean technology. The oxygen carriers play a crucial role in the CLC system. They are required to have very high reactivity and stability during the CLC oxidation/reduction cycles. For example, the oxidation/reduction of an oxygen carrier should be accomplished with short residence time (<11s) [2] & [3] to achieve a high fuel conversion rate. The most widely used oxygen carriers used in the past decade were supported metal-based materials. There are two common ways to study the reactivity of oxygen carriers for chemical looping application, lab-scale reactor and thermogravimetry analyzer (TGA).

Lab-scale demonstration for chemical looping combustion was reported by Mohamed *et al* [5] in which the contact time of 60s for $NiO/Ce\text{-}Al_2O_3$ sample in CH_4 fueled system at 650°C resulted in more than an 80% conversion of NiO. Abad *et al* [6] mentioned that with only 14 wt% of active-site on the CuO grain, the optimum ratio of oxygen carrier to fuel was between 1.7 and 4 with a combustion efficiency of 99.9% at 700°C. Bakare *et al* [7] studied the kinetics of VOx-

$MoOx/Al_2O_3$ as an oxygen carrier in a C_2H_6 fueled fluidized-bed reactor where it was found that a temperature of 650°C and residence time of 30s favoured COx among other gases. Investigation of $Co\text{-}Ni/Al_2O_3$ kinetics was reported by Hossain and Lasa [8] where both oxidation and reduction kinetics followed the nucleation and nuclei growth model when the temperature ranged between 550°C to 650°C, and activation energies were found to be 44 kJ/mol and 45 kJ/mol for the oxidation and reduction reactions, respectively. Investigation of mixed metal-based oxygen carriers was performed by Frick *et al* [3] using Fe-Cu and Mn-Ni metals where the average CO_2 yields of >90% observed at 1050°C for Fe-Cu sample, and the CO_2 yield for Mn-Ni sample was >85% at 1050°C. Xu *et al* [9] reported the highest oxygen capacity of 7.8 wt% was observed with a $CuO_{77.5\%}/TiO_{2_{5\%}}Al_2O_{3_{17.5\%}}$ sample. They also reported that the addition of TiO_2 prevented CuO and Al_2O_3 from the interacting and the CuO grains from agglomerating on the mixed support oxides. Guo *et al* [4] synthesized Fe-based oxygen carriers using sol-gel method where a surface area of 4.92 m^2/g was estimated and a high CO_2 selectivity greater than 95% was observed.

Thermogravimetric analyzer (TGA) are primarily used to study CLC process of gaseous fuels. The reaction order, activation energy, and numerous other kinetics/behaviours can be estimated using TGA. Study on the reactivity of Cu-based oxygen carriers (800°C-950°C) in a TGA was reported by Donat *et al* [10] where the maximum oxygen capacity of 8.04% was estimated, and an early reduction in the cyclic performance due to the agglomeration of the support ($CaO\text{-}Al_2O_3$) was observed. Oxygen capacity of 8.02 wt% at 800°C for $SrCuO_2$ was reported by Ksepko [11] in a TGA. Wang *et al* [12] reported that the influence of temperature on the CH_4 reduction of Chinese sulfur-containing lean iron ore was significant as a reaction temperature of 800°C showed a 22% conversion, while a temperature of 950°C resulted in a 95% conversion, and as the CH_4 concentration increased from 50% to 100%, increases in the conversion were observed

(37% to 55%); however, coke formation was only noticeable at 50% and 100% CH_4 concentrations. Monazam *et al* [13] described the reduction of Cu-ferrite to Cu was chemically controlled, while Cu-ferrite to Cu-Fe_3O_4 and Cu-Fe were found to be controlled by the nucleation and growth model. The activation energies for the reductions of CuO-ferrite to Cu-ferrite, Cu-ferrite to Cu-Fe_3O_4, and CuO-ferrite to Cu-Fe were approximately 55.32 kJ/mol, 70 kJ/mol, and 165 kJ/mol. Study of manganese minerals was performed by Mei *et al* [14] where it was shown all samples started losing their reactivity after the 10^{th} cycle, which was then attributed to the reformation of particles and/or the production of fine particles during the oxidation/reduction reactions.

Previous studies on the reactivity of oxygen carriers using both lab-scale reactor and TGA have shown some challenges related to agglomerations, high attrition index, and interaction between the active-sites and supports. It has also been demonstrated that some oxygen carriers such as iron and manganese are abundant and considered non-toxic to the environment, yet their oxygen capacity is low (3-10%) compared to others. Other carriers such as cobalt and nickel have relatively high oxygen capacity (21-27%) but considered expensive with some concerns related to their effects on health and safety. Hence, there is a need to study supported transition metals such as Cu, Co, Fe, and Ni oxygen carriers using low loading percent to maximize their reactivity in the CLC process. Therefore, the aim of this study is to investigate the limit of oxygen intake of single metal (Cu, Co, Fe, Ni) deposited with low loading percent (10%) on single support (Al_2O_3, CeO_2, TiO_2, ZrO_2). This investigation will help finding effective oxygen carriers that possess minimal interaction between the active-sites and supports as well as reduce possible interaction between the active-sites and supports. The optimal oxygen carriers may be used in the CH_4 fueled CLC

process to increase the selectivity of CO_2 among other gases (CO, H_2), and to reduce the solid inventories in the CLC reactor system.

2.4. Materials and Methods

The active-sites (i.e. Cu, Co, Fe, Ni) in this study were prepared using nitrate forms such as copper nitrate trihydrate ($Cu(NO_3)_2.3H_2O$), cobalt nitrate hexahydrate ($Co(NO_3)_2.6H_2O$), iron nitrate nonahydrate ($Fe(NO_3)_3.9H_2O$), and nickel nitrate hexahydrate ($Ni(NO_3)_2.6H_2O$). These nitrates were purchased from Sigma Aldrich Canada and used without any modification. The metal support oxide CeO_2 (99.995%) was also purchased from Sigma Aldrich Canada. The other metal support oxides, Al_2O_3 (γ-alumina, 99.9%), TiO_2 (99.5%), and ZrO_2 (99.5%), were purchased from Alfa-Aesar. All the support oxides were used without any modification. The metal-based oxygen carriers were prepared by the incipient wetness impregnation technique with a respective active-site in an aqueous solution. The metal loading percent used in this study was 10% for all samples except for the denoted samples with Cu, Co, Fe, and Ni where the support oxides were not used (i.e. pure metals). First, a suspension aqueous solution of a support oxide in a metal active-site was stirred on a hot plate/magnetic stirrer at 75°C until the water completely evaporated. The sample was then conventionally oven dried at 120°C for 12 hrs. The dried sample was calcined in air at 500°C for 3 hrs to obtain the oxide forms such as CuO and CoO. Lastly, the reduction of the samples was conducted by passing hydrogen gas through a tubular reactor at 350°C for 3 hrs.

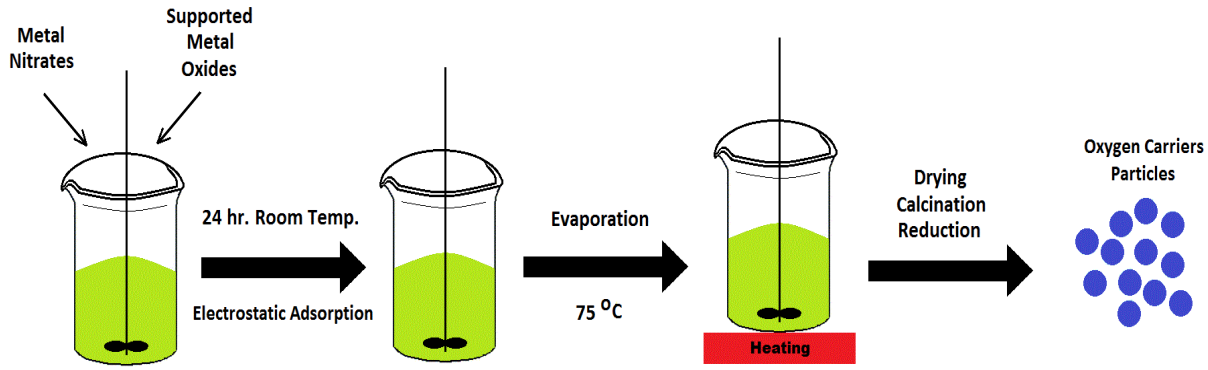

Fig. 2.1. Steps in wetness impregnation technique.

Characterizations, such as BET surface area and porosimetry of oxygen carriers, were estimated using the Micrometrics 2020 ASAP instrument. Prior to the analysis, the samples were degassed at 120°C for 2 hrs to remove any surface-adsorbed moisture. Then, the mesoporous adsorption/desorption analysis was performed using nitrogen gas in a liquid nitrogen bath. The X-ray diffraction (XRD) analysis was conducted using a Rigaku ULTIMA III X-ray diffractometer with Cu K-alpha radiation as the source of the X-rays. The oxygen carriers were scanned with 2-theta equal to 20-80, a 0.05 degree step, and a counting time of 2.0 degrees per minute operating at 40 kV and 44 mA to determine the full diffractogram of the metal oxygen carriers.

The oxygen capacity of the reduced oxygen carriers was investigated using the TGA model TG 209 F1 Libra. The reduced samples were first loaded on a Al_2O_3 crucible and placed inside the TGA instrument to determine the maximum oxygen capacity. The temperature was then raised to achieve the desired oxidation condition (800°C–950°C) using a nitrogen flow rate of 20 ml/min and a heating rate of 100 °C/min. The sample was then exposed to air with a flow rate of 20 ml/min allowing the oxidation reaction to take place. The samples' weight changes over time were recorded and saved for further evaluation.

The chemical looping oxidation/reduction reactions were carried out using the same TGA. After the reduced sample was loaded in the crucible, the temperature was increased from 800°C to 950°C at a rate of 100°C/min in nitrogen (20 ml/min), and the sample was then exposed to air (20 ml/min) to conduct the oxidation reaction and methane gas (40 vol% balanced with nitrogen) to conduct the reduction reaction. Nitrogen gas was purged for three minutes between each oxidation and reduction segment to avoid the mixing of air and methane gases. The oxidation and reduction segments were repeated three and two times, respectively. The typical CLC profile of methane in which synthesized metal-based materials were utilized as oxygen carriers is shown in Fig. 2.2. The weight gain corresponds to the sorption of oxygen (oxidation), while the weight loss is a result of the desorption of oxygen. The decrease in conversion in the second cycle is mainly attributed to the deposition of coke after the CH_4 reduction reaction, which reduces the oxygen transfer capability during the second oxidation reaction.

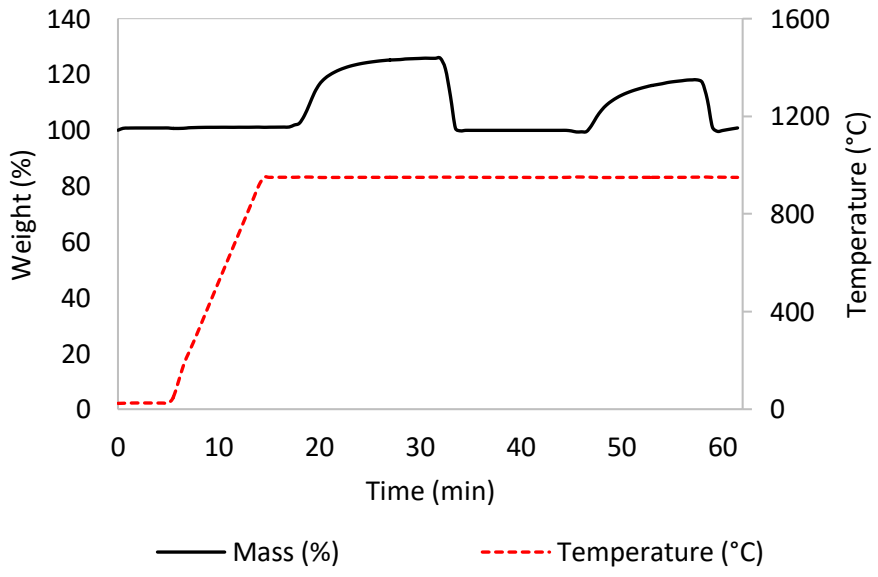

Fig. 2.2. Typical TG profile for CH_4 CLC process (two oxidation/reduction cycles).

The effect of the initial weight of sample and CH_4 concentration on the oxidation and reduction reactions was investigated only using Co, Cu, Fe, and Ni metals to determine the optimal operation conditions for other supported metal-based oxygen carriers in the TGA CLC system. All TGA experiments in this paper were at least duplicated. The uncertainty was found to be $\pm$ 2.12 wt%.

2.5. Results and Discussion

2.5.1. Oxygen carrier characterizations

The surface area of Co, Fe, and Ni (Fig. 2.3a) decreased after the reduction experiment, while the surface area of Cu (Fig. 2.3a) slightly increased after the reduction experiment. The Al_2O_3 support (Fig. 3b) reported the highest surface area among the supports. A small variation in the surface areas of fresh and reduced supported oxygen carriers (Fig. 2.3c) was observed for all samples except Co/ZrO_2 and Co/TiO_2, which showed increases of 33.85% and 47.84%, respectively. Fe/TiO_2 and Ni/ZrO_2, however, showed decreases of 26.17% and 22.97%, respectively. The average pore volume (Fig. 2.3d) of fresh and reduced supported oxygen carriers were also estimated using the 2020 ASAP instrument. Decreases in the pore volume were observed with Co, Fe, and Ni samples (86.61%, 47.47%, and 90.38%, respectively) but Co/ZrO_2 sample showed an increase of 53.32% in the pore volume. The reason for the changes in the surface areas/ pore volume of these metals could be attributed to the agglomeration of particles that took place after the reduction experiment, which may have stabilized the oxygen-free phases of these metals. A decrease in the surface area of the oxygen carriers after the reduction experiment was reported elsewhere [3], [15] & [16]. The Co/ZrO_2 oxygen carrier showed an increased surface area

(53.85%) compared to those reported in [17]. The uncertainty of BET surface area and porosimetry analyses using Micrometrics 2020 ASAP were found to be $\pm$ 7.12%.

The XRD analysis for oxygen carrier metals (Co, Cu, Fe, Ni) supported with metal oxides (Al_2O_3, CeO_2, TiO_2, ZrO_2) showed a complete reduction of copper supported with alumina, ceria, and zirconia was observed (please refer to Supplementary Material Fig. 1) as CuO was completely reduced into a Cu phase. However, copper supported with titania did not show any significant phase changes between the fresh and reduced samples. The phases in the fresh sample of Co/Al_2O_3 (Supplementary Material Fig. 2.2) were Co_3O_4, Al_2O_3, and $CoAl_2O_4$, while the reduced sample showed only CoO and Al_2O_3 phases. Interactions between cobalt and aluminum oxide occurred and resulted in the formation of $CoAl_2O_4$ in the fresh sample. The fresh sample of Co/CeO_2 showed Co_3O_4 and CeO_2 phases, while the reduced sample showed Co and CeO_2, which indicated a complete reduction. The cobalt sample supported by titania and zirconia showed only a Co_3O_4 phase in the fresh samples, and no cobalt metal was found in the reduced samples. This result was due to either perfect dispersion, or the cobalt metal, completely covered by titania or zirconia, was not detectible by the XRD.

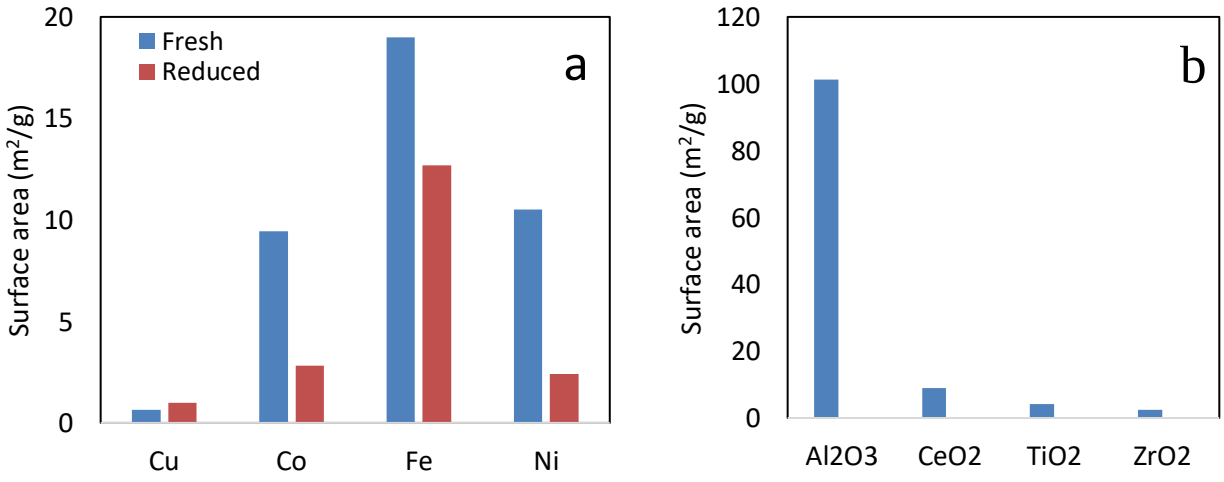

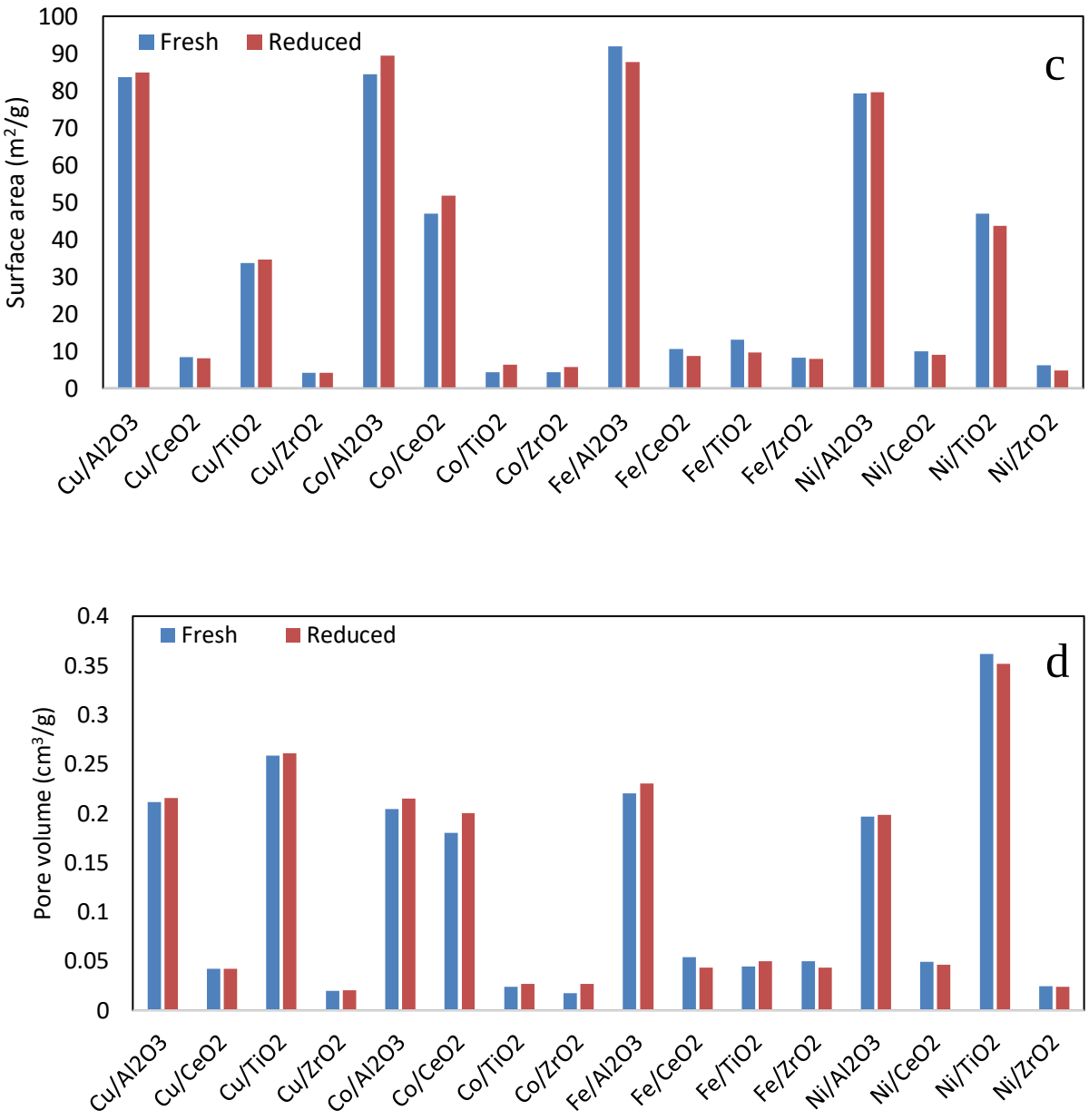

Fig. 2.3. BET surface area and porosity: (a) metals surface area, (b) supports surface area (c) metals deposited on supports surface area, (d) metals deposited on supports pore volume.

Iron (Supplementary Material Fig. 2.3) supported with aluminum oxide showed Fe_2O_3 and Fe_3O_4 phases in both the fresh and reduced samples. A reduction of iron from Fe_2O_3 to FeO and

Fe was observed in the iron supported sample with cerium oxide. A partial reduction of Fe_2O_3 to Fe_3O_4 was found in the iron sample supported with titania. A complete reduction of iron from Fe_2O_3 to Fe occurred in the iron sample supported with zirconium oxide. The phases that occurred in the fresh sample of Ni/Al_2O_3 (Supplementary Material Fig. 2.4) were NiO, Al_2O_3, and $NiAl_2O_4$, while the reduced sample showed Ni, NiO, $NiAl_2O_4$, and Al_2O_3 phases. Interactions between nickel and aluminum oxide occurred and resulted in the formation of $NiAl_2O_4$ phase. A complete reduction of NiO to Ni was observed in the nickel samples supported with ceria and zirconia, while a partial reduction of NiO to Ni was found in the nickel sample supported with titania. The support ZrO_2 facilitated a complete reduction of all active-site metals. This result was due to either high thermal stability of ZrO_2 (m.p. 2,715°C) compared to other support oxides, or absence of possible phase transition of ZrO_2 that could occur in this experimental condition compared to Al_2O_3 and CeO_2 supports. The average particle sizes of all samples were estimated using the Scherrer equation and are shown in Table 2.1.

The average particle size of aluminum oxide was not calculated because it was less than 1 nm in diameter (Supplementary Material Figs. 1-4). Because the diameter was small, noises were induced which contributed to a high degree of uncertainty associated with determining FWHM. The ceria, titania, and zirconia supports showed high average particle sizes compared to the deposited active phases, which could explain the low BET surface area for those supports. However, the reduced pure metals (i.e. Co, Cu, Fe, Ni) reported larger sizes than the oxidized forms. This result could be due to the agglomeration of pure metals, which resulted in the enlargement of the grains, and thus, a high average particle size. The uncertainty of crystalline domain size for metal-based oxygen carriers was in the range of $\pm$ 14.30%.

Table 2.1 Crystalline domain size for metal-based oxygen carriers

Sample	Phase	Average particle size (nm)
Cu/Al_2O_3	CuO	28
	Cu	69
Cu/CeO_2	CuO	20
	Cu	80
	CeO_2	47
Cu/TiO_2	CuO	14
	TiO_2	38.5
Cu/ZrO_2	CuO	13
	Cu	61
	ZrO_2	57
Co/Al_2O_3	$CoAl_2O_4$	9
Co/CeO_2	Co_3O_4	13
	Co	13
	CeO_2	12
Co/TiO_2	Co_3O_4	13
	TiO_2	119
Co/ZrO_2	Co_3O_4	15
	ZrO_2	54
Fe/Al_2O_3	Fe_3O_4	20
	Fe_2O_3	21
Fe/CeO_2	Fe_2O_3	20
	FeO	8
	Fe	39
	CeO_2	46.5
Fe/TiO_2	Fe_3O_4	27
	Fe_2O_3	23
	TiO_2	116
Fe/ZrO_2	Fe_3O_4	24
	ZrO_2	59
Ni/Al_2O_3	NiO	10
	Ni	8.5
Ni/CeO_2	NiO	27
	Ni	32
	CeO_2	47
Ni/TiO_2	NiO	10
	Ni	13
	TiO_2	35.5
Ni/ZrO_2	NiO	23
	Ni	31
	ZrO_2	54

The differences and similarities among the synthesized oxygen carriers are as follows:

- The addition of Al_2O_3 to metals successfully reduced the CuO and Co_3O_4 oxides to Cu and Co metals; however, for iron sample, no reduction occurred and the nickel sample interacted with Al_2O_3 which resulted in forming $NiAl_2O_4$ phase, which was not reducible under our experimental condition.
- The ceria support helped reducing the CuO, Co_3O_4 and NiO oxides to their metal forms but partial reduction was noticed with Fe sample.
- The titania support showed significant effect on the reduction of copper, iron and nickel samples where no reduction to metals or partial reduction was observed. The Co/TiO_2 was completely reduced to Co metal in which cobalt metal was completely covered by titania.
- The zirconia support help reducing all oxidized samples to their metal forms without showing any interaction between metals and supports.

2.5.2. Study of Chemical Looping Combustion using TGA

2.5.2.1. Effect of initial weight of sample on the oxidation/reduction reactions

The effect of the initial weight of the oxygen carriers was studied using TGA to address whether mass transfer had an effect on the oxidation/reduction reactions of metal-based oxygen carriers. Four initial sample weights (5 mg, 10 mg, 15 mg, and 20 mg) of each pure metal were selected to be tested in the TGA at 850°C and 40 vol% CH_4.

The sample with an initial weight of 5 mg showed a slight increase in the rate of oxidation followed by 10 mg, 15 mg and 20 mg samples' weight for each of Cu (Fig. 2.4 a & b), Co (Fig. 2.4 c & d), Fe (Fig. 2.4 e & f), and Ni (Fig. 2.4 g & h), as shown in the TG/DTG curves. However, during the reduction reaction, no significant difference was noticed when the initial weights of the samples were varied except for Co and Fe. The 20 mg Co sample was reduced 2s faster than the

other weights, and the 5 mg sample showed a slight increase (3.82%) in the reduction rate. The variation in the oxidation reaction rates with different sample initial weights could be attributed to the mass transfer effect. As the initial weight of the samples increased, the reactant gases (i.e. air, CH_4), encountered increased resistance to diffuse inside the reactive layer of the oxygen carriers. Consequently, as the initial weight of the samples increased, reactivity decreased. Similar results also reported by San Pio *et al* using Cu-based oxygen carrier [18].

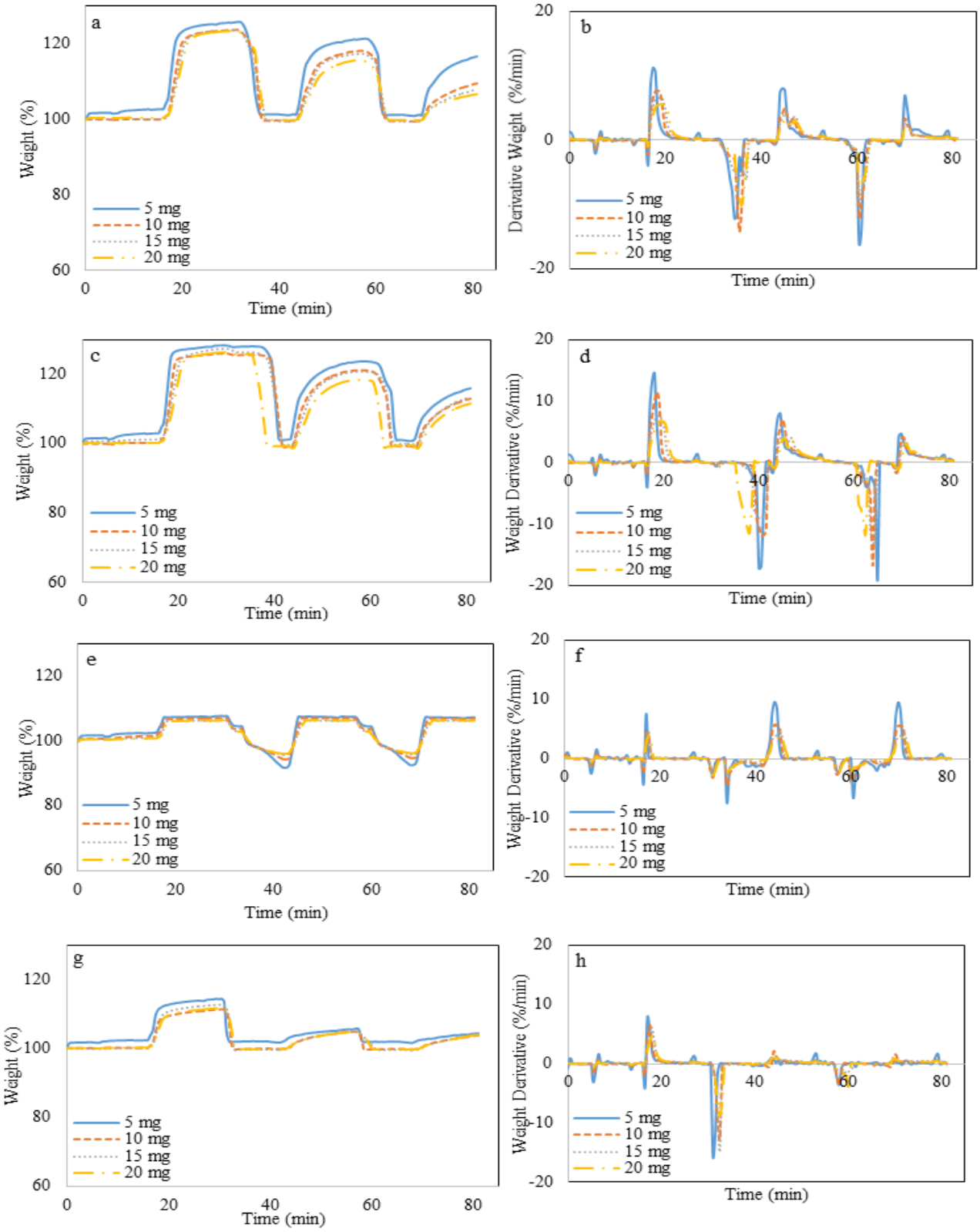

Fig. 2.4. TGA-CLC reactions at 850 °C and 40 vol.% CH_4 concentration using different metals, Cu: (a) TGA, (b) DTG, Co: (c) TGA, (d) DTG, Fe: (e) TGA, (f) DTG, and Ni: (g) TGA, (h) DTG.

2.5.2.2. The effect of CH_4 concentration on the reduction reaction

The effect of methane concentration (10 vol%, 20 vol%, 30 vol%, and 40 vol% balanced with N_2) on the reduction reaction of Cu, Co, Fe, and Ni was investigated in TGA. The results showed that as the methane concentration increased, the conversion of metals increased for Cu, Co, Fe, and Ni. No solid reduction was observed when cobalt was used as an oxygen carrier (Figs. 5c and d) when 10% CH_4 concertation was employed. Further, the first reduction peaks on the DTG curve of Cu (Fig. 2.5b) and Ni (Fig. 2.5h) were greater than the second reduction peak. This finding could be due to the deposition of carbon on the surface of these metals, which potentially reduced the second oxidation reaction rate and thus, the second reduction reaction. Negligible peak gains and losses (< 0.1%) that corresponded to carbon deposition were observed on the DTG curve (Fig. 2.5f) for Fe. Carbon deposition on Cu increased by 0.21%, 3.58%, 3.31%, and 4.44% for the CH_4 concentrations of 10 vol.%, 20 vol.%, 30 vol.%, and 40 vo.%, respectively. Carbon deposition on Co increased by 0.26%, 5.70%, 6.12%, and 3.85% for the CH_4 concentrations of 10 vol.%, 20 vol.%, 30 vol.% and 40 vo.%, respectively. Carbon deposition on Ni increased by 2.44%, 6.36%, 8.33%, 7.08% for the CH_4 concentrations 10 vol.%, 20 vol.%, 30 vol.% and 40 vol.%, respectively. The reason for the increase in the carbon deposition as CH_4 concentration increased was mainly due to the occurrence of methane thermal decomposition after complete reduction of oxygen carriers which resulted in depositing carbon and released hydrogen gas. Thus, as the CH_4 concentration increased, decomposition of methane increased, which then led to increase in the carbon deposition on copper, cobalt and nickel samples. Similar explanation was reported elsewhere [2]. Iron on the other hand, showed no significant carbon formation on its particles which showed good agreement with other reported study [19]. Therefore, increasing the methane

concentration favoured the carbon deposition on copper, cobalt and nickel metals; however, iron metal showed no sign of carbon deposition.

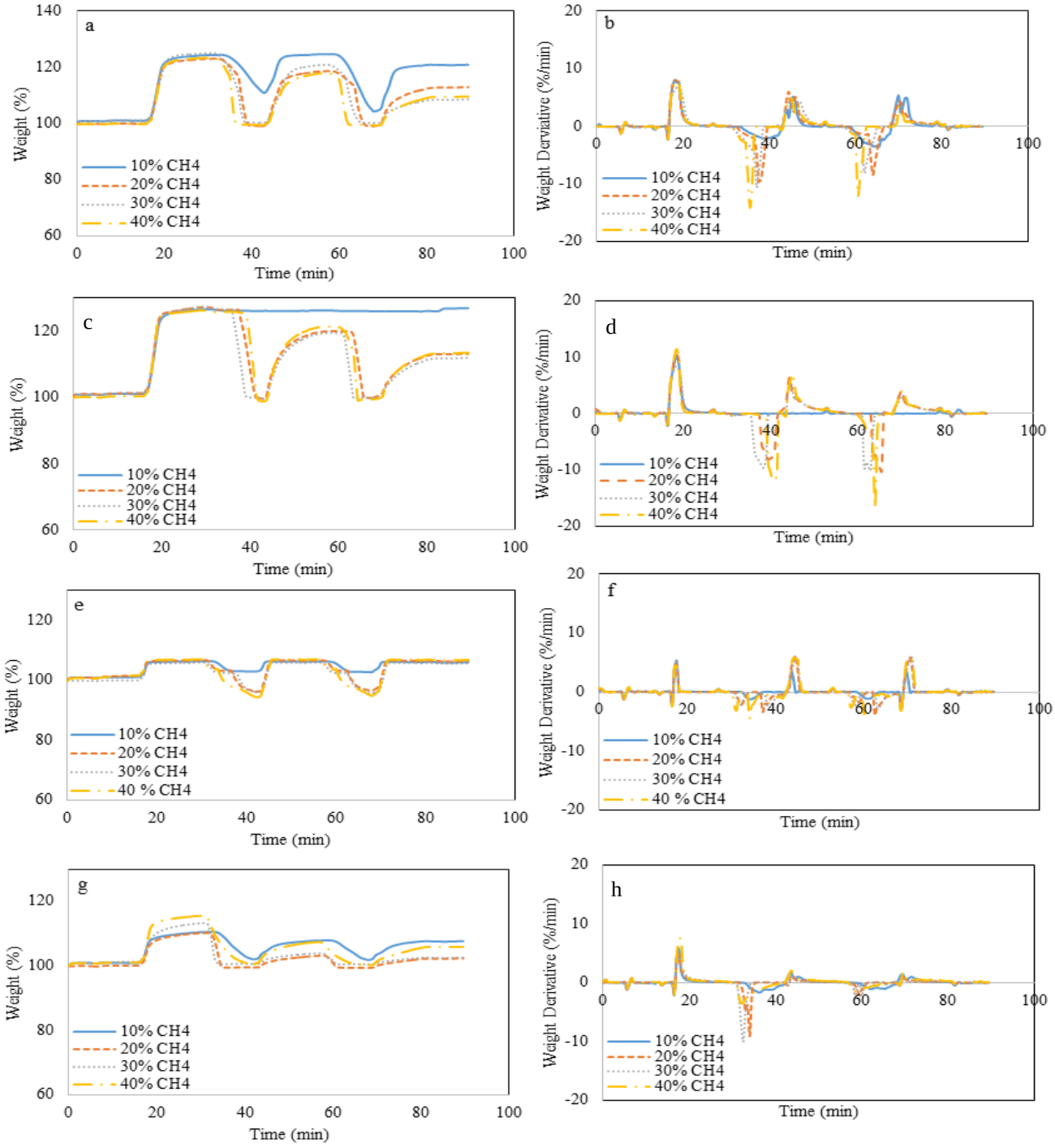

Fig. 2.5. TGA-CLC reactions at 850 °C and 10 mg sample initial weight using different metals, Cu: (a) TGA, (b) DTG, Co: (c) TGA, (d) DTG, Fe: (e) TGA, (f) DTG, and Ni: (g) TGA, (h) DTG.

2.5.2.3. Maximum oxygen capacity of metals and supported metal-based oxygen carriers

The theoretical oxygen capacity was calculated using the following equation.

$$\text{oxygen capacity} = \frac{k\,W_O}{W_{O.O.C}} \tag{2.1}$$

where: W_O is the weight of detached oxygen (mg), $W_{O.O.C}$ is the weight of fully oxidized oxygen carrier (mg); and, k is the oxygen detachment factor (-). Eq. (2.1) was used to calculate the theoretical oxygen capacity of the metals; the theoretical and experimental values were then compared. The results are shown in Fig. 2.6. The temperature affected the oxygen capacity of all metals. Slight effects were observed in the Cu and Ni samples. The highest oxygen capacity of Cu was 19.60% at 850°C; while for Ni was 13.19% at 800°C. The highest oxygen sorption was observed at 900°C for Co (25.53%), while the highest O_2 sorption for Fe (23.44%) was observed at 950°C.

The oxygen capacities of the supported metals oxides are shown in Figs. 7-10. Temperature had a slight effect on the Cu/Al_2O_3 sample (Fig. 2.7) where the highest oxygen capacity was 2.05% at 950°C. However, Cu/CeO_2 showed a maximum oxygen capacity of 3.12% at 900°C followed by 2.82%, 2.63%, and 2.44% at 850°C, 800°C and 950°C, respectively. Cu/TiO_2, showed no significant effect when the temperature was raised from 800°C to 900°C, but at 950°C, the lowest oxygen capacity of 1.73% was recorded. Cu/ZrO_2 had maximum oxygen capacity at 850°C, but the oxygen capacity decreased as the temperature increased from 850°C to 950°C.

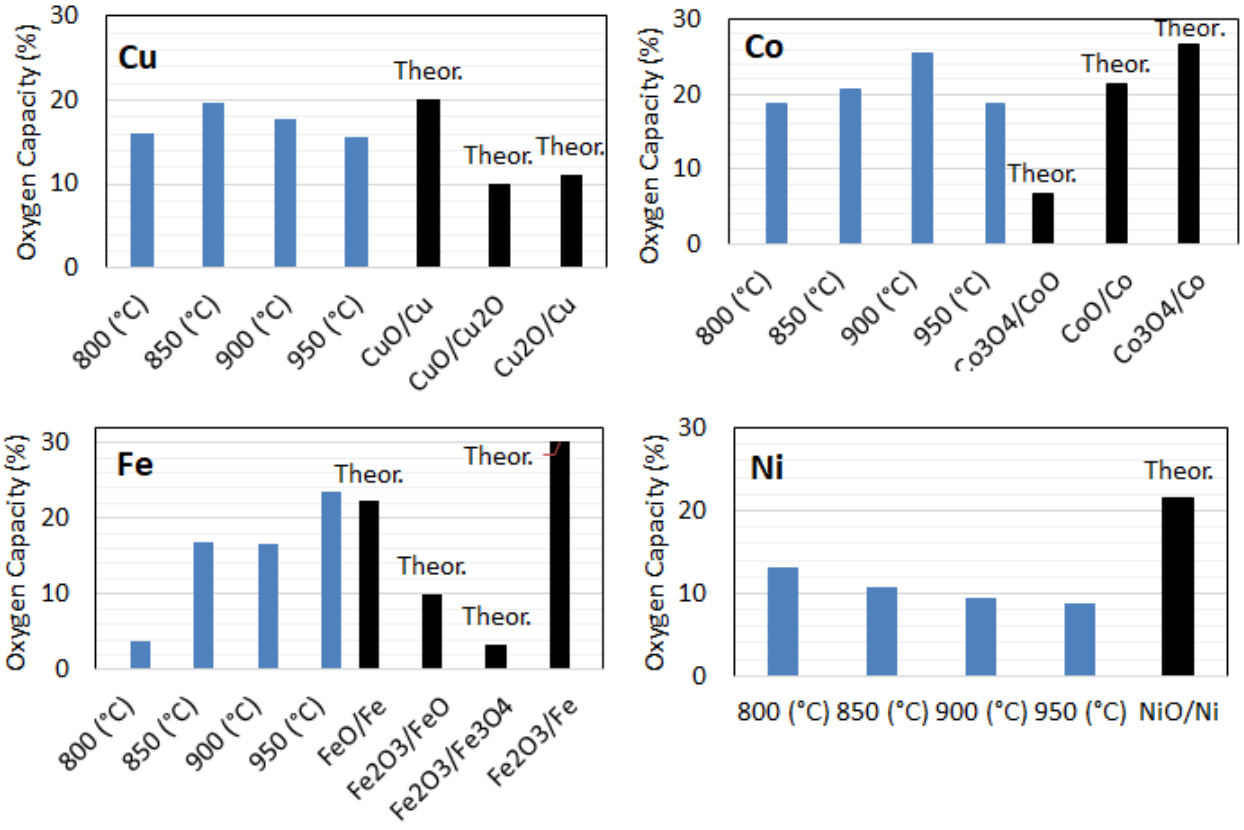

Fig. 2.6. Maximum oxygen capacity for Cu, Co, Fe, Ni using 10 mg initial sample weight and 40 vol.% CH_4 concentration.

Both Co/Al_2O_3 and Co/CeO_2 (Fig. 2.8) increased in oxygen capacity as the temperature increased from 800°C to 950°C. The maximum oxygen capacity reached 1.92% at 950°C for Co/Al_2O_3 and 5.22% at 950°C for Co/CeO_2. Temperature had a slight effect between 800°C and 900°C on the Co/TiO_2 sample; at 950°C, the highest oxygen capacity of 6.14% was reported among other Co samples supported with TiO_2. No significant effect of temperature was observed on the Co/ZrO_2 sample.

The Fe/Al_2O_3 sample (Fig. 2.9) slightly decreased in oxygen capacity as the temperature increased; the maximum oxygen capacity was observed to be 1.28% at 850°C. A slight increase

in the oxygen capacity was observed for the Fe/CeO_2 sample as the temperature increased from 800°C to 900°C, but at 950°C, the highest oxygen capacity of 6.83% was reported among all other supported Fe-based oxygen carriers. An increase in oxygen capacity was observed for the Fe/ZrO_2 sample as the temperature increased from 800°C to 950°C; the oxygen capacity increased from 1.52% to 3.54%, respectively.

All Ni supported oxygen carriers (Fig. 2.10) increased in oxygen capacity as the temperature increased from 800°C to 950°C expect for the Ni/ZrO_2 sample where a slight effect of temperature was observed. The oxygen capacity for Ni/Al_2O_3, Ni/CeO_2, and Ni/TiO_2 increased from 0.43%, 3.05%, and 2.41% at 800°C to 2.30%, 5.00%, and 4.99% at 950°C, respectively.

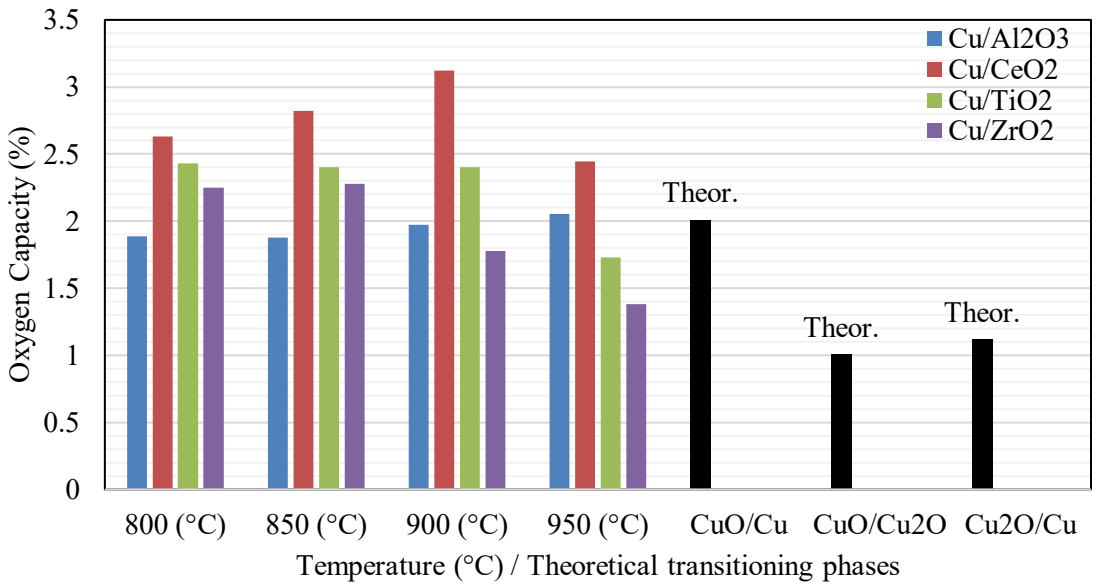

Fig. 2.7. Comparison between experimental and theoretical oxygen capacities of supported Cu-based oxygen carriers at different temperatures.

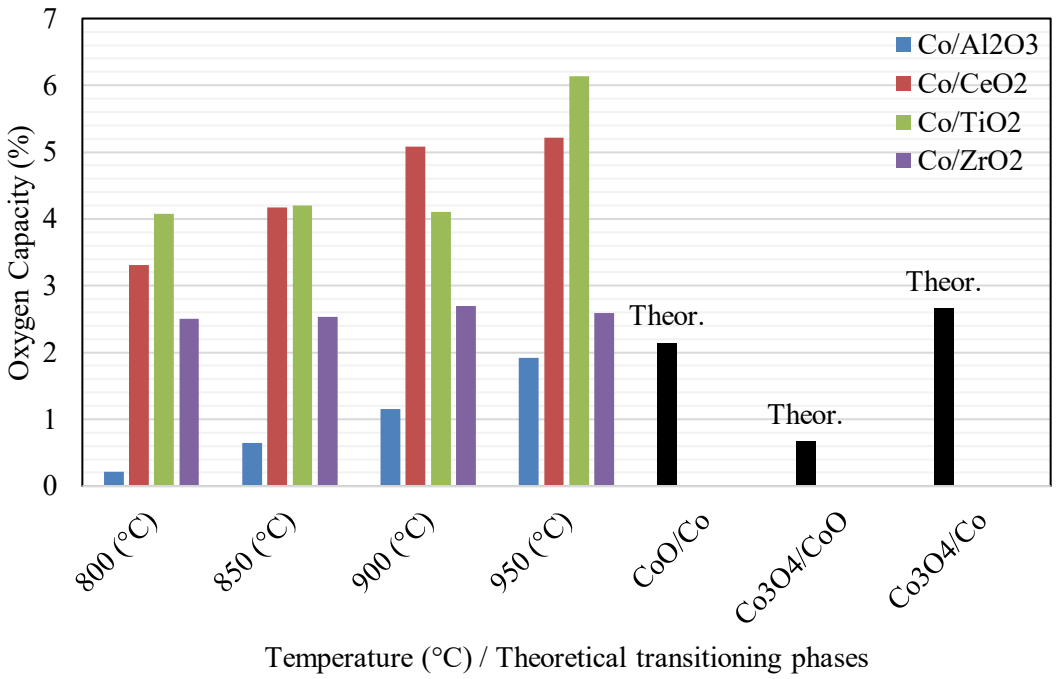

Fig. 2.8. Comparison between experimental and theoretical oxygen capacities of supported Co-based oxygen carriers at different temperatures.

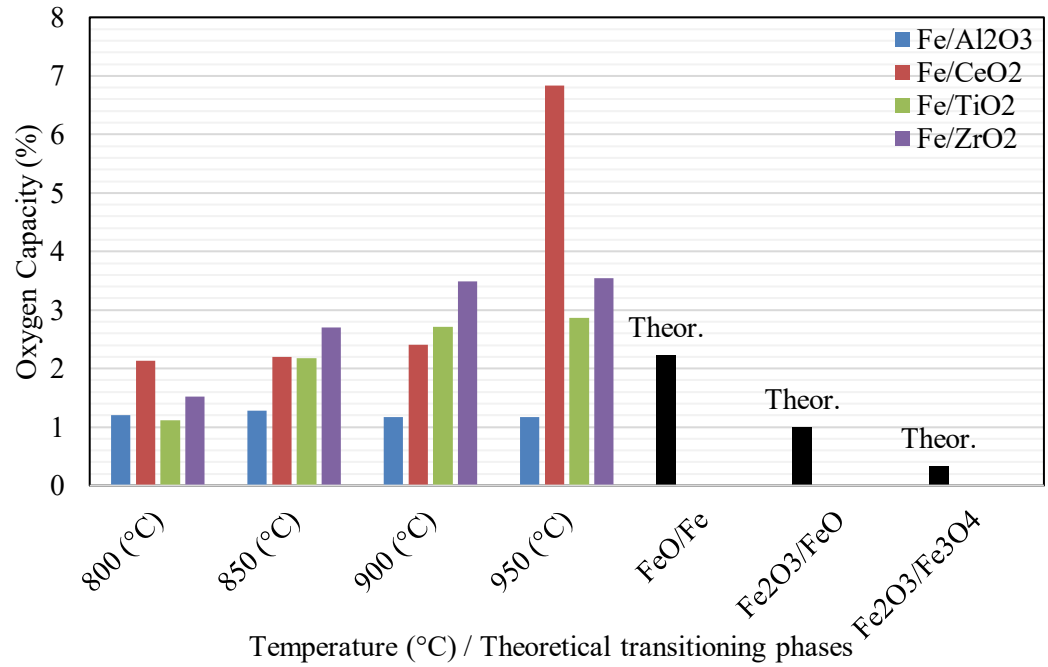

Fig. 2.9. Comparison between experimental and theoretical oxygen capacities of supported Fe-based oxygen carriers at different temperatures.

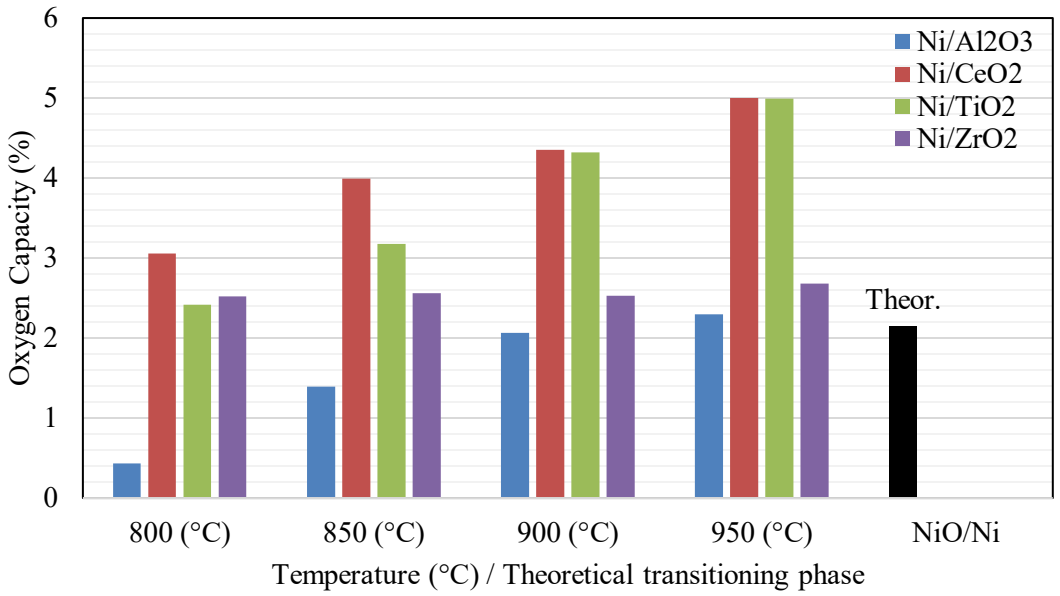

Fig. 2.10. Comparison between experimental and theoretical oxygen capacities of supported Ni-based oxygen carriers at different temperatures.

The comparison between the theoretical (black columns) and experimental oxygen capacities shows that the metal phases during the oxidation and reduction reactions for the Cu samples could be CuO/Cu, Cu/Cu_2O, and/or Cu_2O/Cu. Co could exhibit CoO/Co, Co_3O_4, Co_3O_4/Co or a combination of these phases. In contrast, Fe could consist of FeO/Fe, Fe_2O_3/FeO, or Fe_2O_3/Fe_3O_4. However, combinations of two or three phases could also occur. The active-sites phase-transitioning to different phases during the methane reduction reaction was reported elsewhere [1] & [2]. In addition, the variation in the oxygen capacity for some samples shows higher experimental O_2 sorption capacity when compared to the theoretical O_2 sorption capacity. The variation in the oxygen capacity for some samples could possibly be due to partial reduction of supports to form intermediate phases such as $CuTiO_3$ and NiCe. For supported Ni oxygen carriers, as the temperature increased, carbon was formed as intermediary product which later was

oxidized to form CO_2 [20] & [21]. This explains the higher experimental O_2 sorption capacity when supported Ni samples are used. Variation of oxygen capacity with temperature in Cu-based oxygen carriers (Fig. 2.7) was due to the formation of carbon at lower temperature (<850°C) and sintering of reduced metal particles at higher temperature (>900°C), which resulted in decreasing the reduction rate of oxygen carriers and thus their oxygen capacity [22] & [23]. However, Co, Fe, and Ni based oxygen carriers did not report significant sintering of particles at higher temperature, which resulted in an increase in the oxygen capacity as temperature increased.

2.5.2.4. The effect of reaction temperature on the conversion of solid oxygen carriers

The conversion (oxidation/reduction) of the oxygen carrier samples was calculated using the following equation:

$$X = \frac{m - m_r}{m_o - m_r} \tag{2.2}$$

where; m is the mass of sample at any time (mg), m_r is mass of the reduced sample (mg); and, m_o is the mass of the oxidized sample (mg). The conversion profiles of all oxygen carriers during the oxidation/reduction reactions are shown in Supplementary Material Figs. 5-9.

After approximately 80% oxidation conversion, the metal-based oxygen carriers experienced an internal mass transfer effect, which limited the oxidation reaction rates. Therefore, the shrinking core model is best suited to represent the estimation of oxidation reaction kinetics. The shrinking core model is defined as follows:

$$r = \frac{dX}{dt} = k_{SCM}\,(1 - X)^{2/3} \tag{2.3}$$

The experimental kinetic parameters for the reduction reaction are calculated using the proposed method, which is independent of the kinetic model [24], as follows:

$$r = \frac{dX}{dt} = k(T)\, f(X) \tag{2.4}$$

using Arrhenius equation:

$$k = k_o \exp\left(-\frac{E_A}{RT}\right) \tag{2.5}$$

Therefore [24],

$$\ln[t_X(T)] = \{\ln[G(X)] - \ln[k_o]\} + \frac{E_A}{RT}\,;\ \ln[G(X)] \ll \ln[k_o] \tag{2.6}$$

The reaction order is estimated using the rate law as follows:

$$r = k\,(1 - X)^n \tag{2.7}$$

or

$$\ln(r) = \ln\left(\frac{dX}{dt}\right) = \ln(k) + n\ \ln(1 - X) \tag{2.8}$$

where r is reaction rate (mol/g min); X is conversion (-); t is time (min.); k is the reaction rate constant ($mol^{1-n}\ g^{n-2}/min$); k_0 is the frequency factor ($mol^{1-n}\ g^{n-2}/min$); E_A is activation energy (kJ/mol); R is the universal gas constant (J/mol K); T is absolute temperature (K); t_X is residence time (min.); G(X) and f(X) are conversion dependent functions; and n is reaction order (-). It is worth mentioning that the reaction order was estimated within the first step (i.e. surface reaction step) to fit eq. (2.7) profile. However, the overall reaction order was assumed to be 2/3 according to eq. 2.3.

For the estimation of the kinetic parameters, eq. 2.2 was first used to calculate the conversion at a given temperature, then the reaction rate was calculated using the second term of eq. 2.3 (i.e. dX/dt). The shrinking core model reaction rate constant (k_{SCM}) was then calculated using a linear regression to fit the rate (dX/dt) versus ($(1 - X)^{2/3}$) with R^2 of 0.9 or higher. The previous steps were repeated for all reaction temperatures to find (k_{SCM}) at every temperature. Finally, the linear regression of (k_{SCM}) versus reciprocal of temperature gave the activation energy and frequency factor of eq. 2.5 once the overall reaction considered to be 2/3.

Summary of the oxidation and reduction reactions kinetic parameters is presented in Table 2.2. Significant effects of the support oxides on the oxidation and reduction activation energies were witnessed. For the Cu-based oxygen carriers, the activation energy of the oxidation reaction increased with the addition of support oxides increasing the energy; however, the addition of support oxides decreased the reduction reaction activation energy.

Table 2.2 Oxidation and reduction reactions kinetic parameters of metal-based oxygen carriers

	Oxidation			Reduction		
Sample	**k_0($mol^{1-n}g^{n-2}$/min)**	**E_o(kJ/mol)**	**n**	**k_0($mol^{1-n}g^{n-2}$/min)**	**E_r(kJ/mol)**	**n**
Cu	412.98	50.03	1.01	14.28	149.29	1.12
Co	4.25	35.66	1.01	7.57	85.82	1.22
Fe	9.96	113.64	2.13	11.06	119.86	1.43
Ni	5.16	41.74	1.03	1.20	26.84	1.07
Cu/Al_2O_3	148.45×10^3	113.34	0.98	1.05	8.00	0.92
Cu/CeO_2	20.06×10^6	158.49	2.64	61.92	46.37	1.09
Cu/TiO_2	129.50×10^4	130.94	0.67	106.14	51.12	0.01
Cu/ZrO_2	136.27×10^4	123.90	0.73	13.78×10^2	72.68	0.87
Co/Al_2O_3	3.458	11.78	1.06	1.47	17.12	0.33
Co/CeO_2	478.50×10^4	154.80	1.18	13.72	34.01	1.34
Co/TiO_2	147.44	43.68	0.34	37.79	50.49	1.05
Co/ZrO_2	8.42	23.35	1.26	17.45×10^2	83.80	0.67
Fe/Al_2O_3	429.87×10^6	184.01	1.11	7.56	2.80	0.002
Fe/CeO_2	34.23	43.13	1.72	21.73	42.81	0.20
Fe/TiO_2	799.90×10^6	194.18	0.94	31.14×10^2	9.51	0.06
Fe/ZrO_2	226.65	46.62	1.08	21.49×10^2	89.41	0.20
Ni/Al_2O_3	57.41×10^3	114.64	0.70	107.15	53.89	0.05
Ni/CeO_2	1.38	6.13	1.07	18.83	32.74	0.87
Ni/TiO_2	26.41	28.58	0.26	382.87	67.72	0.59
Ni/ZrO_2	1.11	1.69	1.50	409.48	63.68	0.88

For the Co-based samples, the addition of Al_2O_3 and ZrO_2 decreased the activation energy of the oxidation reaction by 66.97% and 34.52%, respectively, while the addition of CeO_2 and TiO_2 increased the activation energy from 35.7 kJ/mol for pure Co to 154.8 kJ/mol and 43.7

kJ/mol, respectively. The reduction reaction activation energy, however, decreased with the addition of the supports.

The addition of Al_2O_3 and TiO_2 increased the oxidation reaction activation energy for the Fe samples by 61.93% and 70.88%, respectively, while the addition of CeO_2 and ZrO_2 decreased the activation energy by 62.04% and 58.97%, respectively. The reduction reaction activation energy of Fe decreased with the addition of the support oxides.

The oxidation reaction activation energy of the Ni supported sample with Al_2O_3 increased to 114.6 kJ/mol (from 41.7 kJ/mol for Ni). However, with the addition of CeO_2, TiO_2, and ZrO_2, the activation energy decreased up to 6.1 kJ/mol, 28.6 kJ/mol, and 1.7 kJ/mol, respectively. The activation energy for the reduction reaction of the Ni supported samples increased. There were mainly two factors that caused changes in the activation energies of supported metals: 1) metals/supports synergistic effect, 2) interaction between metals and supports. The energy needed to reduce metals at the time of synthesis (synergy) could be lowered on supported copper, cobalt and iron samples; thus, the energy barrier (activation energy) that was needed to move forward the reduction reaction decreased (Table 2.2). The opposite could also be occurred (i.e. increase of synergy resulted in higher activation energy of oxidation reaction). The interaction between Ni and supports oxides could occur and resulted in forming intermediate phase such as $NiAl_2O_4$ and NiCe; therefore, the reduction reaction activation energy to reduce the supported nickel increased, as those phases usually formed endothermically. In this study, it was found that less synergistic effect and the absence of forming intermediate phases led to high reactive oxygen carriers that had oxygen capacity closer to its theoretical value and lower activation energies. The synthesized oxygen carriers Cu/Al_2O_3, Co/CeO_2, Fe/ZrO_2, and Ni/ZrO_2 showed high reactivity among others samples.

2.6. Conclusion

Methane CLC using metal-based oxygen carriers was investigated using a bench-scale reactor, and a TGA. The metals Cu, Co, Fe, and Ni were successfully synthesized, characterized, and examined for their potential to be used in the CLC process. The results indicated that the surface area of Co, Fe, and Ni slightly decreased after the reduction reaction with H_2 in the bench-scale reactor; however, the surface area of Cu slightly increased. Interaction phases ($CoAl_2O_4$ and $NiAl_2O_4$) were observed by the XRD analysis, where the $CoAl_2O_4$ phase completely reduced to Co and Al_2O_3 but $NiAl_2O_4$ sample did not reduced. The effect of sample initial weight in the TGA showed no significant effect on the oxidation/reduction reactions of Cu, Co, Fe, and Ni. Further, as the CH_4 concentration increased, the reduction of the metal oxygen carriers and the deposition of carbon on the metal oxygen carriers increased. The Co, Fe, and Ni based samples showed the highest oxygen capacities at 950°C, while the Cu-based oxygen carriers reported the highest oxygen capacity at 900°C. Increasing the oxidation reaction temperature lowered the reaction rate but increased the reduction reaction rate of all samples. The addition of support oxides lowered the activation energies of oxidation and reduction reactions for most of the metals. The Cu/Al_2O_3, Co/CeO_2, Fe/ZrO_2, and Ni/ZrO_2 samples showed better performance in term of H_2 gas reducibility, oxygen capacity, and the oxidation and reduction reactions activation energies, suggesting their potential to be further tested in a lab-scale reactor.

2.7. Acknowledgements

The authors would like to acknowledge the financial support provided by Canadian Natural Resources Limited (CNRL), Devon, and the Natural Sciences and Engineering Research Council of Canada (NSERC). The authors would also like to acknowledge the financial support received

from the Ministry of Education (MOE) in the Kingdom of Saudi Arabia, and we appreciate the volunteering TGA and synthesis help of this study performed by Camilla Fernandes De Oliveira, Diego Costa, Tommy Chu, Ningyu Yu, Ahmed El-Mehairi, and Steve Lee. The authors would like to acknowledge Dr. Gerardo Vitale Rojas for the helpful discussions about the XRD data analysis and interpretation.

2.8. References

[1] Hossain, M. M., de Lasa H. I., Chemical-looping combustion (CLC) for inherent CO_2 separations - a review. Chem. Eng. Sci. 2008; 63: 4433-4451.

[2] Adánez, J., Abad, A., García-Labiano, F., de Diego, L, F., Gayán, P., Progress in Chemical-Looping Combustion and Reforming Technologies. A review. Prog. Energy Combust. Sci. 2012; 38: 215-282.

[3] Frick, V., Rydén, M., Leion, H., 2016. Investigation of Cu–Fe and Mn–Ni oxides as oxygen carriers for chemical-looping combustion. Fuel Process. Technol. 2016; 150: 30-40.

[4] Guo, Q., Yang, M., Liu, Y., Yang, Q., Zhang, Y., 2016. Multicycle Investigation of a Sol-Gel-Derived Fe_2O_3/ATP Oxygen Carrier for Coal Chemical Looping Combustion. AIChE J. 2016; 62: 996-1006.

[5] Mohamed, S. A., Quddus, M. R., Razzak, S. A., Hossain, M. M., de Lasa, H. I., Fluidizable NiO/Ce-γAl_2O_3 Oxygen Carrier for Chemical Looping Combustion. Energy Fuels. 2015; 29: 6095−6103.

[6] Abad, A., Adánez, J., García-Labiano, F., de Diego, L. F., Gayán, P., Modeling of the chemical-looping combustion of methane using a Cu-based oxygen-carrier. Combust. Flame. 2010; 157: 602–615.

[7] Bakare, I. A., Mohamed, S. A., Al-Ghamdi, S., Razzak, S. A., Hossain, M. M., de Lasa, H. I., Fluidized bed ODH of ethane to ethylene over VOx–MoOx/c-Al_2O_3 catalyst: Desorption kinetics and catalytic activity. Chem. Eng. J. 2015; 278: 207–216.

[8] Hossain, M. M., de Lasa, H. I., Reduction and oxidation kinetics of Co–Ni/Al_2O_3 oxygen carrier involved in a chemical-looping combustion cycles. Chem. Eng. Sci. 2010; 65: 98-106.

[9] Xu, Z., Zhao, H., Wei, Y., Zheng, C., Self-assembly template combustion synthesis of a core–shell CuO@TiO_2–Al_2O_3 hierarchical structure as an oxygen carrier for the chemical-looping processes. Combust. Flame. 2015; 162: 3030-3045.

[10] Donat, F., Hu, W., Scott, S. A., Dennis, J. S., Characteristics of Copper-based Oxygen Carriers Supported on Calcium Aluminates for Chemical-Looping Combustion with Oxygen Uncoupling (CLOU). Ind. Eng. Chem. Res. 2015; 54: 6713−6723.

[11] Ksepko, E., Examining $SrCuO_2$ as an oxygen carrier for chemical looping combustion. J. Therm. Anal. Calorim. 2015; 122: 621–633.

[12] Wang, X., Liu, H., Jin, B., Zhao, J. Sun, C., Snape, C. E., Experimental Evaluation of a Chinese Sulfur-Containing Lean Iron Ore as the Oxygen Carrier for Chemical-Looping Combustion. Ind. Eng. Chem. Res. 2015; 55: 428-435.

[13] Monazam, E. R., Breault, R. W., Tian, H., Siriwardane, R., Reaction Kinetics of Mixed CuO−Fe_2O_3 with Methane as Oxygen Carriers for Chemical Looping Combustion. Ind. Eng. Chem. Res. 2015; 54: 11966-11974.

[14] Mei, D. Mendiara, T., Abad, A., de Diego, L. F., García-Labiano, F., Gayań, P., Adańez, J., Zhao, H., Evaluation of Manganese Minerals for Chemical Looping Combustion. Energy Fuels. 2015; 29: 6605-6615.

[15] Dennis, J. S., Scott, S. A., In situ gasification of a lignite coal and CO_2 separation using chemical looping with a Cu-based oxygen carrier. Fuel. 2010; 89: 1623-1640.

[16] Zhao, H., Guo, L., Zou, X., Chemical-looping auto-thermal reforming of biomass using Cu-based oxygen carrier. Appl. Energy. 2015; 157: 408-415.

[17] Wang, K., Yu, Q., Qin, Q., Duan, W., Feasibility of a Co Oxygen Carrier for Chemical Looping Air Separation: Thermodynamics and Kinetics. Chem. Eng. Technol. 2014; 37:

1500-1506.

[18] San Pio, M. A., Roghair, I., Gallucci, F., Van Sint Annaland M., Investigation on the decrease in the reduction rate of oxygen carriers for chemical looping combustion. Powder Technol. 2016; 301: 429-439.

[19] Cho, P., Mattisson, T., Lyngfelt, A., Carbon Formation on Nickel and Iron Oxide-Containing Oxygen Carriers for Chemical-Looping Combustion. Ind. Eng. Chem. Res. 2005; 44: 668-676.

[20] Chiron, F-X., Patience, G.S., Rifflart, S., Kinetic mechanism derived through dosing reactants over NiO, Ni and Ni-C. In: Proc. 1st International Conference on Chemical Looping. Lyon, France. 2010.

[21] Dewaele, O., Froment, G. F., TAP Study of the Mechanism and Kinetics of the Adsorption and Combustion of Methane on Ni/Al_2O_3 and NiO/Al_2O_3. J. Catal. 1999; 184: 499-513.

[22] Ryu, H-J, Bae, D-H, Jin, G-T., Effect of Temperature on Reduction Reactivity of Oxygen Carrier Particles in a Fixed Bed Chemical-Looping Combustor. Korean J. Chem. Eng. 2003; 20: 960-966.

[23] Ishida, M., Jin, H., Okamoto, T., Kinetic Behavior of Solid Particle in Chemical-Looping Combustion: Suppressing Carbon Deposition in Reduction. Energy Fuels. 1998; 12: 223-229.

[24] Gomez, A., Mahinpey, N., A new method to calculate kinetic parameters independent of the kinetic model: Insights on CO_2 and steam gasification. Chem. Eng. Res. Des. 2014; 95: 346-357.

CHAPTER THREE: Determination of redox pathways of supported bimetallic oxygen carriers in a methane fuelled chemical looping combustion system

Fuel 233 (2018) 133-145

3.1. Presentation of the article

This chapter presents an article that determines the governing redox reaction pathways for the methane fuelled CLC process when bimetallic oxygen carriers were used based on the experimental findings and optimum operating conditions of monometallic carriers described in Chapter 2. The intrinsic and global kinetics of bimetallic samples were estimated, which then helped in addressing the internal mass transfer phenomenon that impacted most samples during the oxidation reaction. While determining the governing pathways, it was observed that precursors with weak chemical stability most likely reduced with methane then interacted with support to form metal-support complexes. Moreover, once the chemical stability between precursors and support remained resilient, negligible interaction between precursors and supports was observed. In addition, three samples stood out (Ni-Co/ZrO_2, Ni-Cu/ZrO_2, and Ni-Fe/ZrO_2) in terms of stable oxygen capacities as the temperature increased and negligible interaction between precursors and supports.

The experimental design, testing, calculations, data interpretation, writing and editing of this work were performed by Tijani, M. M. Guidance about the TPR-H_2 and BET analyses were offered by Dr. Aqsha, A. Part of the TGA experiment and data extraction was performed by Mr. Yu, N. Prof. Mahinpey, N. provided supervision to carry out this work, revision and refining the final manuscript.

Determination of redox pathways of supported bimetallic oxygen carriers in a methane fuelled chemical looping combustion system

This article has been published in Fuel Journal 233 (2018) 133-145. Reprinted with permission.

Mansour Mohammedramadan Tijani[a], Aqsha Aqsha[b], Ningyu Yu[a], Nader Mahinpey[a]

[a] Department of Chemical and Petroleum Engineering, Schulich School of Engineering, University of Calgary, Calgary, Alberta, T2N 1N4, Canada

[b] Department of Chemical Engineering, Faculty of Engineering, Universiti Teknologi PETRONAS, 32610 Seri Iskandar, Perak Darul Ridzuan, Malaysia

3.2. Abstract

The incipient wetness impregnation technique was used to synthesize supported bimetallic precursors (Ni and Co, Cu or Fe) by Al_2O_3, CeO_2, TiO_2 and ZrO_2 in order to understand both oxidation and reduction reactions (redox) pathways during the methane chemical looping combustion (CH_4-CLC). Understanding the reaction pathways helps to enable proper modifications of oxygen carriers, which later assists in choosing chemically stable precursors that could enhance the overall redox reaction rates. A higher solid conversion rate and fewer interactions with supports will produce highly reactive and thermally stable oxygen carriers. The BET surface area results showed highest increase in Ni-Fe/ZrO_2 sample by 17.73% and highest decrease in Ni-Fe/CeO_2 sample by 78.80%. The internal mass transfer results revealed that the reaction and internal diffusion for Ni-Fe/TiO_2 and Ni-Fe/ZrO_2 samples were similar; however, the effectiveness factor of the Ni-Cu/TiO_2 sample showed isothermal surface reaction was the controlling step. Under the operating condition presented in this study (oxidation with air at 20 ml/min, and reduction with CH_4 balanced with N_2 at 20 ml/min), most stable samples for CLC practical deployment were Ni-Co/ZrO_2, Ni-Cu/ZrO_2, and Ni-Fe/ZrO_2 due to their exhibition of

stable oxygen transport capabilities, and nonexistence of interaction between precursors and supports.

3.3. Introduction

Global warming, nowadays, is caused by the large-scale emission of greenhouse gases. A large portion of emissions results from industrially emitted carbon dioxide [1]. Carbon capture and sequestration processes are among the most promising strategies to decrease the atmospheric concentration of carbon dioxide. The oxy-fuel combustion process means that the fuels (gas or solid) are combusted with only oxygen. This process is considered clean where a mixture of CO_2 and H_2O is produced and easily separated while the formation of nitrogen oxides (NOx) is avoided [2]. The Chemical Looping Combustion (CLC) process has great potential to become an efficient and clean alternative technology [2]. CLC was introduced as a means of reducing the CO_2 emission [3]. It was chosen among others because of its potential to reduce the cost of the CO_2 capture process by up to 50% [4]. In the CLC process, a solid oxygen carrier is oxidized at high temperatures inside a reactor called the air reactor. The reactants are air and the solid oxygen carrier, which is transferred to the fuel reactor. In the case of fixed-bed reactors, the carrier is exposed to the fuel. Conversion of fuel and reduction of the oxygen carrier is then carried out. The process is then repeated in multiple cycles (i.e. oxidation/reduction reactions). The following reactions describe the general CLC process.

$$(OC)_r + Air \rightarrow (OC)_o \; ; \quad \Delta H_o \tag{3.1}$$

$$(OC)_o + Fuel \rightarrow CO_2 + H_2O + (OC)_r \; ; \quad \Delta H_r \tag{3.2}$$

where OC is Oxygen Carrier; ΔH_o is enthalpy of oxidation reaction (J); ΔH_r represents enthalpy of reduction reaction (J); and r & o subscripts represent reduced and oxidized, respectively.

CLC of gaseous fuel (i.e. CH_4) is used to separate CO_2 from N_2 when gaseous fuel is combusted. The oxygen reacts with the gaseous fuel to produce end-products like CO_2 and H_2O. After the condensation of H_2O, a highly concentrated stream of CO_2 can be obtained. This process reduces the penalties (heat loss and CO_2 capture/separation unit) that are usually associated with the capture of CO_2 from flue gases resulted from the combustion of gaseous fuel in an air environment [5]. Although not all transition metals are suitable for oxygen carriers due to their reactivity, cost and/or environmental concerns, different attempts have been made to enhance the reactivity of some transition metals. Zheng *et al* [6] studied different combinations of Cu as an active site, as well as SiO_2 and Al_2O_3 supports for their capability to produce a high concentration stream of H_2 in a fixed-bed reactor (270 cm^3). It was then reported that a 95% conversion of H_2 was observed at 500°C. The carrier with 36.1% Cu loading was found to exhibit the highest oxygen capacity of 9%. Harper *et al* [7] studied copper-based oxygen carriers in a packed-bed reactor at 400°C. It was found that mixing different copper oxides and oxygen carriers in the fuel reactor at a ratio of 1:6 (Al_2O_3) could prevent the agglomeration between the active site (Cu) and inert support (Al_2O_3) in the solid particles. It was concluded that the concentration of copper at the particle surface was proportional to the presence of agglomeration. Zhu *et al* [8] investigated the use of Fe_2O_3/Al_2O_3 (3:2) in a newly proposed configuration of a CLC packed-bed reactor at 850°C. High concentrations of H_2 (95 vol.%) were achieved after 20 cycles of oxidation/reduction reactions. Hamers *et al* [9] examined the effect of pressure (2–7.5 bar at 600°C) on the performance of a $NiO/CaAl_2O_4$ oxygen carrier in a packed-bed reactor. It was concluded that changes in pressure have a small effect on the outlet molar fractions of O_2 and H_2, which were observed in both oxidation and reduction cycles (8.75% and 12.5%, respectively). Song *et al* [10] investigated the effect of temperature, gas flow rate, initial sample weight and particle size on a novel $CaSO_4$

oxygen carrier for methane combustion. It was found that a reaction temperature of 950°C showed the highest methane reduction rate with 0.4–0.6 mm average particle size of $CaSO_4$. The 90g initial weight of $CaSO_4$ showed a 28.6% higher conversion rate of CH_4 as well as a 21.4% higher conversion for CH_4 with a flow rate of 50 ml/min.

Unsupported mixed metal oxygen carriers such as Fe-Cu and Mn-Ni were tested in a batch fluidized-bed reactor by Frick *et al* [11] using CH_4, H_2 and CO as fuel gases. Average CO_2 yield from methane was reported to be higher than 85% at 1050°C for all samples. The activation energies for oxidation and reduction reactions are another key parameter to determine the reactivity of oxygen carriers. Typical values for the activation energy of reduction reaction are found to be less than 100 kJ/mol, and for the oxidation reaction are higher than 100 kJ/mol; however, values of activation energies greater than 300 kJ/mol are considered to be high [2]. Hossain and Lasa [12] evaluated the activation energy and reaction mechanisms for bimetallic oxygen carriers using O_2-TPO and H_2-TPR. It was found that both reactions were better presented by nucleation and nuclei growth model where the activation energies for oxidation and reduction reactions were found to be 44 kJ/mol and 45 kJ/mol respectively. Jiang *et al* [13] tested a bimetallic oxygen carrier (Fe-Cu) for its reactivity in both TGA and batch fluidized-bed reactor using H_2 and CO as fuel gases. It was observed that as the Cu content increased (5% to 20%), the redox reactions rates (using H_2) also increased, as well as the agglomeration of Cu particles in the batch fluidized-bed reactor. Interpretation of possible reduction reaction mechanisms of bimetallic oxides oxygen carrier ($CuO\text{-}Fe_2O_3$) was reported by Siriwardane *et al* [14] who observed that methane fully reduced both bimetallic oxide precursors ($CuO\text{-}Fe_2O_3/Al_2O_3$) to Cu and Fe metals due to the synergetic effect of released oxygen, and dispersion of CuO and Fe_2O_3 on $CuFe_2O_4$. Bhavsar *et al* [15] investigated the phase stability of bimetallic oxygen carriers ($Fe\text{-}Mn/CeO_2$) in both TGA and

fixed-bed reactors and reported that a high ratio of ceria-supported Fe to Mn oxygen carrier resulted in de-alloying and re-alloying phenomena that unfavorably enhanced the solid-state diffusion process in the Fe phase.

Kinetic measurements and evaluation for metal-based oxygen carriers have been reported in the literature. However, the literature contains few detailed explanations of the experimental reduction reaction pathways of supported bimetallic (Co, Cu, Ni, Fe) oxygen carriers. Therefore, studies of the intrinsic and global kinetics for methane-fuelled CLC redox reactions of supported bimetallic oxygen carriers are required to have an understanding of reaction mechanism. This paper provides a bridge to link innovative future approaches to efficient performance of bimetallic oxygen carriers and previous studies that showed that the use of some metals with substantially high oxygen carrying capacity were considered expensive and/or toxic to humans and the environment (i.e. Co, Cu, Ni) while others with low oxygen carrying capacity (i.e. Fe) were inexpensive. The aim of this paper is to provide comprehensive studies on the reactivity and kinetics of supported bimetallic oxygen carriers (Ni-Co, Ni-Cu, Ni-Fe), and to interpret the most dominant reduction reaction pathways when methane is used as a fuel. The outcomes of this study will provide valuable information about chemically stable and supported bimetallic oxygen carriers in the methane-fuelled CLC system, which could help in improving precursor conversion level, increasing CO_2 selectivity among other gases such as H_2 and CO, and reducing the precursors-supports interactions.

3.4. Materials and Methods

3.4.1. Materials

The synthesized oxygen carriers used in this study are as follows: Ni-Co/Al_2O_3, Ni-Co/CeO_2, Ni-Co/TiO_2, Ni-Co/ZrO_2, Ni-Cu/Al_2O_3, Ni-Cu/CeO_2, Ni-Cu/TiO_2, Ni-Cu/ZrO_2, Ni-Fe/Al_2O_3, Ni-

Fe/CeO_2, $Ni\text{-}Fe/TiO_2$, $Ni\text{-}Fe/ZrO_2$. They were prepared using the incipient wetness impregnation method. The following nitrates forms of precursor were purchased from Sigma Aldrich Canada: cobalt nitrate hexahydrate ($Co(NO_3)_2.6H_2O$), copper nitrate trihydrate ($Cu(NO_3)_2.3H_2O$), iron nitrate nonahydrate ($Fe(NO_3)_3.9H_2O$), and nickel nitrate hexahydrate ($Ni(NO_3)_2.6H_2O$). The support oxide CeO_2 (99.995%) was purchased from Sigma Aldrich Canada, while Al_2O_3 (γ-alumina, 99.9%), TiO_2 (99.5%), and ZrO_2 (99.5%) were purchased from Alfa-Aesar. Both metal nitrates and support oxides were used without any further modifications. A beaker was initially filled with 50 ml of DI water, and then a starting aqueous solution was used where the respective nitrates form of precursor #1 (i.e. Ni) was dissolved for 10 min followed by nitrates form of precursor #2 (i.e. Co, Cu, Fe). The support oxides (Al_2O_3, CeO_2, TiO_2, ZrO_2) were then added to the mixture and stirred for 24 h. The mixture was then heated to 75°C until all water evaporated. The sample was then collected, and dried in a conventional oven at 120°C for 12 h to remove all moisture. The sample was then calcined in air at 800°C for 3 h to remove any impurities (e.g. NOx), and to form the oxide forms of the binary precursors. Finally, the oxidized samples were reduced in a tubular reactor in hydrogen gas (Praxair Canada, ultra-high: 99.95 vol%) at 800°C for 3 h to obtain the oxygen-free forms of oxygen carriers.

3.4.2. Characterization Studies

The synthesized oxygen carriers were characterized using Brunauer–Emmett–Teller (BET) surface area/porosimetry technique, and Hydrogen-Temperature Programmed Reduction (H_2-TPR). The surface area and pore volume of oxygen carriers were obtained using the Micromeritics ASAP 2020 instrument. The sample was first de-gassed (evacuated to 20 mmHg, and heated to 120°C for 2 h) to remove all surface moisture. The analysis was then conducted on the gas-free and moisture-free sample using nitrogen gas as an absorptive gas at -196°C (liquid nitrogen bath).

The BET isotherm of the sample was obtained where the Brunauer–Emmett–Teller (BET) theory was applied to calculate the surface area of the sample. The mesoporous dimensions were then estimated.

The H_2-TPR experiments were performed using Quantachrome ChemBET 3000 chemisorption analyzer. About 100 mg of the sample was placed in a quartz tube and was heated up to 200°C for 1 h under an Argon (Ar) flow of 50 ml/min. After this pretreatment, the sample was then reduced using a 10% H_2/Ar (Praxair Canada, ultra-high, Ar: 99.995 vol%, H_2: 99.95 vol%) gas mixture passing through the sample at a flow rate of 15 ml/min. The sample was heated up to 900°C. The H_2 consumption during the reduction of the metal with an increase in temperature was observed by seeing changes in the TCD signal. The area under the reduction peak gave the amount of H_2 consumed during the reduction process.

3.4.3. Experimental Setup

A thermogravimetric analyzer (TGA 209 F1 Libra) was used to study the reactivity of oxygen carriers. Oxygen capacity (detached oxygen) was measured by loading around 10 mg of sample into an aluminum oxide (Al_2O_3) crucible, and placing the crucible inside the TGA. The analysis started with keeping the sample at 25°C for 5 min to stabilize its weight, then the sample was heated to the reaction temperature (800°C-1000°C) at a 100K/min heating rate and a nitrogen gas flowrate of 20 ml/min (Praxair Canada, purity: 99.998 vol%). The sample was kept at the reaction temperature for 3 min to achieve isothermal condition, then air was introduced to the sample at 20ml/min for 10 min to allow the oxidation reaction, followed by another 10 min of methane gas (Praxair Canada, chemically-pure: 99.0 vol%) at 40 vol.% (balanced with nitrogen) to allow the reduction reaction. Nitrogen gas was purged for 3 min between each oxidation and reduction segment to avoid mixing of gases. The chemical looping combustion of methane using

solid oxygen carriers was carried out using same steps as for the determination of oxygen capacity, except that the oxidation and reduction reactions were repeated three and two times respectively in order to evaluate the rate of oxidation and reduction reactions on solid oxygen carriers. The optimized TGA operating conditions were adopted from [16]. Blank runs of crucible and supports oxides were carried out, and then subtracted from all data to avoid the inclusion of the gases' buoyancy effect, as well as redox reactions of crucible and support oxides.

3.5. Results and Discussion

3.5.1. Bimetallic oxygen carrier characterizations

3.5.1.1. *BET surface area and porosimetry*

The absolute BET surface area and the mesoporous pore volume values of all samples are shown in Table 3.1. The differences between oxidized and reduced bimetallic oxygen carriers are presented in Fig. 3.1.

Table 3.1 BET surface area and mesoporous pore volume

Sample	Surface area (m^2/g)		Pore volume (cm^3/g)	
	Oxidized	Reduced	Oxidized	Reduced
Ni-Co/Al_2O_3	47.185	36.706	0.139	0.112
Ni-Co/CeO_2	4.140	3.715	0.018	0.016
Ni-Co/TiO_2	2.951	3.113	0.008	0.014
Ni-Co/ZrO_2	6.828	4.141	0.036	0.017
Ni-Cu/Al_2O_3	28.096	21.477	0.118	0.086
Ni-Cu/CeO_2	4.028	3.797	0.016	0.011
Ni-Cu/TiO_2	2.112	2.140	0.005	0.005
N-Cu/ZrO_2	4.218	3.148	0.016	0.013
Ni-Fe/Al_2O_3	48.400	41.110	0.144	0.154
Ni-Fe/CeO_2	5.227	1.108	0.027	0.012
Ni-Fe/TiO_2	3.407	1.964	0.020	0.004
Ni-Fe/ZrO_2	4.745	5.586	0.062	0.023

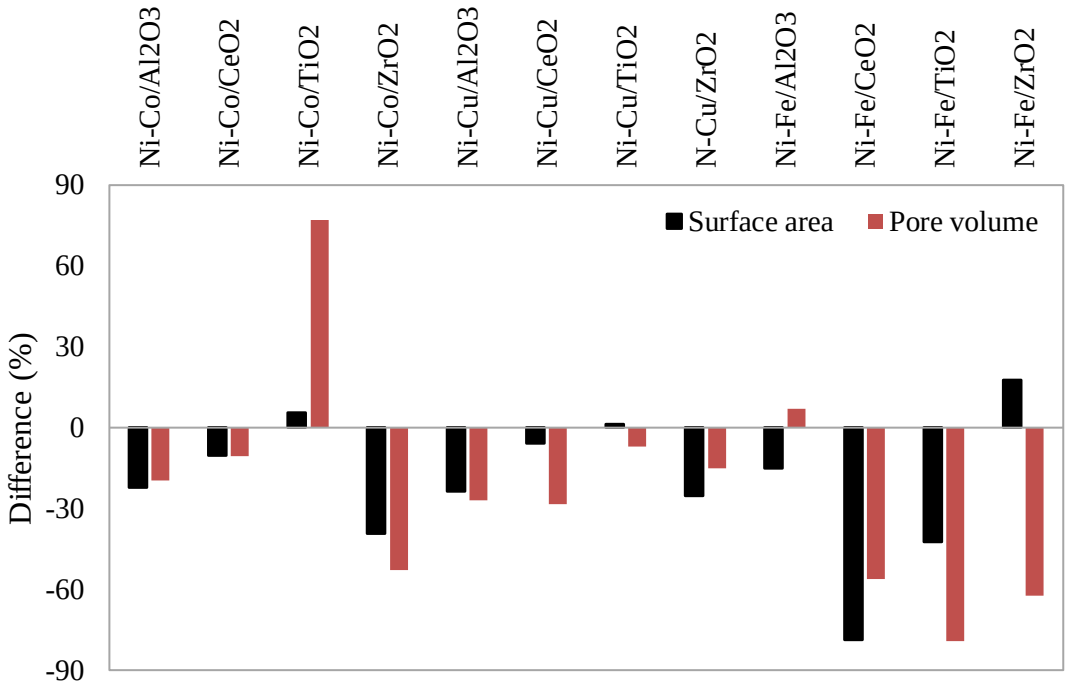

Fig. 3.1. BET surface area and pore volume percentage difference between oxidized and reduced samples.

All bimetallic oxygen carriers exhibited a decrease (negative values of Fig. 3.1) in the surface area (Fig. 3.1) after the reduction experiment with H_2 gas, except for Ni-Co/TiO_2, Ni-Cu/TiO_2, and Ni-Fe/ZrO_2 samples, where the surface area slightly increased (positive values of Fig. 3.1) by 5.48%, 1.32% and 17.73% respectively. The greatest percentage surface area reductions were found in Ni-Fe/CeO_2 (78.80%), Ni-Fe/TiO_2 (42.33%), and Ni-Co/ZrO_2 (39.46%) samples. The mesoporous pore volumes of oxidized and reduced bimetallic oxygen carriers are shown in Fig. 3.1. All samples reported a pore volume of less than 0.1600 cm^3/g, and a similar trend of oxidized and reduced bimetallic surface areas was observed for all pore volumes except for Ni-Fe/Al_2O_3 and Ni-Fe/ZrO_2 samples. The pore volume of the Ni-Fe/Al_2O_3 sample increased from 0.144 cm^3/g to 0.1541 cm^3/g, while the pore volume of Ni-Fe/ZrO_2 decreased from 0.0619 cm^3/g to 0.0233 cm^3/g. The decrease in the surface area of bimetallic oxygen carriers could be due to the sintering

of particles after the reduction experiment, while the increase in the surface area and pore volume after the reduction treatment of Ni-Co/TiO_2 sample indicates that this sample did not suffer the sintering phenomenon after vacancies were created from the removal of oxygen atoms (H_2-reduction). The Ni-Fe/Al_2O_3 surface area decreased after the reduction treatment but its pore volume increased. This could be due to a partial sintering of particles inside pores, which resulted in decreasing the particle surface area and enlarging the pore size (i.e. diameter). Similar results of sintering of bimetallic (Ni-Co, Ni-Cu, Ni-Fe) systems versus pore volumes were discussed in detail in [17]. The variations in the BET surface area (increases/decreases) for several supported metals oxygen carriers were also reported elsewhere [16], [18]. The average uncertainty in the surface area measurements of Micromeritics ASAP 2020 instrument was calculated and found to be 0.82%.

3.5.1.2. *The Hydrogen Temperature Programmed Reduction (H_2-TPR)*

The H_2 uptake for each of the synthesized samples is shown in Fig. 3.2. The H_2 uptake provides a measure of the reactivity of precursors (bimetallic oxides) in terms of oxygen dissolution rate versus temperature increases. It was observed that the samples with low H_2 uptake may result in higher oxygen capacity, while samples with high H_2 uptake showed oxygen capacity closer to the theoretical values. This indicates that lower H_2 uptake resulted in great interaction between bimetallic precursor oxides and supports, which facilitated the reduction of support and thus higher oxygen capacity compared to the theoretical values. On the other hand, High H_2 uptake for some samples, such as Ni-Co/Al_2O_3, Ni-Cu/ZrO_2, Ni-Fe/TiO_2 and Ni-Fe/ZrO_2, resulted in oxygen capacity values that were closer to the theoretical ones, meaning that no significant interaction between the bimetallic precursor oxides and supports was encountered.

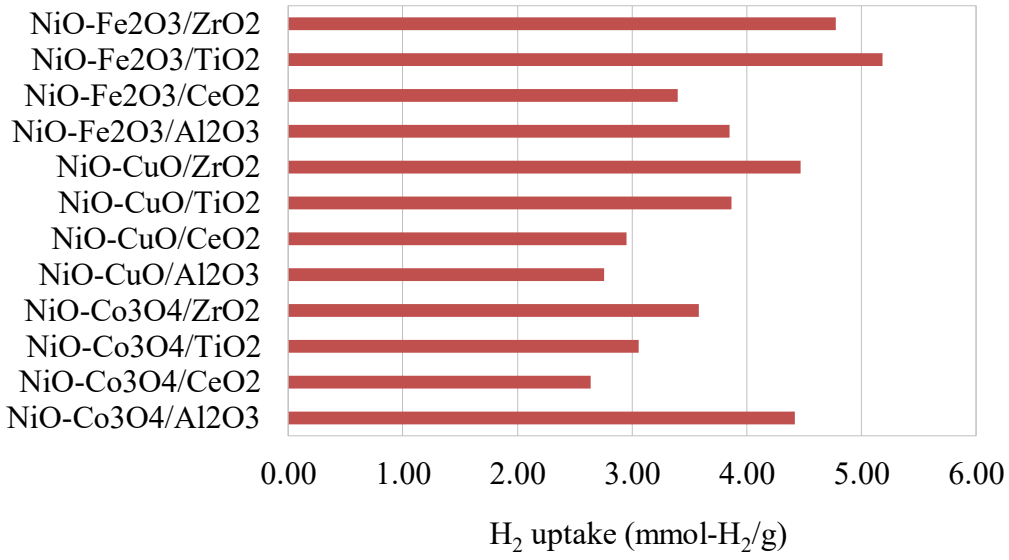

Fig. 3.2. Hydrogen uptake for bimetallic oxygen carriers.

Reduction profiles of oxidized supported bimetallic samples are shown in Fig. 3.3. The H_2-TPR analysis showed no significant reduction of support oxides except for CeO_2 support in which the average temperature of 812.3°C showed slight reduction. The use of CeO_2 as support has been generally reported in literature [2], [19]; however, the use of CeO_2 as an active site has particularly reported in literature such as the conversion of carbon monoxide and carbon dioxide [20]. This indicates the capability of CeO_2 to be reduced and oxidized compared to other supports presented in this study. On this basis, reduction of CeO_2 in the H_2-TPR analysis was likely to happen because of the elevated reduction temperature (900°C) and the presence of a strong reducing agent (H_2 gas). Therefore, the pure CeO_2 support alone showed a reduction temperature of 812.3°C (Fig. 3.3) among other supports. However, the existence of highly reactive mixed metal oxides such as NiO, Co_3O_4, CuO, and Fe_2O_3 as precursors facilitated an early reduction of CeO_2 to either Ce_2O_3, Ce, or complex metal-Ce phases. For that reason, no peak for CeO_2 was noticed at the knowingly

reduction temperature (812.3°C) of this study for pure CeO_2 sample. Further discussions about possible formation of metal-Ce complexes are explained in the effect of temperature on oxygen capacity section (Section 3.2.1).

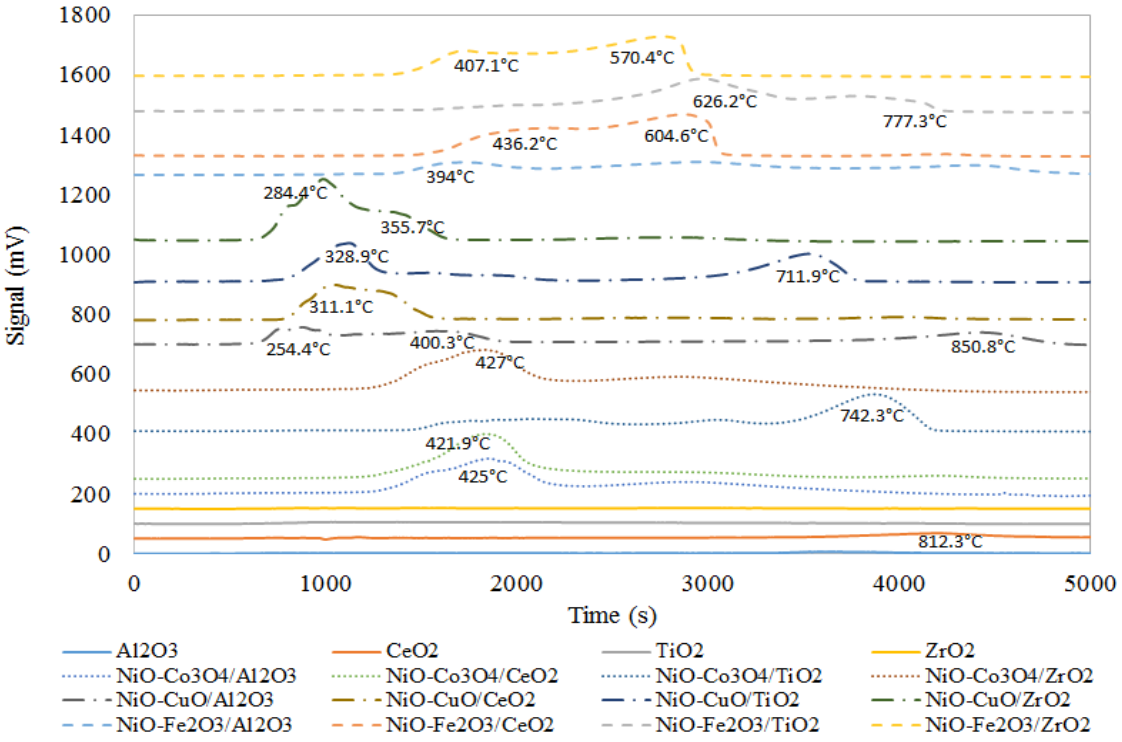

Fig. 3.3. H_2-TPR profile for bimetallic oxide oxygen carriers with reduction temperatures indicated under each peak.

The supported bimetallic oxide sample NiO-Co_3O_4 showed only one major reduction temperature for each sample, indicating that both NiO and Co_3O_4 simultaneously reduced to Ni and Co phases. The supported NiO-CuO bimetallic oxides showed two distinctive reduction temperatures, except for NiO-CuO/CeO_2, which showed only one reduction temperature (311.1°C). The reason for the two reduction temperatures could either be the separate reduction of bimetallic oxides or reduction of TiO_2 supports at higher temperature (700°C), which resulted from the interaction of bimetallic precursor oxides and supports. For the supported NiO-Fe_2O_3 samples, stretched reduction tread at two temperatures was observed with NiO-Fe_2O_3/CeO_2 and NiO-

Fe_2O_3/ZrO_2 samples, which could be due to the separate reduction of bimetallic oxide NiO-Fe_2O_3. Supported NiO-Fe_2O_3 with Al_2O_3 showed one reduction temperature of 394°C, but NiO-Fe_2O_3 supported with TiO_2 showed two reduction temperatures, where the temperature of 777.3°C could either be due to the separate reduction of bimetallic oxides or reduction of TiO_2 supports.

Reduction temperatures of metal oxides using hydrogen as a reducing agent have been reported as follows:

1) $Co_2O_3 \xrightarrow{333°C} CoO \xrightarrow{384°C} Co$ [21]

2) $CuO \xrightarrow{325°C} Cu$ [22]

3) $Fe_2O_3 \xrightarrow{390°C} Fe_3O_4 \xrightarrow{400°C-700°C} FeO \xrightarrow{400°C-700°C} Fe$ [23]

4) $NiO \xrightarrow{290°C} Ni$ [24]

In comparing Fig. 3.3 and the above-mentioned four steps, interaction between precursor oxides and supports occurred and resulted in three scenarios: a) the addition of NiO and the second precursor oxide (i.e. Co_3O_4, CuO or Fe_2O_3) on the supports by the incipient wetness impregnation technique increased the attraction energy between the bimetallic precursor oxides themselves or the active-site and support, and thus higher reduction temperatures compared to the reported ones were noticed; b) the addition of NiO and the second precursor oxide (i.e. Co_3O_4, CuO or Fe_2O_3) on the supports by the incipient wetness impregnation technique decreased the attraction energy between the bimetallic precursor oxides themselves or the active-site and support, and thus lower reduction temperatures were noticed; and, c) the addition of NiO and the second precursor oxide (i.e. Co_3O_4, CuO or Fe_2O_3) on the supports by the incipient wetness impregnation technique did not show any significant changes in the attraction energy of the bimetallic oxides, active-site and/or support.

Scenario (a) occurred with the NiO-Co_3O_4/Al_2O_3, NiO-Co_3O_4/CeO_2, and NiO-Co_3O_4/ZrO_2 samples. The NiO-Co_3O_4/TiO_2 sample showed no significant peak up until the temperature of 742.3°C, indicating that the supports might be reduced at this temperature, leading to a higher oxygen capacity than the theoretical value for this sample due to further reduction of supports. Reduction of NiO temperature was only noticeable with NiO-CuO/Al_2O_3 and NiO-CuO/ZrO_2 samples, consistent with scenario (b). Scenario (a) was observed for the CuO metal supported with Al_2O_3 and ZrO_2 supports. The NiO-CuO/CeO_2 sample showed the possibility that scenario (a) could occur on the NiO side and scenario (b) on the CuO side. The reduction of temperature of CuO (328.9°C) was close to the reported one (325°C), indicating that scenario (c) occurred on the CuO side. However, the same behaviour of TiO_2 support was observed with NiO-CuO precursors in which further reduction of TiO_2 occurred at 711.9°C.

Scenario (a) was the most dominant among NiO-Fe_2O_3 supported samples where no noticeable NiO reduction temperature was observed. With respect to temperature reduction of Fe_2O_3 metal, two trends were observed. Trend #1 was observed with NiO-Fe_2O_3/Al_2O_3 and NiO-Fe_2O_3/TiO_2 samples, where the complete oxidized iron (Fe_2O_3) reduced completely to either FeO or Fe with a low reduction temperature of 394°C in the NiO-Fe_2O_3/Al_2O_3 sample and a high reduction temperature of 626.2°C in the NiO-Fe_2O_3/TiO_2 sample compared to the standard reduction temperature of the oxidized iron (step 3). Trend #2 was observed with NiO-Fe_2O_3/CeO_2 and NiO-Fe_2O_3/ZrO_2 samples, where two distinctive reduction temperatures were noticed with a transition shoulder between them indicating a phase transition of Fe_2O_3 precursor. Therefore, Fe_2O_3 reduced to Fe_3O_4 and then to FeO at the low temperatures of 436.2°C and 407.1°C for the NiO-Fe_2O_3/CeO_2 and NiO-Fe_2O_3/ZrO_2 samples respectively. Then, the high reduction temperatures of 604.6°C and 570.4°C were responsible for the complete reduction to the Fe phase

for the $NiO\text{-}Fe_2O_3/CeO_2$ and $NiO\text{-}Fe_2O_3/ZrO_2$ samples, respectively. Scenario (c) could provide the best explanation for the reduction of $NiO\text{-}Fe_2O_3/CeO_2$ and $NiO\text{-}Fe_2O_3/ZrO_2$ samples. The reduction signal at 777.3°C for $NiO\text{-}Fe_2O_3/TiO_2$ sample could possibly again be due to the reduction of TiO_2 support.

3.5.2. Chemical Looping Combustion (CLC) using thermogravimetric analyzer (TGA)

The synthesized bimetallic oxygen carriers were examined in the TGA to evaluate their reactivity in the methane-fuelled CLC process. The typical TGA profile is shown in Fig. 3.4.

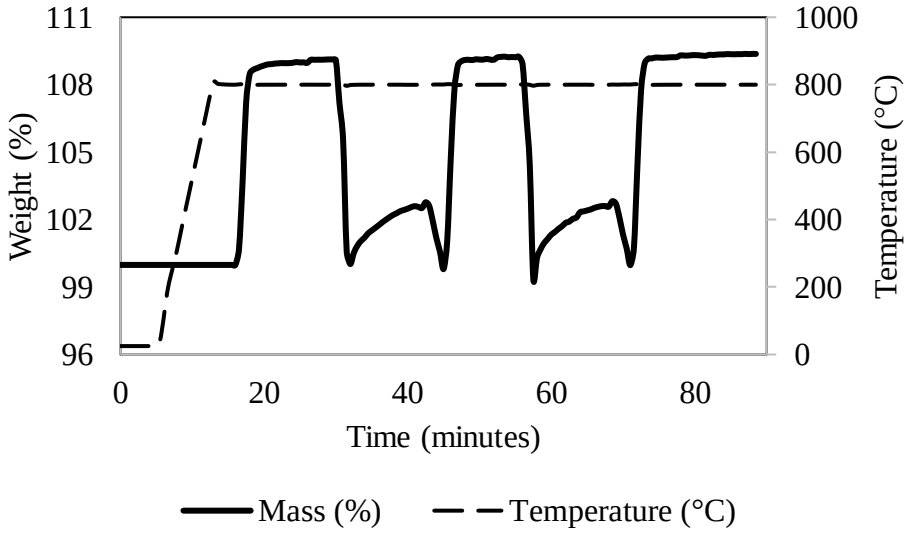

Fig. 3.4. Typical methane-fuelled CLC-TGA profile.

The first percentage weight gain is due to the oxidation reaction with air, while the first percentage weight loss corresponded to the methane reduction reaction. Carbon deposition formed immediately after the reduction reaction (second peak), followed by the combustion of carbon once air is introduced. Other oxidation and reduction cycles were followed to assess reactivity and carbon deposition. It was observed that air did not fully oxidize the sample, which resulted in less reduction conversion in the first cycle compared to the second cycle. Detailed studies on both

oxidation and reduction reaction rates are explained in section 5.4. The TGA experiments in this work were at least duplicated to find the uncertainty; however, a random sample was repeated six times. The uncertainty of TGA measurements was found to be 1.05 wt%.

3.5.2.1. *Effect of temperature on the oxygen capacity*

The detached oxygen capacities of bimetallic oxygen carriers were experimentally obtained for supported bimetallic samples. Then, the theoretical oxygen capacity for pure and unsupported active-metals was calculated and compared with the experimental values to investigate the effect of different reduction reaction temperatures on oxygen capacity. Knowing the oxygen capacity during the methane reduction reaction at different temperatures addresses whether or not there is an interaction between the active sites and supports (i.e. further reduction of supports in presence of metals), which may later provide useful information about the possible reduction reaction pathways of supported bimetallic oxygen carriers. The experimental oxygen capacity was estimated using the following expression:

$$OC_{Exp} = \frac{W_{Oxi} - W_{red}}{W_{Oxi}} \times 100\% \quad (3.3)$$

where: W_{Oxi} weight of fully oxidized sample (mg); and, W_{red} weight of fully reduced sample (mg). The theoretical oxygen capacity was calculated using the following expression [16]:

$$OC_{Theor} = \frac{k\, W_O}{W_{Oxi}} \times 100\% \quad (3.4)$$

where: W_O is the weight of detached oxygen (mg); W_{Oxi} is the weight of fully oxidized oxygen carrier (mg); and, k is the oxygen detachment factor (-).

The TGA experimental oxygen capacity (OC_{Exp}) at different reaction temperatures for supported bimetallic samples is shown in Figs. 3.5 to 3.7. The Ni-Co based oxygen carriers (Fig. 3.5) showed variations in the experimental oxygen capacity at different reaction temperatures. The

Ni-Co/Al_2O_3, Ni-Co/CeO_2, and Ni-Co/TiO_2 samples reported increases in the oxygen capacity as temperatures increased from 800°C to 1000°C; however, Ni-Co/ZrO_2 showed a stable oxygen capacity as temperature increased. The Ni-Co/Al_2O_3 sample reported an increase of 79.15% in the oxygen capacity (800°C to 1000°C), while Ni-Co/CeO_2, and Ni-Co/TiO_2 samples reported increases of 16.00% and 30.21% respectively when temperature increased from 800°C to 1000°C. The Ni-Co/ZrO_2 sample showed a maximum oxygen capacity of 9.89% at 900°C.

The variations in the oxygen capacities of these samples could be due either to the gas-solid interaction or interaction between precursors and supports such as Ni and Al_2O_3, which are widely reported to interact to form nickel aluminate spinel ($NiAl_2O_4$) that is nonreactive and requires high temperature to be fully reduced [25]. Comparison between the calculated maximum oxygen capacity (9.60%), where the loaded precursors on an inert support completely reduced (i.e. NiO-Co_3O_4 →Ni-Co), and TGA estimated oxygen capacity (Fig. 3.5) suggested that the Ni-Co/Al_2O_3 sample partially oxidized and formed the intermediate phase ($NiAl_2O_4$), lowering the oxygen capacity at 800°C-900°C reaction temperatures. However, as the temperature increased (950°C-1000°C), improved oxygen capacity was observed, which might be due to reduction at the intermediate phase (i.e. $NiAl_2O_4$) as temperature increased. Comparison between the calculated (9.60%) and TGA-obtained oxygen capacities of Ni-Co/CeO_2 and Ni-Co/TiO_2 samples indicated that interaction between precursors and supports occurred resulted in reducing the support oxides to possibly form Co-NiCe, Co-$NiCe_2O_3$ and/or Co-$NiTi_2O_3$ mixed-metal/oxide phases. Detailed thermodynamic studies to form NiCe, $NiCe_2O_3$ and $NiTi_2O_3$ mixed-metal/oxide phases have been discussed elsewhere [26], [27]. The coexistence of Ni precursor promoted the oxygen mobility in these oxides, which explains the higher TGA oxygen capacity values when compared to the calculated value of 9.60%. The Ni-Co/ZrO_2 sample showed stable oxygen capacity and lower than

the calculated value (9.60%), which means no possible interaction between precursor (i.e. Ni-Co) and support (i.e. ZrO_2) existed to hinder the oxygen capacity of this sample.

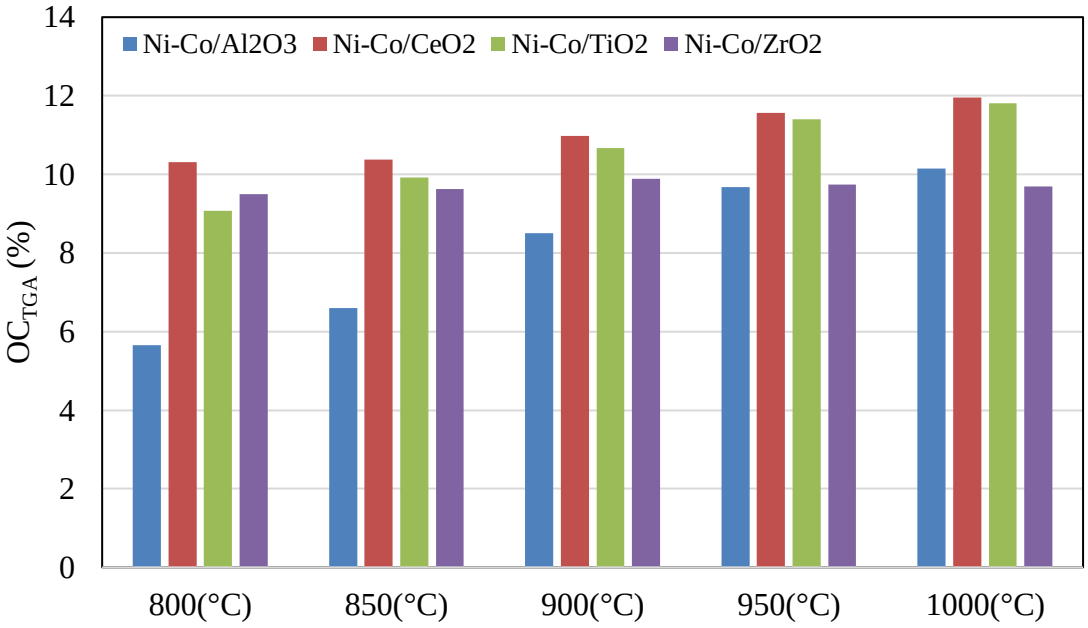

Fig. 3.5. TGA oxygen capacity (800°C-1000°C) for supported Ni-Co precursor with Al_2O_3, CeO_2, TiO_2 and ZrO_2 oxides.

The supported Ni-Cu precursor with Al_2O_3 (Fig. 3.6) showed an increase in the oxygen capacity as temperature increased from 800°C to 1000°C, where the maximum oxygen capacity was reported to be 8.81% at 1000°C. However, other supported Ni-Cu samples fluctuated and showed maximum oxygen capacities of 10.99% at 950°C for Ni-Cu/CeO_2, 9.97% at 1000°C for Ni-Cu/TiO_2 9.71% at 900°C for Ni-Cu/ZrO_2. A similar trend for Ni-Co/Al_2O_3 was observed in the Ni-Cu/Al_2O_3 sample (oxygen capacity increased with temperature increase due to $NiAl_2O_4$ formation/reduction). The $NiAl_2O_4$ formation could lower the TGA oxygen capacity between 800°C and 900°C, but as temperature increased from 900°C to 1000°C, TGA the oxygen capacity of the Ni-Cu/Al_2O_3 sample improved. Since further reduction of alpha alumina is not possible in this experimental condition, thermal decomposition of CH_4 to C and $2H_2$ at temperatures higher

than 900°C could facilitate the reduction of $NiAl_2O_4$, which in turn improved the TGA oxygen capacity of this sample.

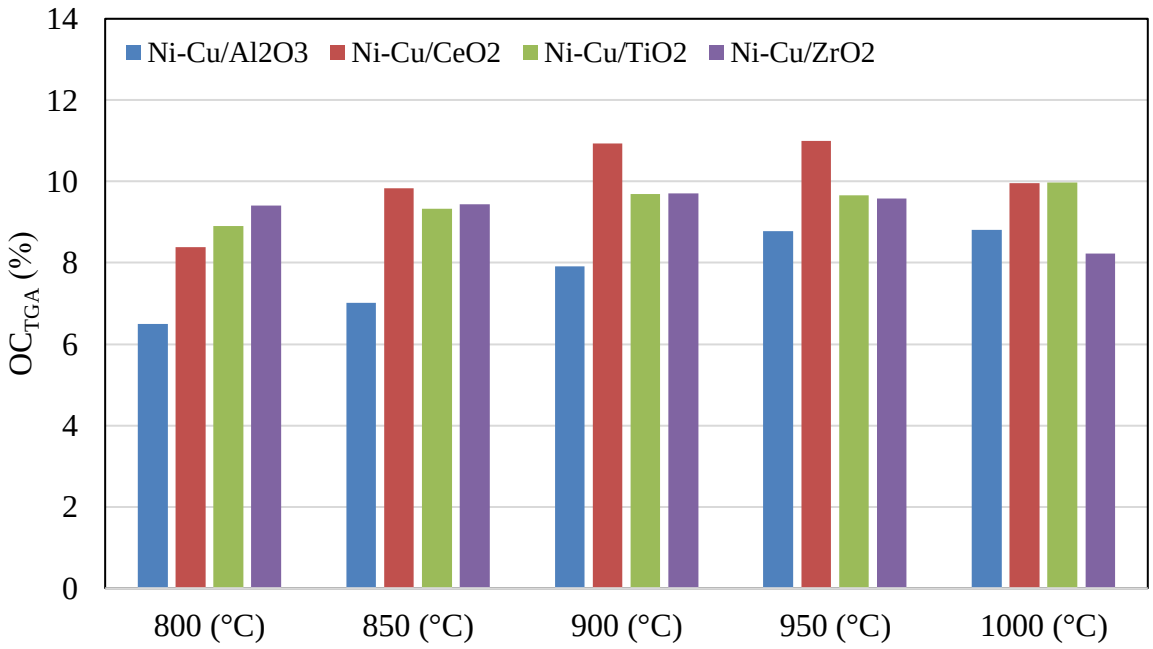

Fig. 3.6. TGA oxygen capacity (800°C-1000°C) for supported Ni-Cu precursor with Al_2O_3, CeO_2, TiO_2 and ZrO_2 oxides.

All Ni-Cu supported samples with Al_2O_3, CeO_2, TiO_2 and ZrO_2 oxides reported higher oxygen capacity than the calculated value (8.31%), except Ni-Cu/Al_2O_3 at 800°C, 850°C, 900°C, and Ni-Cu/ZrO_2 at 1000°C. The higher TGA oxygen capacity than the calculated value indicates further reduction of support oxides to form new phases of mixed-metals/oxides. Carbon formation is usually noticeable at TGA temperature higher than 850/900°C [28]. Thus, carbon formation occurred in the Ni-Cu/ZrO_2 sample when temperature increased from 900°C to 1000°C, which could prevent further reduction of NiO-CuO/ZrO_2 as temperature increased.

The supported bimetallic Ni-Fe oxygen carriers with CeO_2, TiO_2 and ZrO_2 as shown in Fig. 3.7 displayed a fluctuating trend as temperature increased from 800°C to 1000°C, but the oxygen capacity of Ni-Fe/Al_2O_3 sample increased as the temperature increased. The highest reported

oxygen capacities for Ni-Fe/Al_2O_3, Ni-FeCeO_2, Ni-Fe/TiO_2 and Ni-Fe/ZrO_2 samples were 11.55% at 1000°C, 14.73% at 950°C, 14.20% at 1000°C and 12.28% at 800°C, respectively. The calculated oxygen capacities of the oxide form of precursor Fe when it completely reduced to Fe were 10.30% and 11.41% when Fe_2O_3 → Fe and Fe_2O_3 → Fe_3O_4 → FeO → Fe, respectively. By comparing these values with the obtained TGA oxygen capacity for the non-reducible and most stable support within our experimental condition (i.e. ZrO_2), it was observed that the Fe_2O_3 precursor was reduced completely to Fe following the 11.41% oxygen capacity pathway. Therefore, no significant reduction of supports was observed in the Ni-Fe/Al_2O_3 and Ni-Fe/ZrO_2 samples at all reaction temperatures. However, reduction of supports in the presence of the Ni precursor was reported in Ni-Fe/CeO_2 and Ni-Fe/TiO_2 samples due to the higher oxygen capacity compared to the calculated values.

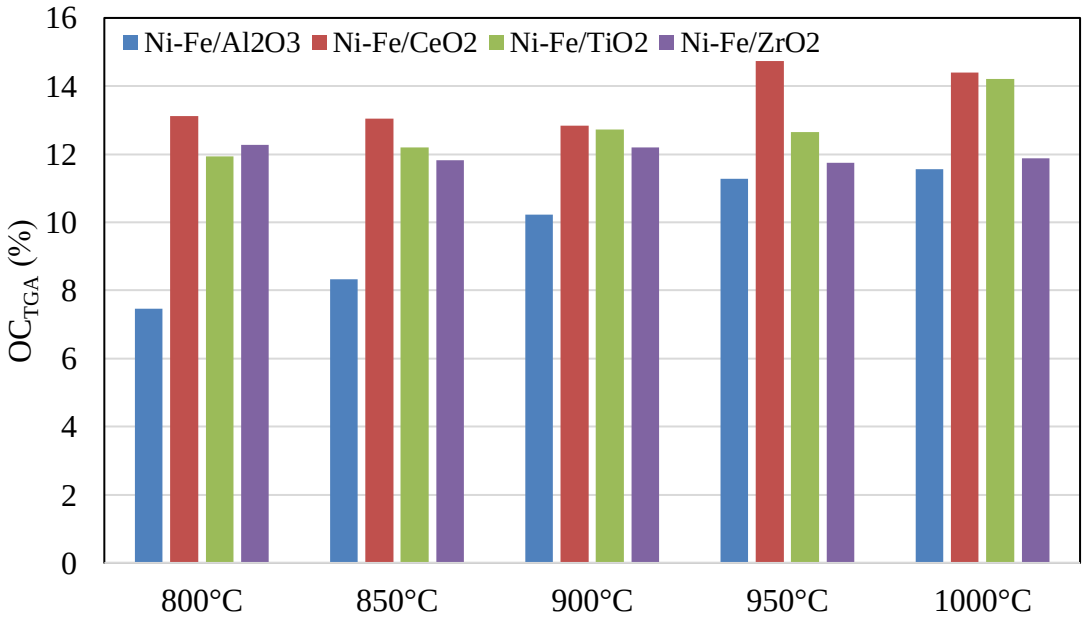

Fig. 3.7. TGA oxygen capacity (800°C-1000°C) for supported Ni-Fe precursor with Al_2O_3, CeO_2, TiO_2 and ZrO_2 oxides.

3.5.2.2. *Kinetics determination and the study of CLC redox reaction rates*

In this section, the activation energies for both oxidation and reduction reactions were estimated and presented to help verify the proposed pathways of transition phases during the methane-fuelled TGA-CLC process. The experimental conversion for both oxidation and reduction reactions was calculated using the following expression:

$$X = \frac{m - m_r}{m_o - m_r} \tag{3.5}$$

where: X is the solid conversion (-), m, m_r and m_o are the weight of sample at any time (mg), fully reduced sample weight (mg), and fully oxidized sample weight (mg), respectively.

A typical conversion profile for the oxidation and reduction reaction in a TGA is shown in Fig. 3.8. The shrinking core model (SCM) assumes that the consumed initial phase of sample shrinks to produce another different phase, named the product layer. The diffusion into the product layer increases as the particle shrinks, which then results in a lower solid conversion level compared to the initial conversion level when the reaction regime is more influential (Fig. 3.8a). Referring to the shrinking core model trend (not necessarily a 100% match), it was observed that all oxidation profiles of bimetallic samples showed two distinctive regimes: a reaction-limited regime and mass-transfer-limited regime (similar trend and not a match to the SCM). Furthermore, all the experimental data for oxidation reaction were compared to the SCM and a similar trend was found; therefore, the shrinking core model was adopted in the oxidation reaction kinetic evaluation for the oxidation of bimetallic samples (Fig. 3.8a). However, the reduction profiles were different from one sample to another and did not follow a specific trend; therefore, the method explained in [16] that addressed both kinetics and reactions mechanisms was chosen for the evaluation of

reduction reaction kinetics to interpret the reduction reaction pathways of bimetallic oxygen carriers.

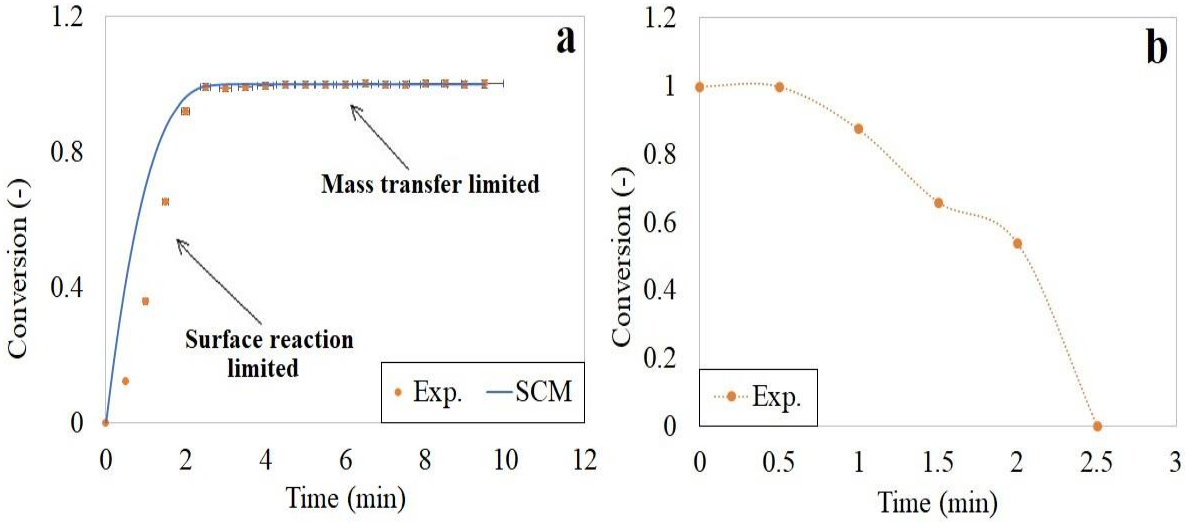

Fig. 3.8. Typical conversion profiles of bimetallic oxygen carriers, (a) oxidation conversion profile, (b) reduction conversion profile.

3.5.2.2.1. *Oxidation reaction*

The kinetics of oxidation reaction (intrinsic and global) was determined, then the mass transfer effectiveness factor to observe the limiting steps was estimated. The following equations were considered:

- Shrinking core model:

$$r = \frac{dX}{dt} = k_{SCM}\,(1 - X)^{2/3} \tag{3.6}$$

- Arrhenius equation:

$$k = k_o \exp\left(-\frac{E_A}{RT}\right) \tag{3.7}$$

- Rate law:

$$r = k\,(1 - X)^n \tag{3.8}$$

- Effectiveness factor:

$$\eta = \frac{\text{global reaction rate}}{\text{intrinsic reaction rate}} \tag{3.9}$$

where: r is reaction rate (mol/g min); X is conversion (-); t is time (min); k_{SCM} is the shrinking core model reaction rate constant ($mol^{1-n}\, g^{n-2}/min$); k_o is the frequency factor ($mol^{1-n}\, g^{n-2}/min$); E_A is activation energy (kJ/mol); R is the universal gas constant (J/mol K); and T is absolute temperature (K).

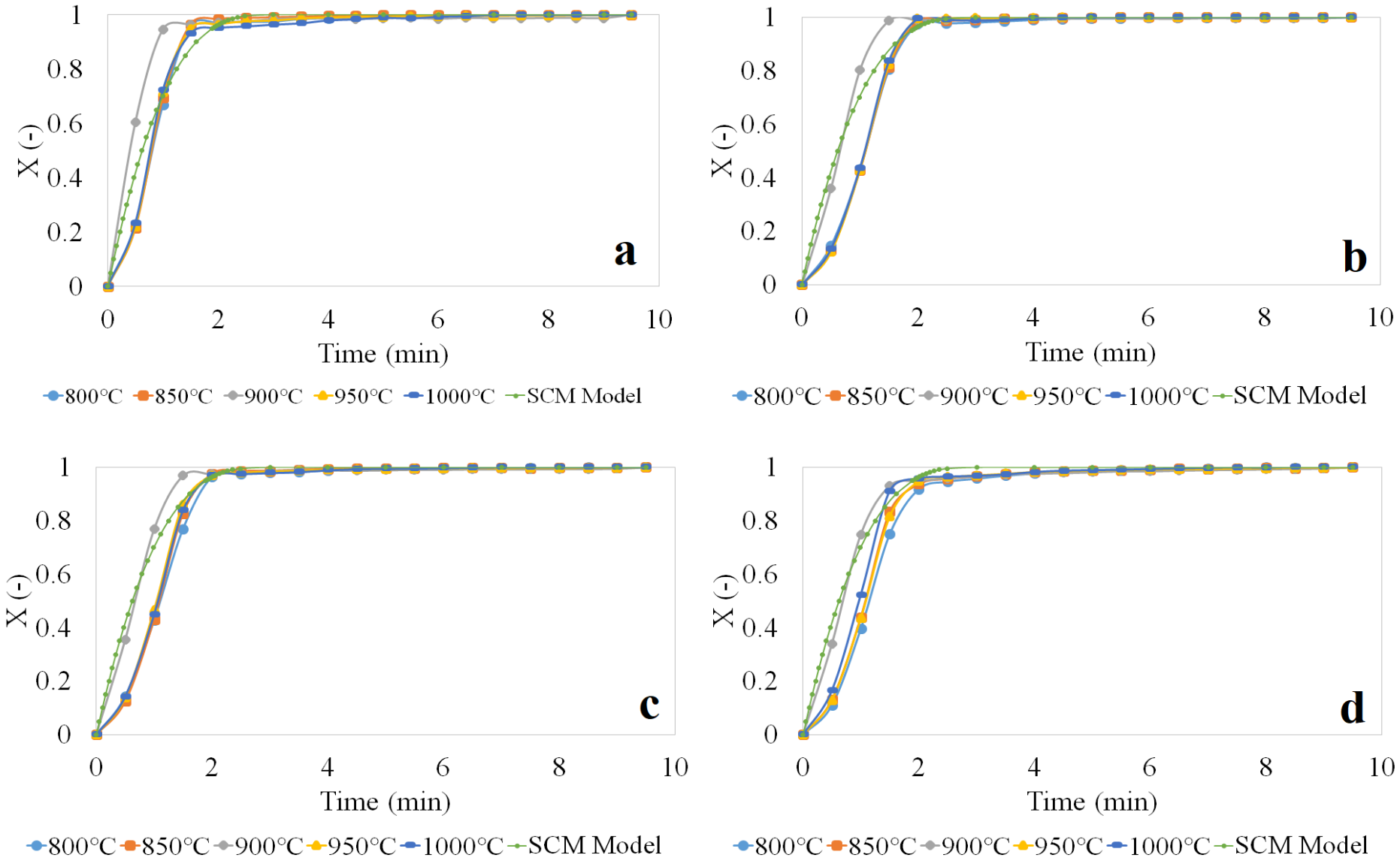

Fig. 3.9. Conversion profile (oxidation) of Ni-Co precursor deposited on (a) Al_2O_3, (b) CeO_2, (c) TiO_2; and, (d) ZrO_2.

The oxidation conversion profiles for all supported oxygen carriers are shown in Figs. 3.9–3.11. In the first 2 min of air exposure and when temperature ranged from 800°C-1000°C, about 90% of conversion was achieved for all samples; however, the 900°C oxidation reaction temperature showed improvements in the conversion rate for all samples.

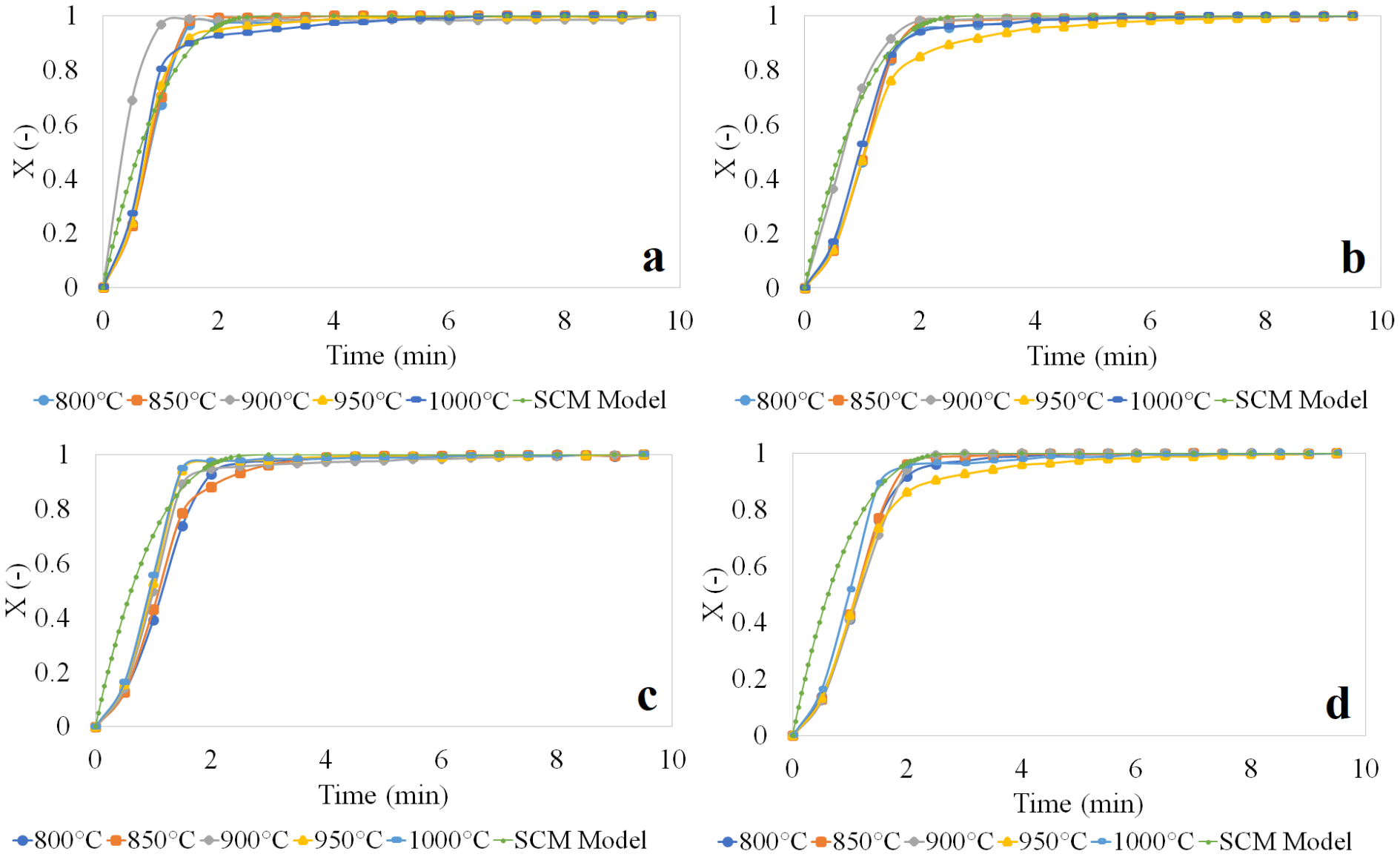

Fig. 3.10. Conversion profile (oxidation) of Ni-Cu precursor deposited on (a) Al_2O_3, (b) CeO_2, (c) TiO_2; and, (d) ZrO_2.

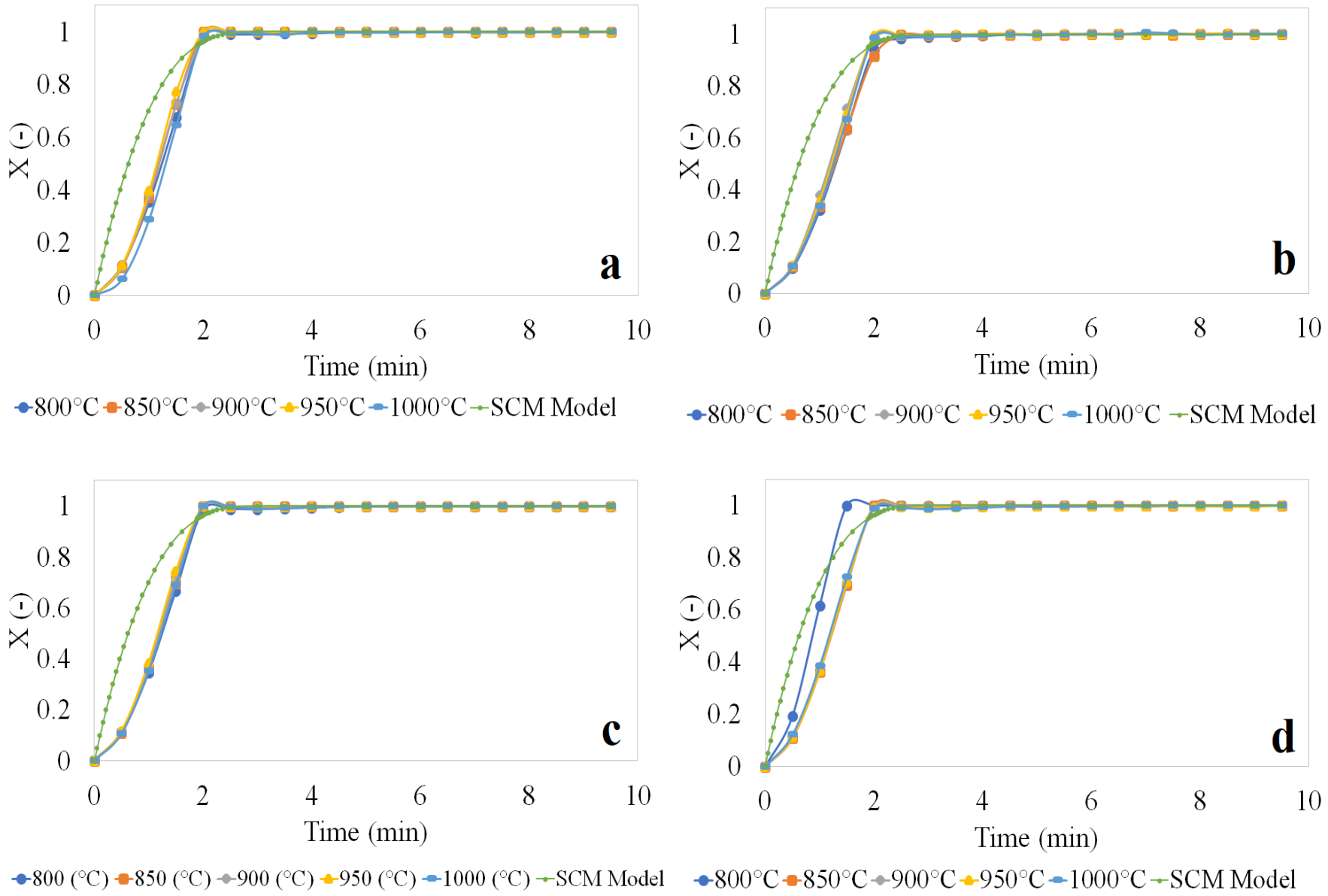

Fig. 3.11. Conversion profile (oxidation) of Ni-Fe precursor deposited on (a) Al_2O_3, (b) CeO_2, (c) TiO_2; and, (d) ZrO_2.

Eqns. (3.6) and (3.7) were used twice: for the surface reaction limited regime, and for the mass transfer limited regime to estimate the intrinsic and global activation energies, respectively, within the oxidation period (Fig. 3.8a). The internal effectiveness factor for the oxygen carriers was calculated using Eq. (9) and it is shown in Fig. 3.12. Three regimes were attributed to the effectiveness factor: 1) isothermal internal diffusion controlling condition, 2) isothermal surface reaction controlling condition, and 3) non-isothermal surface reaction controlling condition. As shown in Fig. 3.12, the effectiveness factor of Ni-Co/CeO_2, Ni-Co/TiO_2, Ni-Cu/Al_2O_3, Ni-Cu/CeO_2, Ni-Cu/ZrO_2 and Ni-Fe/CeO_2 samples indicated that internal diffusion was the controlling condition, which means no significant temperature difference existed between the inside of the sample and its surface (isothermal condition). The effectiveness factor of the Ni-Fe/TiO_2 and Ni-Fe/ZrO_2 samples was within the transition regime of internal diffusion and surface reaction conditions (Fig. 3.12). This means the rates of both reaction and internal diffusion for Ni-Fe/TiO_2 and Ni-Fe/ZrO_2 samples were similar. The effectiveness factor of the Ni-Cu/TiO_2 sample showed isothermal surface reaction was the controlling condition rather than the internal diffusion, indicating that pore diffusion within this sample was negligible. The non-isothermal condition existed in the Ni-Co/Al_2O_3, Ni-Co/ZrO_2, and Ni-Fe/Al_2O_3 samples where the effectiveness factor was found to be greater than 1.

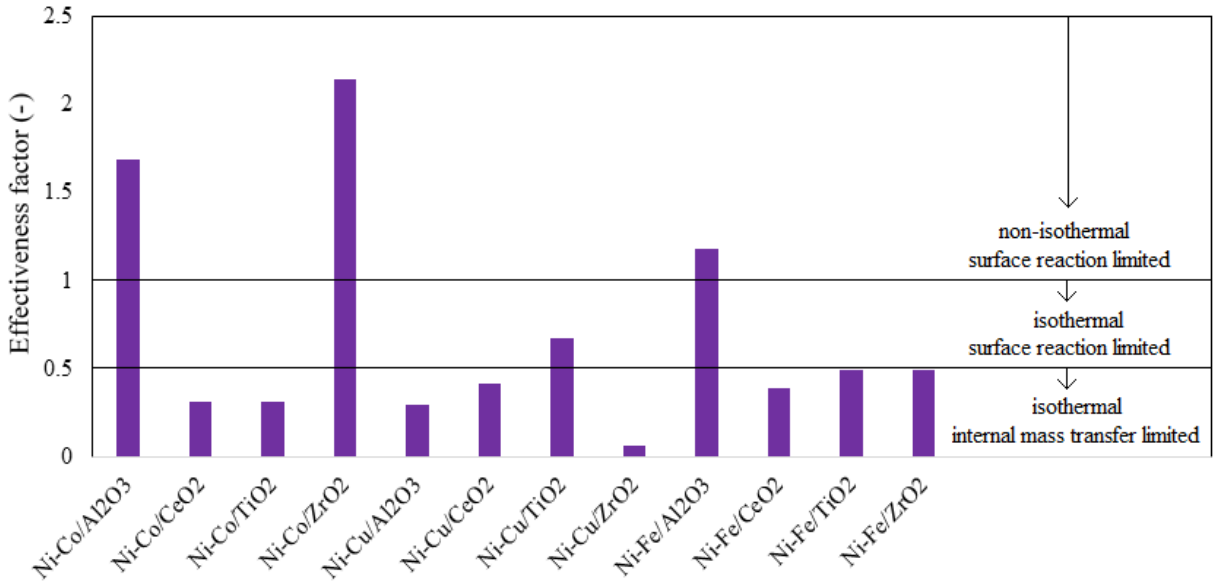

Fig. 3.12. Internal effectiveness factor of bimetallic oxygen carriers.

Based on the effectiveness values for all samples, it can be concluded that interaction between precursors and supports could evidence the internal diffusion condition for some samples (i.e. Ni-Co/CeO_2, Ni-Co/TiO_2, Ni-Cu/CeO_2, and Ni-Fe/CeO_2); however, when no possible interaction between precursors and supports existed, surface reaction condition was the controlling condition. The deposition of precursors inside the supports' pores during the impregnation and the presence of exothermic oxidation reaction inside the pores are indications of temperature difference between the sample inside and its surface, which explains the greater than 1 the effectiveness factor of the Ni-Co/Al_2O_3, Ni-Co/ZrO_2, and Ni-Fe/Al_2O_3 samples. No possible interaction between precursors and supports in the Ni-Cu/Al_2O_3 and Ni-Cu/ZrO_2 samples was noticed; however, isothermal and internal mass transfer conditions were found in these samples. This may indicate that the precursors in these two samples were deposited deep into the pores during the impregnation, which resulted in decreasing their oxygen capacity (due to the internal

diffusion) by the increased formation of carbon (pores blockage) during the reduction reaction (refer to Fig. 3.6 for oxygen capacity comparison).

3.5.2.2.2. Reduction reaction

The reduction profiles for bimetallic oxygen carriers are shown in Figs. 3.13–3.15. Generally speaking, as temperature increased (800-1000°C), reduction profile occurred more rapidly for all samples, except for the Ni-Cu/Al_2O_3 sample where minor effects of temperature on the reduction profile were observed. This could mean that the precursors in the Ni-Cu/Al_2O_3 sample were readily available for reduction without the presence of a mass transfer effect.

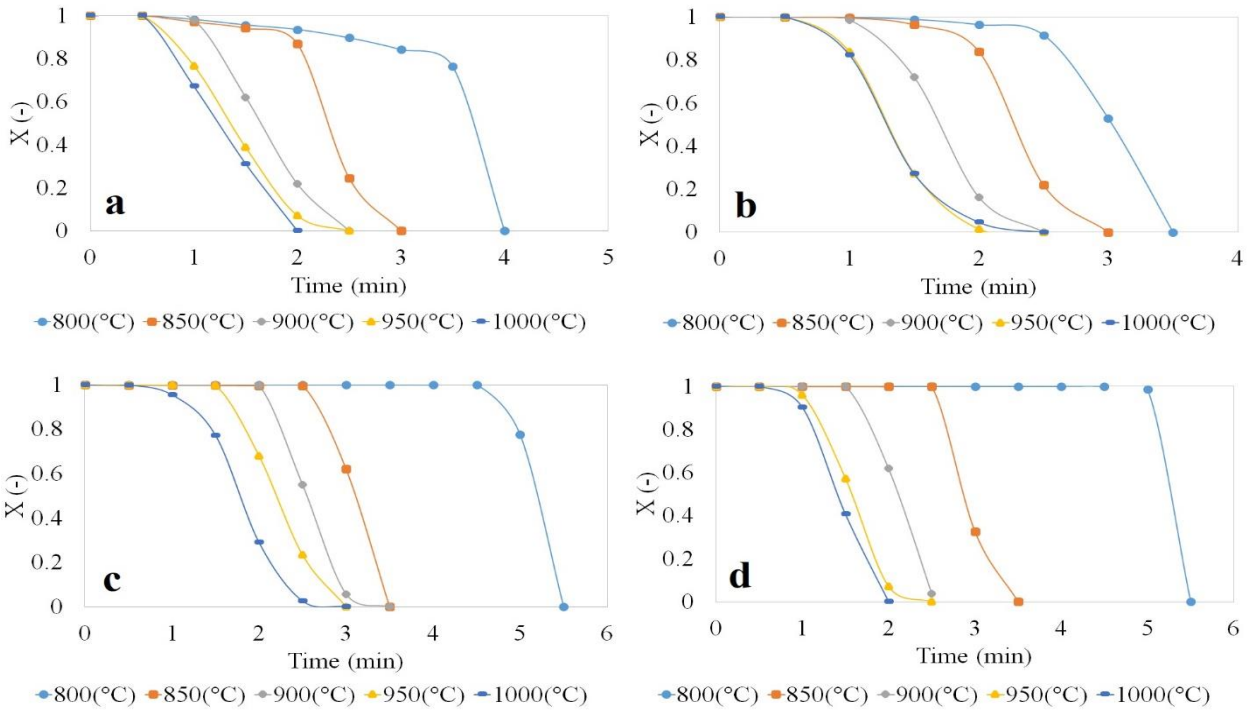

Fig. 3.13. Conversion profile (reduction) of Ni-Co precursor deposited on (a) Al_2O_3, (b) CeO_2, (c) TiO_2; and, (d) ZrO_2.

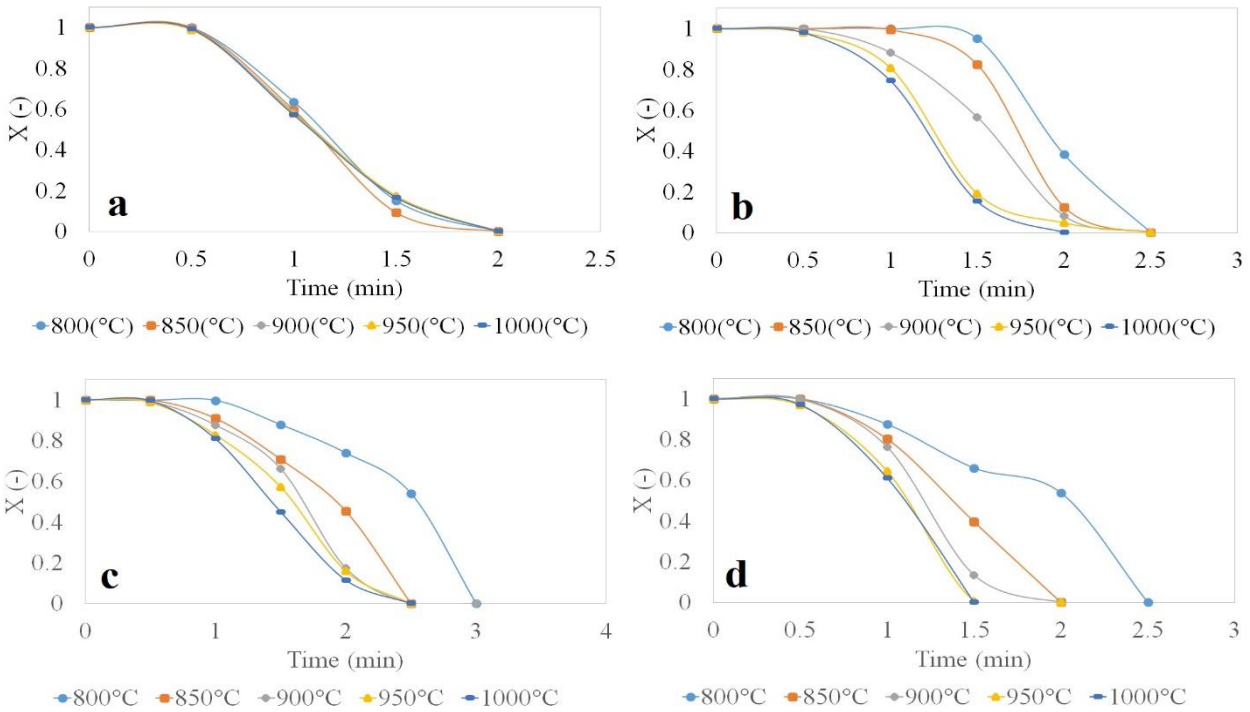

Fig. 3.14. Conversion profile (reduction) of Ni-Cu precursor deposited on (a) Al_2O_3, (b) CeO_2, (c) TiO_2; and, (d) ZrO_2.

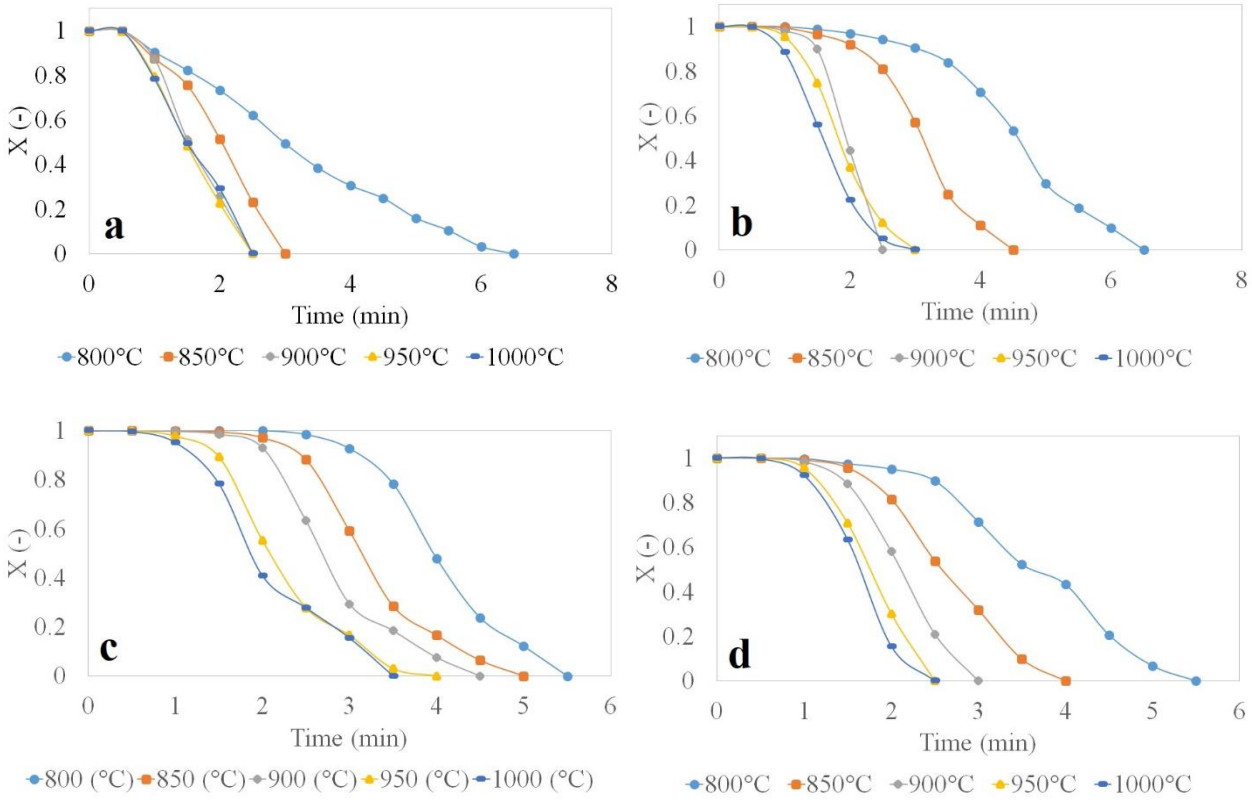

Fig. 3.15. Conversion profile (reduction) of Ni-Fe precursor deposited on (a) Al_2O_3, (b) CeO_2, (c) TiO_2; and, (d) ZrO_2.

Evaluation of activation energy for the reduction reaction was performed at different solid conversion levels (X: 30%, 50%, 70% and 90%) to determine the reaction pathways that were dominant during the reduction reaction of bimetallic oxygen carriers. The kinetic method used to evaluate the kinetic parameters for the reduction reaction is discussed in detail in [16]. However, the main equation used is as follows [29]:

$$1/t_X(T) = k_o - G(X) + e^{\frac{-E_r}{RT}} \quad (3.10)$$

where: t_X is residence time (min); X is conversion (-); T is absolute temperature (K); G(X) is conversion dependent function (-); k_o is the frequency factor (1/min); Er is activation energy of reduction reaction (kJ/mol); and R is the universal gas constant (kJ/mol K).

The comparison between the oxygen capacity and activation energy of supported monometallic and bimetallic oxygen carriers is shown in Table 3.2. The first set of samples, shown in Table 3.2, is the bimetallic combination of Ni and Co samples with different supports. The supported Ni-Co samples showed higher activation energy than the monometallic samples of either Ni or Co; however, the oxygen capacity of supported Ni-Co samples was lesser than oxygen capacity of supported monometallic samples of Ni and Co except for Ni-Co/Al_2O_3 sample, which showed a 12.42% more oxygen capacity than Ni/Al_2O_3 and Co/Al_2O_3 samples. The second set of combination is the supported Ni, Cu and Ni-Cu samples. The activation energy of the supported Ni-Cu was lower than the supported monometallic samples. The oxygen capacity of supported bimetallic samples (Ni-Cu) were quite similar to the monometallic samples (~13.45% or less by difference). The third set of combination is the supported Ni, Fe, and Ni-Fe samples. The highest activation energy of 67.47 kJ/mol was reported for the Ni-Fe/CeO_2 sample with highest oxygen capacity of 14.73%. Moreover, the oxygen capacity of supported Ni-Fe samples was higher than the monometallic samples. It can be concluded with that the increase in the activation energy of

bimetallic samples favoured increases in their oxygen capacity. The effect of activation energy on the oxygen capacity will next be considered for determination of governing reaction pathways of bimetallic oxygen carriers.

Table 3.2 Comparison of activation energy and oxygen capacity of mixed carriers

Sample			
Precursor	Support	Activation energy, Er (kJ/mol)	Oxygen capacity (g/g)
Ni		53.89*	4.40*
Co	Al_2O_3	17.12*	4.62*
Ni-Co		79.77	10.14
Ni		32.74*	7.10*
Co	CeO_2	34.01*	7.92*
Ni-Co		71.30	11.96
Ni		67.72*	7.09*
Co	TiO_2	50.49*	8.84*
Ni-Co		75.01	11.81
Ni		63.68*	4.78*
Co	ZrO_2	83.80*	5.39*
Ni-Co		94.49	9.89
Ni		53.89*	4.40*
Cu	Al_2O_3	8.00*	4.05*
Ni-Cu		2.61	8.81
Ni	CeO_2	32.74*	7.10*

Cu		46.37*	5.12*
Ni-Cu		43.56	10.99
Ni		67.72*	7.09*
Cu	TiO_2	51.12*	4.43*
Ni-Cu		35.24	9.97
Ni		63.68*	4.78*
Cu	ZrO_2	72.68*	4.28*
Ni-Cu		24.97	9.71
Ni		53.89*	4.40*
Fe	Al_2O_3	2.80*	2.42*
Ni-Fe		20.06	11.55
Ni		32.74*	7.10*
Fe	CeO_2	42.81*	7.97*
Ni-Fe		67.47	14.73
Ni		67.72*	7.09*
Fe	TiO_2	9.51*	4.00*
Ni-Fe		59.77	14.20
Ni		63.68*	4.78*
Fe	ZrO_2	89.41*	4.68*
Ni-Fe		43.74	12.28

* [16], estimated.

Tables 3.3-3.5 show the activation energy for the reduction reaction at different solid conversion levels. As the solid conversion level increased, activation energy increased for Ni-Co supported with TiO_2 and ZrO_2 supports (Table 3.3). However, the opposite trend of conversion versus activation energy was observed for the Ni-Co supported with Al_2O_3 sample (Table 3.3). The Ni-Co/CeO_2 sample (Table 3.3) showed a fluctuating activation energy trend when solid conversion increased. The change in the activation energy with solid conversion level is an indication of multiple reactions taking place in the same sample. Thus, by comparing the activation energy of bimetallic samples (Table 3.3) and the values of activation energy of a single metal precursor presented in [16], the reaction pathways of bimetallic precursors can be predicted (considering loading percentage and experimental errors). The reaction pathways for supported Ni-Co precursors with Al_2O_3, CeO_2, TiO_2 and ZrO_2 are shown in Fig. 3.16. New forms of metals / metal oxides were predicted in all supported Ni-Co precursors expect for the supported sample with ZrO_2. Oxidation of support was observed in the Ni-Co precursor supported by Al_2O_3. The nickel aluminum spinel ($NiAl_2O_4$) did not reduce, which caused a decrease in the oxygen capacity of the Ni-Co/Al_2O_3 sample. New phases (NiCe, $NiCe_2O_3$ and $NiTi_2O_3$) when the supports were reduced after the precursors' oxidation of methane caused increases in the oxygen capacity of the Ni-Co/CeO_2 and Ni-Co/TiO_2 samples. The weak chemical stability between each precursor favored complete reduction of bimetallic precursors; however, the presence of an oxygen-free precursor (i.e. Ni) facilitated further reduction of some supports. In contrast, the strong chemical stability between Ni and Co precursors facilitated earlier reduction of support than the Co_3O_4 precursor (Fig. 3.16).

Table 3.3 Reduction activation energy at different solid conversion level for supported Ni-Co precursor

Sample \ Conversion (-)	Activation energy (kJ/mol)			
	0.30	0.50	0.70	0.90
Ni-Co/Al_2O_3	53.12	62.20	74.41	79.77
Ni-Co/CeO_2	47.73	52.09	56.45	71.30
Ni-Co/TiO_2	51.81	56.78	59.34	75.01
Ni-Co/ZrO_2	66.99	75.32	83.10	94.49

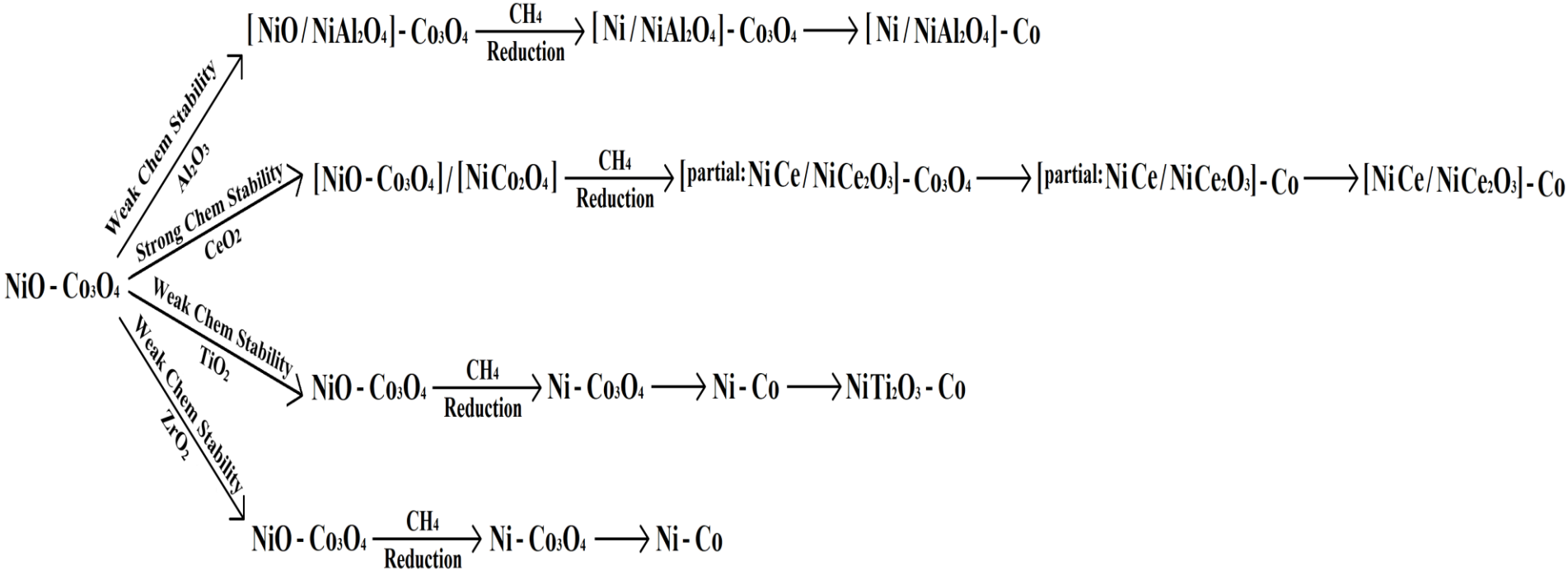

Fig. 3.16. Pathways to reduction reactions of supported Ni-Co precursor.

The activation energy of Ni-Cu/Al_2O_3 (Table 3.4) increased as solid conversion increased up to 70%, but then decreased at higher levels of solid conversion, indicating that reduction of $NiAl_2O_4$ to Ni and Al_2O_3 occurred first, followed by reduction of NiO to Ni (Fig. 3.17). As conversion increased for Ni-Cu/CeO_2 and Ni-Cu/TiO_2 samples (Table 3.4), the activation energies increased for both samples with a transition state of around 50% conversion, which indicated the formation of phases of NiCe, $NiCe_2O_3$ and $NiTi_2O_3$ (Fig. 3.17). No new phases were predicted in the Ni-Cu/ZrO_2 sample; however, complete reduction of precursors was predicted. The chemical stability between the Ni and Cu precursors supported with Al_2O_3, TiO_2, and ZrO_2 supports was weak except for the supported Ni and Cu precursors with CeO_2 support, which showed an unchanged chemical stability (the estimated activation energies in Table 3.4 and those reported values in [16] were close) that perhaps caused an earlier reduction of support CeO_2 than the CuO precursor (Fig. 3.17).

Table 3.4 Reduction activation energy at different solid conversion level for supported Ni-Cu precursor

	Activation energy (kJ/mol)			
Sample \ Conversion (-)	0.30	0.50	0.70	0.90
Ni-Cu/Al_2O_3	0.40	2.51	3.97	2.61
Ni-Cu/CeO_2	25.73	32.55	31.65	43.56
Ni-Cu/TiO_2	25.06	30.65	32.11	35.24
Ni-Cu/ZrO_2	32.27	33.67	23.66	24.97

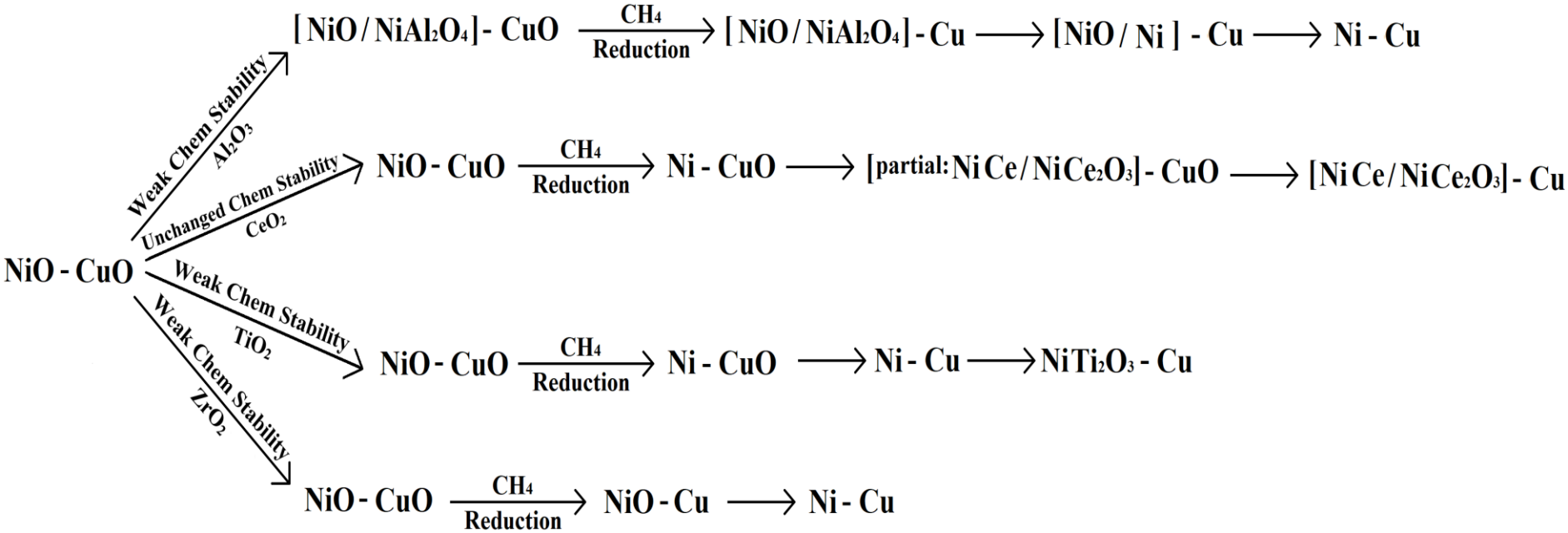

Fig. 3.17. Pathways to reduction reactions of supported Ni-Cu precursor.

The activation energy of supported Ni-Fe precursors increased as conversion increased for all samples (Table 3.5). Slight transition in the activation energy was observed in the Ni-Fe/CeO_2 and Ni-Fe/TiO_2 samples, which indicated partial reduction of both CeO_2 and TiO_2 to NiCe and/or $NiCe_2O_3$, and $NiTi_2O_3$, respectively (Fig. 3.18). Strong chemical stability between Ni and Fe precursors was noticed with Al_2O_3 and CeO_2 supports. This strong chemical stability prevented the interaction between Ni-Fe and Al_2O_3 support and limited the formation of NiCe and/or $NiCe_2O_3$ when CeO_2 was deployed. The chemical stability between NiO and Fe_2O_3 weakened when TiO_2 support was used, which later showed a noticeable transition in the activation energy between 50% and 70% solid conversion (Table 3.5). Chemical stability remained unchanged for the supported Ni-Fe precursor with ZrO_2 due to the presence of the thermally stable support (i.e. ZrO_2).

Table 3.5 Reduction activation energy at different solid conversion level for supported Ni-Fe precursor

	Activation energy (kJ/mol)			
Sample \ Conversion (-)	0.30	0.50	0.70	0.90
Ni-Fe/Al_2O_3	39.48	39.63	36.98	20.06
Ni-Fe/CeO_2	55.71	60.87	50.73	67.47
Ni-Fe/TiO_2	36.94	42.98	48.22	59.77
Ni-Fe/ZrO_2	39.33	40.21	40.49	43.74

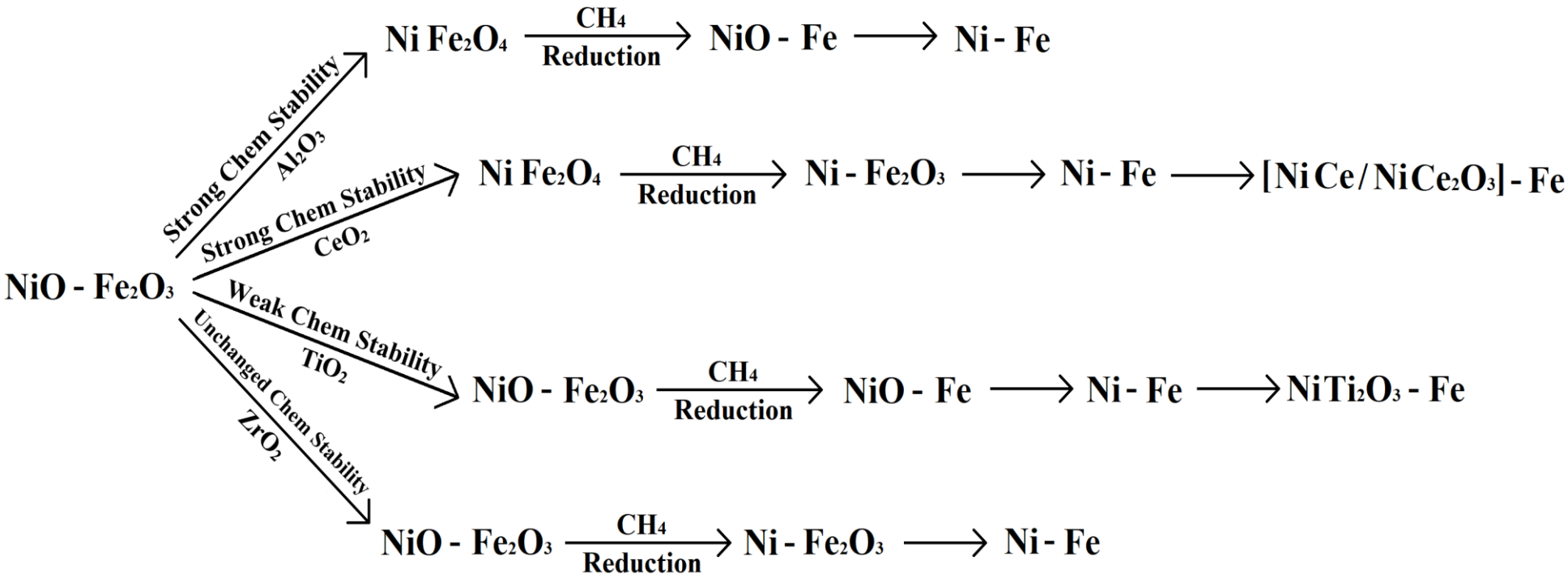

Fig. 3.18. Pathways to reduction reactions of supported Ni-Fe precursor.

3.6. Conclusion

Bimetallic (Ni, Co, Cu, Fe) precursors supported by (Al_2O_3, CeO_2, TiO_2, ZrO_2) were successfully synthesized using the incipient wetness impregnation technique to access their reactivity in a methane-fuelled chemical looping combustion process. By characterizing the synthesized samples, the BET surface area and pore volume decreased for all samples due to sintering of particles, except for the Ni-Co/TiO_2, Ni-Cu/TiO_2, Ni-Fe/Al_2O_3, and Ni-Fe/ZrO_2 samples, where either or both surface area and pore volume increased. Noticeable interaction between precursors and supports was observed especially in the samples supported with CeO_2 and TiO_2 supports due to reduction of supports. The internal mass transfer phenomenon impacted most samples during the oxidation reaction, indicating that as soon as an interaction between precursors and supports existed, pore diffusion was more dominant than surface reaction, and vice versa. It was noticed that during the reduction reaction with methane, precursors with weak chemical stability had a tendency to be reduced earlier to further interact with the supports, resulting in increases in their oxygen capacity. Furthermore, the stronger the chemical stability between bimetallic precursors during synthesis, the less likely the occurrence of precursors-supports interactions, which in turn inhibited the oxygen capacity of bimetallic samples, mostly at reduction temperatures that were lower than 850°C. In summary and for practical deployment of oxygen carriers in the CH_4-CLC process, the operating condition of a 10-min oxidation cycle with air at a flow rate of 20 ml/min and a 10-min reduction cycle with 40% CH_4 balanced with N_2 at a flow rate of 20 ml/min, the most stable samples in term of oxygen transport capabilities at elevated temperature (800°C-1000°C) and absence of precursor-support interaction were: Ni-Co/ZrO_2, Ni-Cu/ZrO_2, and Ni-Fe/ZrO_2.

3.7. Acknowledgements

The authors would like to acknowledge the Natural Sciences and Engineering Research Council (NSERC) of Canada ─ Industrial Research Chairs (IRC) program, Canadian Natural Resources Limited (CNRL), and Devon Canada for funding this study. The authors would like to acknowledge the Ministry of Education (MOE) in the Kingdom of Saudi Arabia. The authors appreciate the contribution of Alan Kim, Jun Daniel Jeong and Tristan Hannequin in the experimental work of this study. The authors would like also to acknowledge Dr. Azfar Hassan for the helpful discussion and data interpretation about the H_2-TPR analysis.

3.8. References

[1] Change, I. P. O. C. (2007). Climate change 2007: The physical science basis. Agenda, 6(07), 333.

[2] Adanez J, Abad A, Garcia-Labiano F, Gayan P, Luis F. Progress in chemical-looping combustion and reforming technologies. Prog. Energy Combust. Sci. 2012; 38(2): 215-282.

[3] Hossain M M, de Lasa H I. Chemical-looping combustion (CLC) for inherent CO_2 separations-a review. Chem. Eng. Sci. 2008; 63(18): 4433-4451.

[4] Kerr H R. Capture and Separation Technology Gaps and Priority Research Needs-Chapter 38.

[5] Ishida M, Zheng D, Akehata T. Evaluation of a chemical-looping-combustion power-generation system by graphic exergy analysis. Energy 1987; 12: 147-154.

[6] Zheng X, Su Q, Mi W. Study of a Cu-Based oxygen carrier based on a chemical looping combustion process. Energy Fuels. 2015; 29(6): 3933-3943.

[7] Harper R N, Boyce C M, Scott S A. Oxygen carrier dispersion in inert packed beds to improve performance in chemical looping combustion. Chem. Eng. J. 2013; 234: 464-474.

[8] Zhu J, Wang W, Hua X N, Wang F, Xia Z, Deng Z. Phase distribution and stepwise kinetics of iron oxides reduction during chemical looping hydrogen generation in a packed bed reactor. Int. J. Hydrogen Energy. 2015; 40(36): 12097-12107.

[9] Hamers H P, Gallucci F, Williams G, van Sint Annaland M. Experimental demonstration of CLC and the pressure effect in packed bed reactors using $NiO/CaAl_2O_4$ as oxygen carrier. Fuel. 2015; 159: 828-836.

[10] Song Q, Xiao R, Deng Z, Zhang H, Shen L, Xiao J, Zhang M. Chemical-looping combustion of methane with $CaSO_4$ oxygen carrier in a fixed bed reactor. Energy Convers. Manag. 2008; 49(11); 3178-3187.

[11] Frick V, Rydén M, Leion H. Investigation of Cu–Fe and Mn–Ni oxides as oxygen carriers for chemical-looping combustion. Fuel Process. Technol. 2016; 150: 30-40.

[12] Hossain M M, de Lasa H I. Reduction and oxidation kinetics of Co–Ni/Al_2O_3 oxygen carrier involved in a chemical-looping combustion cycles. Chem. Eng. Sci. 2010; 65(1): 98-106.

[13] Jiang S, Shen L, Wu J, Yan J, Song T. The investigations of hematite-CuO oxygen carrier in chemical looping combustion. Chem. Eng. J. 2017; 317: 132-142.

[14] Siriwardane R, Tian H, Simonyi T, Poston J. Synergetic effects of mixed copper–iron oxides oxygen carriers in chemical looping combustion. Fuel. 2013; 108: 319-333.

[15] Bhavsar S, Tackett B, Veser G. Evaluation of iron-and manganese-based mono-and mixed-metallic oxygen carriers for chemical looping combustion. Fuel 2014; 136: 268-279.

[16] Tijani M M, Aqsha A, Mahinpey N. Synthesis and study of metal-based oxygen carriers (Cu, Co, Fe, Ni) and their interaction with supported metal oxides (Al_2O_3, CeO_2, TiO_2, ZrO_2) in a chemical looping combustion system. Energy 2017; 138: 873-882.

[17] Kwon Y S, Savitskii A, Solid-state sintering of metal powder mixtures. J. Mater. Synth. Process. 2001; 9(6): 299-317.

[18] Ishida M, Jin H. A novel chemical-looping combustor without NOx formation. Ind. Eng. Chem. Res. 1996; 35(7): 2469-2472.

[19] Mullins D R, Zhang K Z. Metal–support interactions between Pt and thin film cerium oxide. Surf. Sci. 2002; 513(1): 163-173.

[20] Li S, Xu Y, Chen Y, Li W, Lin L, *et al* Tuning the Selectivity of Catalytic Carbon Dioxide Hydrogenation over Iridium/Cerium Oxide Catalysts with a Strong Metal-Support Interaction. Angew. Chem. Int. Ed. (in English). 2017; 56(36): 10761-10765.

[21] Ji Y, Zhao Z, Duan A, Jiang G, Liu J. Comparative study on the formation and reduction of bulk and Al_2O_3-supported cobalt oxides by H_2-TPR technique. J. Phys. Chem. C. 2009; 113(17): 7186-7199.

[22] Pires C A, Dos Santos A C C, Jordão E. Oxidation of phenol in aqueous solution with copper oxide catalysts supported on γ-Al_2O_3, pillared clay and TiO_2: Comparison of the performance and costs associated with each catalyst. Braz. J. Chem. Eng. 2015; 32(4): 837-848.

[23] Batista M S, Wallau M, Urquieta-González E A. Species active in the selective catalytic reduction of no with iso-butane on iron-exchanged ZSM-5 zeolites. Braz. J. Chem. Eng. 2005; 22(3): 341-351.

[24] Sá J, Kayser Y, Milne C J, Fernandes D L A, Szlachetko J. Temperature-programmed reduction of NiO nanoparticles followed by time-resolved RIXS. Phys. Chem. Chem. Phys. 2014; 16(17): 7692-7696.

[25] Hossain M M, de Lasa H I. Reactivity and stability of Co-Ni/Al_2O_3 oxygen carrier in multicycle CLC. AIChE J. 2007; 53(7): 1817-1829.

[26] Roy B, Leclerc C A. Study of preparation method and oxidization/reduction effect on the performance of nickel-cerium oxide catalysts for aqueous-phase reforming of ethanol. J. Power Sources. 2015; 299: 114-124.

[27] Sekimoto H, Shioi R, Uda T, Awakura Y, Sato S. Reduction of titanium oxide to titanium alloy by hydrogen. In 3rd Workshop on Reactive Metal processing March 2007.

[28] Cho P, Mattisson T, Lyngfelt A. Carbon formation on nickel and iron oxide-containing oxygen carriers for chemical-looping combustion. Ind. Eng. Chem. Res. 2005; 44(4): 668-676.

[29] Tijani M M, Aqsha A, & Mahinpey N. X-ray Diffraction and TGA kinetic analyses for Chemical Looping Combustion Applications. Data in Brief. 2017; 17: 200-209.

CHAPTER FOUR: Process simulation and thermodynamic analysis of a chemical looping combustion system using methane as fuel and NiO as oxygen carrier in a moving bed reactor

Chemical Engineering and Processing-Process Intensification. Submitted (2018)

4.1. Presentation of the article

The paper presents a case study to assess the viability of the CLC process when supported nickel oxide with alumina carrier is used for the methane CLC process. Aspen Plus computer software was used to provide kinetic and thermodynamic evaluations of a micro-reactor system in the methane-fueled CLC process. Different limitations on the conversion of methane and carrier were studied, such as formation of carbon, formation of nickel alumina spinel, and mass transfer. The results showed that a maximum methane conversion of 99.44% was achieved; however, the formation of intermediates such as carbon monoxide and hydrogen increased too. Moreover, a complete conversion from methane to carbon dioxide and water was obtained with the non-catalytic gas-solid reaction, while as the entering molar flow rate increased from 1×10^{-9} kmol/s to 100 kmol/s, methane conversion decreased from 100% to almost 50%.

Most of this work was conducted by Tijani, M. M. Dr. Mostafavi, E. assisted in training Tijani, M. M. on how to use Aspen Plus software, and helped in reviewing the results and manuscript before submission. Prof. Mahinpey, N. supervised this work, reviewed the manuscript, and provided financial assistance to install Aspen Plus software.

Process simulation and thermodynamic analysis of a chemical looping combustion system using methane as fuel and NiO as oxygen carrier in a moving bed reactor

This article has been submitted to Chemical Engineering and Processing-Process Intensification in August 2018 and is under review

Mansour Mohammedramadan Tijani, Ehsan Mostafavi, Nader Mahinpey

Department of Chemical and Petroleum Engineering, Schulich School of Engineering, University of Calgary, Calgary, AB, T2N 1N4, Canada

4.2. Abstract

The increase in carbon dioxide ($CO_{2)}$ emissions to the atmosphere is considered a major contributor to global warming. Several technologies have emerged in the last decades to capture $CO_{2,}$ with the chemical looping combustion (CLC) process being a promising approach to mitigate the emission of CO_2. The CLC process produces a concentrated stream of CO_2 through the indirect combustion of fuel with oxygen. The produced CO_2 is then compressed and transported to either storage or utilization. This study provides comprehensive evaluation and sensitivity analysis of the methane chemical looping combustion process in Aspen Plus, using a micro-reactor system, and nickel oxide supported by alumina as oxygen carrier. The effect of various parameters and limitations, as well as thermodynamic evaluations, was investigated, so the outcomes of this study should be beneficial for scaling up the CLC process using a nickel-based oxygen carrier. By varying the reaction temperature from 700°C to 1200°C in the fuel reactor, the maximum achievable conversion of methane was 99.44%. The effect of pressure of the fuel reactor (20 bar to 40 bar) on the conversion of methane showed that a complete conversion of methane to carbon dioxide and water was obtainable (at higher pressures), but the formation of intermediates was minimal. Once the entering flow rate varied (1×10^{-9} kmol/s to 100 kmol/s), the methane

conversion decreased from 100% to nearly 50%. However, the comparison between the reported experimental results in the literature and this study's results showed a good agreement with no significant mass transfer effect on the kinetics.

4.3. Introduction

A well-known global issue is anthropogenic CO_2 emissions, a major greenhouse gas (GHG) emitted in massive amounts to the atmosphere, which may cause irreversible and disastrous damages to the planet, (e.g. climate change). Industries all over the world are now in charge with reducing their carbonaceous GHG emissions to the atmosphere in order to curb global warming. As carbon dioxide emissions are increasing at an alarming rate [1], research on carbon capture and utilization is more imperative than ever. Many technologies have emerged in the last decades for the capture of carbon dioxide [2]. On the one hand, a prime example of some technologies is CO_2 adsorption, which uses solid sorbents such as zeolites or activated carbon to selectively adsorb carbon dioxide [3]. On the other hand, the Rectisol process is a physical absorption process. Selexol and amine solvents are known to be chemical absorption processes through which chemically reactive solvents such as monoethanolamine (MEA) are employed to come to contact with and remove carbon dioxide from flue gas streams [4]. Hence, regeneration of the sorbents and/or solvents are energy-intensive and costly [4], [5], where the regeneration efficiency is relatively low to capture the tremendous amounts of carbon dioxide found in flue gas [6]. A recently emerging technology called chemical-looping combustion, which produces a concentrated stream of carbon dioxide without employing any expensive carbon capture unit, is being further developed thanks to its numerous advantages: predicted low cost, low energy, high efficiency [6].

The growing interest in this technology is justified by a low-combustion cost and a selective capturing of carbon dioxide. It also eliminates the formation of NO_x emission owing to the absence of flame and nitrogen during the combustion of different fuel types (e.g. gas and solids). This technology can be integrated into a fossil fuel-based power plant to limit carbon dioxide emission to the atmosphere as well as to produce a pure stream of carbon dioxide that can be later stored or utilized. The CLC system is based on two interconnected fluidized-bed reactors operating in a cyclic movement (Fig. 4.1). The reactor system consists of a fuel reactor and an air reactor, where an oxygen carrier (a metal-based catalyst) circulates in the reactor system to transfer the necessary oxygen for the indirect combustion of fuel. In the fuel reactor, methane or any kind of syngas

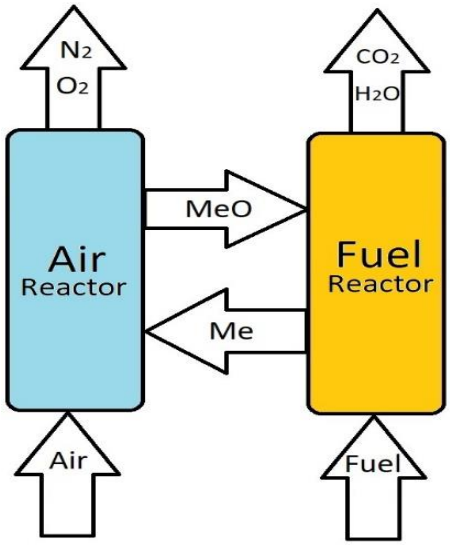

Fig. 4.1. Chemical looping combustion process.

(CO/H_2) and solid fuel like coal reacts with the oxide form of the metal-based oxygen carriers to be reduced to its metal form, contributing to the combustion of methane to produce carbon dioxide and water. The reaction temperature in the reactor system can range from 600°C to 1200°C and the pressure depends on the reactor type (e.g. fixed-bed: 10-40 bar; fluidized-bed: 1-10 bar) [8].

The carbon dioxide is then separated from steam by condensation and compression up to 150 bars (critical phase) to be easily pipelined for transportation and/or storage. In the air reactor, air is used to regenerate the metal form to the oxidized form as follows:

$$\text{Oxidized form: } 2Me_xO_{y-1} + O_2 \rightarrow 2Me_xO_y \quad (4.1)$$

$$\text{Reduced form: } Me_xO_y + C_nH_{2m} \rightarrow (2n+m)Me_xO_{y-1} + nCO_2 + mH_2O \quad (4.2)$$

One important parameter to consider is the metal found in the oxygen carrier and that of its support. In fact, the redox reactions remain the same no matter what metal-based oxygen carriers are being used, but each metal could modify the energy barrier (activation energy), as well as the stability of the oxygen carriers' particles. For this matter, the oxygen carriers must have high chemical reactivity (both oxidation and reduction reactions) and thermal stability [9]. In the fluidization process, the oxygen carriers should be fluidizable at high temperatures. However, the density and pore structure of the oxygen carriers should remain unchanged throughout the cyclic operation to give better redox reaction rates. Iron, nickel, copper and manganese-based oxygen carriers have been investigated because of their superiority compared to other metals. It is found that calcium sulfide, cobalt, nickel and copper have the highest oxygen capacities among other metals [8]. However, calcium sulfide and cobalt may cause health and environmental concerns. Nevertheless, lower temperatures should be used for copper oxide, because of its low melting point (1063 °C at 1 bar). Nowadays, nickel oxide seems to be the most usable metal in CLC processes despite its tendency to deposition of coke and some toxicity issues.

Abad *et al* [10] found the optimum ratio of oxygen carrier to fuel to be between 1.7 and 4, with a combustion efficiency of 99.9% at 700°C for a methane-fueled CLC system with a 14 wt% loading of CuO. Bakare *et al* [11] investigated the kinetics of VO_x-MoO_x/Al_2O_3 as an oxygen carrier in a C_2H_6-fueled fluidized-bed reactor, finding that a temperature of 650°C and residence

time of 30s favoured formation of COx among other gases. Jin and Ishida [12] proposed a new type of ex-situ gasification chemical looping combustion of coal. They reported that as the temperature increased from 600°C to 700°C, the CO_2 concentration profile increased by 18%, and further as the temperature and pressure increased to 3 atm and 1000°C, the CO_2 concentration profile was increased by 77.8%. Frick *et al* [13] studied mixed metal oxides for their reactivity and fluidization properties when used in chemical looping with oxygen uncoupling (CLOU). Metal oxides supported by titanium and calcium showed higher methane conversion (99%) at 1050°C. These metal oxides were also reported to have low attrition index (weight percentage of fines lost) among other samples (<1%). Zhang *et al* [14] proposed a new system for coal pyrolysis attached to a CLOU process. Simulated results showed that the proposed system could produce high CO_2 concentration (92.87%). A batch fluidization experiment was then conducted to verify the proposed new system where both semi-cokes samples reported CO_2 yield of >99.5% at 850°C, and intermediates (i.e. H_2, CO) yields of <1.5% and <0.5% at 850°C, respectively. Jiang *et al* [15] investigated the use of Ni-based oxygen carriers for hydrogen production in the reforming of glycerol chemical looping combustion system, where 90% concentration of hydrogen was achieved at 600°C, but a drop in the solid conversion (NiO to Ni) was found to be around 17% after five oxidation/reduction cycles at 550°C. Ortiz *et al* [16] studied the use of iron waste products as an oxygen carrier in the steam reforming CH_4-fueled chemical looping combustion. The highest oxygen capacity was found to be 2.4%; however, methane combustion efficiency was determined to be 90% when a solid inventory of 800 kg/MW was considered. The optimal oxygen-carrier-to-fuel ratio was also found to be 1.5. Zhou *et al* [17] assessed techno-economic aspects of a 500 MW chemical looping air separation coal-fired plant, suggesting that the air reactor could be operated at lower temperatures than the fuel reactor. The transfer of heat from the air reactor to

fuel reactor could be achieved using an additional heat source such as a solar system or CH_4 firing unit, which would in turn reduce the overall energy requirement for O_2 production.

In this study, nickel oxide supported by alumina has been chosen, proving good stability and reactivity. Nonetheless, this material is known to have some complications when used at such elevated temperatures. Indeed, one major problem is the formation of $NiAl_2O_4$, resulting from the adsorption of nickel oxide on alumina at high temperatures. This new solid phase is not desirable because of its low reactivity compared to nickel oxide, contributing to a decrease in the reactivity of the oxygen carrier. Another issue concerns the production of carbon on the surface of the particles during the reduction that is responsible for decreasing the reactivity of nickel oxide. Nickel oxide plays a catalytic role in methane decomposition to form coke when excessive amounts of methane are introduced. The complexity of the reaction mechanism on a larger scale (e.g. pilot plant) between nickel oxide as oxygen carrier and methane makes it difficult to evaluate the influence of kinetics during the reduction reaction. The same holds true for the complexity of the gas-solid multicomponent mass transfer effects. The knowledge gap identified in previous studies is a thorough investigation of the kinetics and mass transfer effects when a micro-reactor system is used for the nickel-based oxygen carriers in the CLC of methane. Therefore, this study provides a comprehensive evaluation and sensitivity analysis of the CLC process when a micro-reactor system is used in the CLC of methane to mitigate the potential problems listed above for nickel-based oxygen carriers (such as carbon deposition, formation of intermediate phase ($NiAl_2O_4$), and mass transfer effects on kinetics). Aspen Plus computer software is used simulate the whole process, so that the outcomes of this study can be used as a basis for scaling up the CLC process when a nickel-based oxygen carrier is used.

4.4. Theory

In Aspen Plus, the general chemical reaction is defined as follows:

$$r = \frac{[\text{kinetic factor}][\text{driving force}]}{[\text{adsorption expression}]} \tag{4.3}$$

The kinetic factor is expressed by:

$$k_0 * \left(\frac{T}{T_0}\right)^n * \exp\left(-\frac{E_A}{RT}\right) \tag{4.4}$$

The driving force is as follows:

$$K_1 * \Sigma {C_i}^{a_i} - K_2 * \Sigma {C_j}^{b_j} \tag{4.5}$$

The adsorption expression is:

$$(\Sigma K_i \Pi {C_i}^{\nu_i})^m \tag{4.6}$$

The K_i factors used in the driving force and the adsorption expressions represent equilibrium constants, in which K has the following expression:

$$\ln(K) = A + \frac{B}{T} + C * \ln(T) + D * T \tag{4.7}$$

where k_0 is the frequency factor ($mol^{1-n}\ g^{n-2}$/min), T is the reaction temperature (K), T_0 is the reference temperature (K), n is the temperature exponent (-), E_A is the activation energy (kJ/mol), R is the universal gas constant (J/mol K), Ki equilibrium constant (m^3/mol), Ci is the concentration (mol/m^3), a&b are two empirical parameters of Redlich-Kwong equation of state, v is the exponent of i^{th} component (-), m is the adsorption term exponent (-), and A, B, C & D are the adsorption coefficients (-).

4.5. Design criteria

In this study Aspen Plus, which is a chemical process simulation and optimization software used in many fields (polymers, fine chemistry, biochemistry, petrochemistry, etc.), is used to simulate the CLC process using two type of reactors: Gibbs reactor (minimization of Gibbs free

energy) for the oxidation reaction in the air reactor, and plug flow reactor (fuel reactor) that can be switch between RGibbs and RPlug reactors to study the thermodynamics and kinetics of the reduction reaction in the fuel reactor. In this process (Fig. 4.2), the fuel is initially mixed with the circulated oxygen carrier from the air reactor to allow the combustion of fuel to occur at the reaction temperature. The gaseous products (CO, H_2, H_2O, CO_2, and unreacted CH_4 and N_2) are then separated from the solid oxygen carriers (mixture of NiO, Ni and possibly carbon). The particles are fed to the air reactor to be oxidized (Ni to NiO). The solid phase is then split (10% moved out of the process) and later mixed with fresh NiO. The fuel is considered to be 10% methane in nitrogen, while the air is considered to be 20% O_2 and 80% N_2. The oxygen carrier 100% NiO was chosen in order to eliminate the interaction of support, which lowers the reactivity of active metal, especially during the $NiAl_2O_4$ phase that is normally formed when Al_2O_3 support is used. The input and the considered reactor geometry/operating condition of this study are shown in Table 4.1.

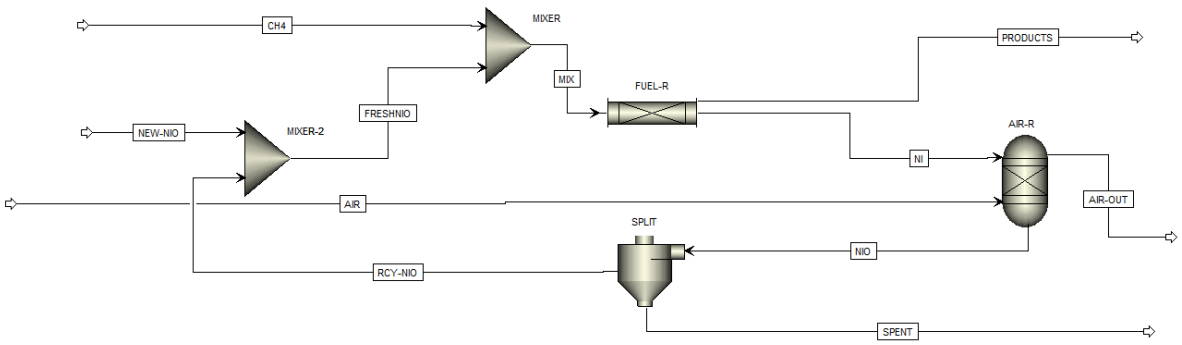

Fig. 4.2. Aspen Plus process flowsheet.

Table 4.1 Data used in the simulation

Input	Value
Fuel flow rate	$6.82 * 10^{-6}$ kmol/s
Air flow rate	$1.67 * 10^{-6}$ kmol/s
NiO flow rate	$6.82 * 10^{-6}$ kmol/s
Fuel reactor parameters	T = 700 °C, P = 30 bar L = 15 cm, D = 4 mm Catalyst loading = 300 mg Bed voidage = 0.4
Air reactor parameters	T = 830 °C, P = 30 bar Gibbs reactor (thermodynamic equilibrium)

4.6. Results and Discussion

4.6.1. *Thermodynamic analysis*

A thermodynamic equilibrium study was performed to assess the nature and behavior of the chemical components involved in the reaction inside the fuel reactor upon changing the temperature and pressure. The gas molar fraction of each gas is given by the gas moles presented during the reaction divided by the total moles:

$$y_i = \frac{n_i}{n_{CO2}+n_{H2O}+n_{CO}+n_{H2}+n_{CH4}} \quad (4.8)$$

where; y_i is the molar fraction of i^{th} gas (-), and n_i is the number of moles of i^{th} gas (mol).

The conversion of i^{th} component is given by:

$$Y_i = \frac{n_{i,R}}{n_{i,F}} \quad (4.9)$$

where; Y_i is the conversion of i^{th} component (-), $n_{i,R}$ is the number of moles of i^{th} component reacted (mol), and $n_{i,F}$ is the number of moles of i^{th} component fed to the fuel reactor (mol).

To evaluate the reduction reaction thermodynamic equilibrium, a Gibbs reactor was used to model the fuel reactor by using the Gibbs free energy minimization method, presumably the Lagrange multiplier matrices technique. The property method used for solids handling in Aspen Plus was the Peng-Robinson equation of state with Boston-Mathias modifications (PR-BM). Details about the PR-BM method can be found elsewhere [18]. The gas composition of the outlet stream was studied when the reactor temperature varied from 700°C to 1200°C. The composition of the product gas and the conversion of methane are shown in Fig. 4.3.

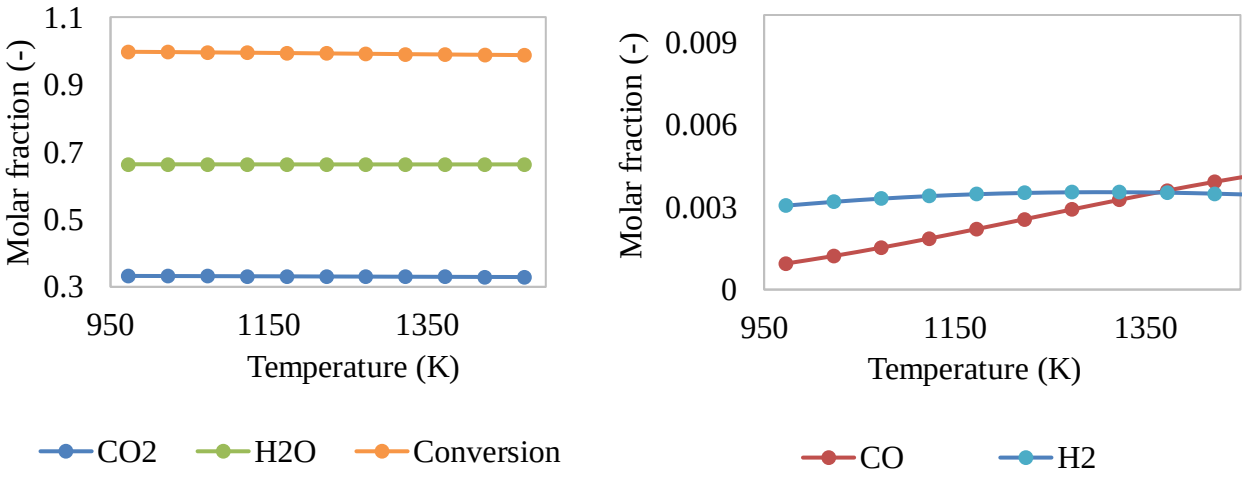

Fig. 4.3. Thermodynamic equilibrium of gaseous products.

As can be seen in Fig. 4.3, when the RGibbs reactor was used as a fuel reactor, the conversion of methane could reach up to 99.44% with a stoichiometric ratio of gaseous products (i.e. carbon dioxide and water). The equilibrium results obtained from this study were compared to the

experimental results conducted by Son *et al* [19] with a good agreement found. Further, the intermediates (carbon monoxide and hydrogen) were investigated during the reduction reaction where the minimal appearance of intermediates was noticed; however, as the reaction temperature increased (700^{o}C to 1200^{o}C), the formation of carbon monoxide and hydrogen increased too. The increase in the formation of intermediates suggested a partial combustion of methane in the RGibbs reactor occurred at elevated temperatures. This could be due to the limited supply of oxygen coming from the carriers in the fuel reactor (i.e. oxygen/methane ratio) that caused a partial combustion of methane. From a thermodynamic prospective, to avoid the partial combustion of methane in the RGibbs reactor, the operating temperature should not exceed 900^{o}C. However, the temperature in the fuel reactor should not be too low (<500^{o}C) to hinder the combustion of methane. Similar results were found elsewhere for the formation of intermediates at elevated temperatures [19].

The variation of pressure was investigated to study the effect of pressure on the thermodynamic equilibrium of the reduction reaction of the carriers. The pressure in the fuel reactor varied from 20 bar to 40 bar and the results are shown in Fig. 4.4. The combustion reaction of methane moved toward the final products (carbon dioxide and water); however, the formation of intermediates (hydrogen and carbon monoxide) was minimal. Upon varying the pressure in the fuel reactor, a diffident effect of pressure on the thermodynamics was observed. This indicates that the products from the methane combustion reaction were independent of pressure in the range of 20 bar to 40 bar. The thermodynamic conditions obtained were used for the following kinetic study.

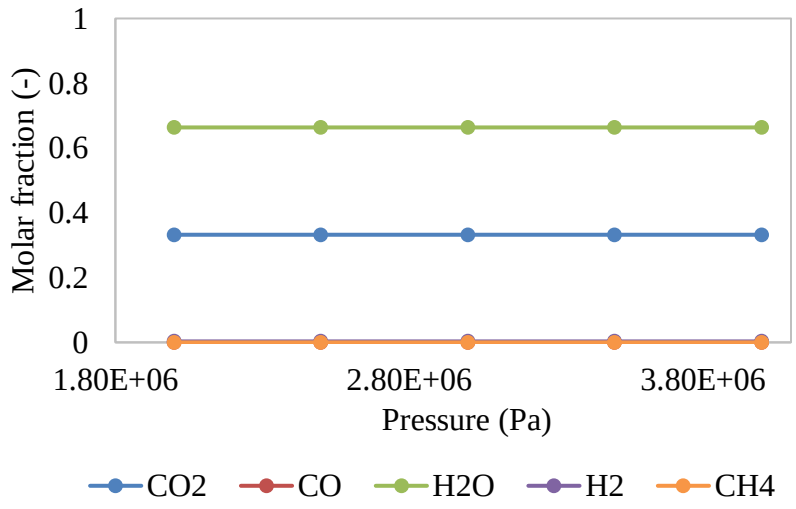

Fig. 4.4. Effect of pressure on the thermodynamic of reduction reaction.

4.6.2. *Kinetic assessment*

A study was made of the effect of reaction kinetics on the CLC fuel reactor. Two types of chemical reactions could be considered in this study: non-catalytic gas-solid reactions, and catalytic gas-gas reactions. All considered reactions were as follow [20]:

Non-catalytic gas-solid reactions:

$$CH_4 + 2NiO \rightarrow 2Ni + 2H_2 + CO_2 \quad (4.10)$$

$$CH_4 + NiO \rightarrow Ni + 2H_2 + CO \quad (4.11)$$

$$H_2 + NiO \rightarrow Ni + H_2O \quad (4.12)$$

$$CO + NiO \rightarrow Ni + CO_2 \quad (4.13)$$

Catalytic gas-gas reactions:

$$CH_4 + H_2O \rightarrow CO + 3H_2 \quad (4.14)$$

$$CH_4 + CO_2 \rightarrow 2CO + 2H_2 \quad (4.15)$$

$$CO + 3H_2 \rightarrow CH_4 + H_2O \quad (4.16)$$

$$CO + H_2O \rightarrow CO_2 + H_2 \quad (4.17)$$

$$CH_4 \rightarrow C + 2H_2 \quad (4.18)$$

$$C + CO_2 \rightarrow 2CO \quad (4.19)$$

$$C + H_2O \rightarrow CO + H_2 \quad (4.20)$$

In Aspen Plus, the Power Law (PL) model was assumed for the non-catalytic gas-solid reactions, but for the catalytic gas-gas reactions with known partial pressures of produced gases, the Langmuir-Hinshelwood-Hougen-Watson (LHHW) model was used. The tolerance value of iterations was adjusted several times to obtain consistent results. The concentration profile along the fuel reactor length is shown in Fig. 4.5. A complete conversion from methane to carbon dioxide and water with no intermediates was obtained using the non-catalytic gas-solid reaction. The exiting stream consisted of only 67% water and 33% of carbon dioxide. The entering and exiting streams composition of the fuel reactor are shown in Table 4.2.

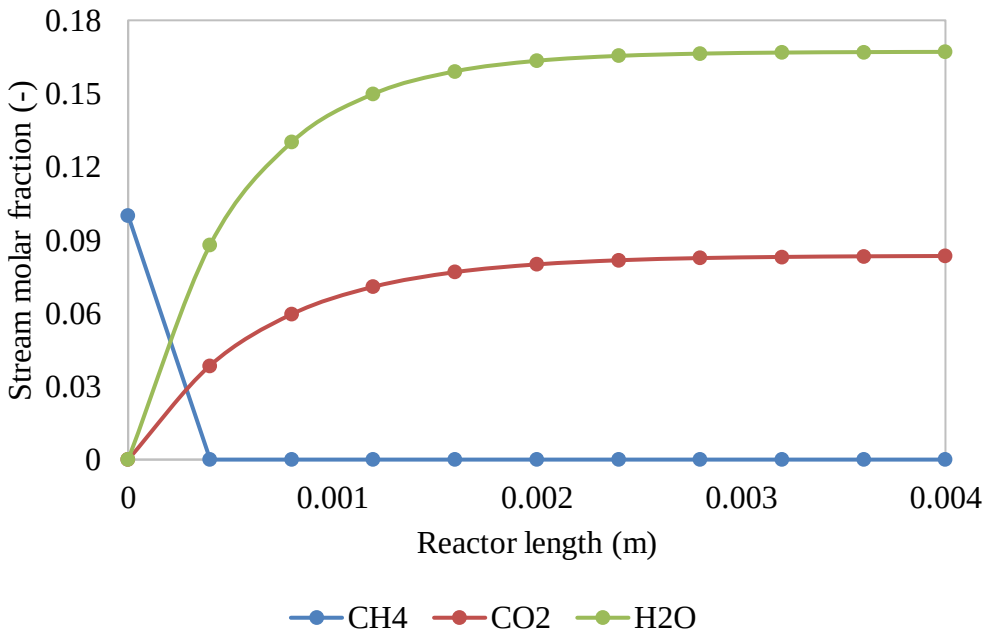

Fig. 4.5. Concentration profile across the fuel reactor length.

Table 4.2 Streams composition of fuel and air reactor

Fuel Reactor			
Component	Gas Fraction	Solid fraction	Product Fraction
CH_4	0.1	0	0
CO_2	0	0	0.0833
H_2O	0	0	0.1673
N_2	0.9	0	0.7494
NiO	1	0.9590	0
Ni	0	0.0410	0
Air Reactor			
O_2	0.2	0	0.1285
N_2	0.8	0	0.8716
NiO	0.9589	1	0
Ni	0.0410	0	0

4.6.3. *Sensitivity analysis and the effect of operating conditions*

A set of sensitivity analyses were conducted to investigate the effects of temperature and pressure on the exiting product stream. As the temperature and pressure increased from 500°C to 1000°C, and from 20 bar to 40 bar respectively, no significant effects were noticed on the molar fraction of both CO_2 and H_2O. Further, the variation in the reactor length and residence time showed no significant effect on the composition of final products. Methane decomposition is more likely to occur after the reduction reaction of NiO to Ni [21]. Therefore, another set of reactions (rxns: (18) to (20)) was added to the system concerning formation of carbon due either to methane

decomposition and/or Boudouard reaction, and the removal of carbon due to steam gasification reaction [8].

$CH_4 \rightarrow C + 2H_2$ methane decomposition (4.18)

$2CO \rightarrow C + CO_2$ Boudouard reaction (4.19)

$C + H_2O \rightarrow CO + H_2$ steam gasification (4.20)

It was noticed that the added reactions were considerably slower than the ones in the first set of reactions (rxns: (10) to (17)). The reason for reactions (18) to (20) having no significant effect could be the fact that methane decomposition reaction is favored at high temperature (higher than 600°C) whereas the Boudouard reaction is favored at lower temperature (400°C) [22]. Also, the formation of carbon usually occurs when there is no a sufficient amount of steam in the fuel reactor.

4.6.3.1. Effect of inlet molar flow rate on the methane conversion

The effect of molar flow rate of methane and the carrier gas entering the fuel reactor on the conversion of methane was studied, and the results are shown in Fig. 4.6. Methane conversion decreased from 100% to nearly 50% as the flow rate was increased from 1×10^{-9} kmol/s to 100 kmol/. However, the steam concentration in the exiting stream increased to 100% as the entering molar flow rate increased, while the carbon dioxide concentration decreased. It is worth considering that after a certain flow rate the residence time dropped drastically, causing the final trends in conversion and gas composition. The formation of intermediate (H_2) was greater than the other intermediate (CO), which could be the reason for the increases in steam concentration. The optimal flow rates for methane and the carrier of this study were determined to be less than 0.1 kmol/s to maintain a methane conversion of 50% or higher. Flowrates of $1E^{-6}$ to $1E^{-3}$ are favorable for chemical looping reforming (CLR) and hydrogen production; that is, however, outside the scope of this study.

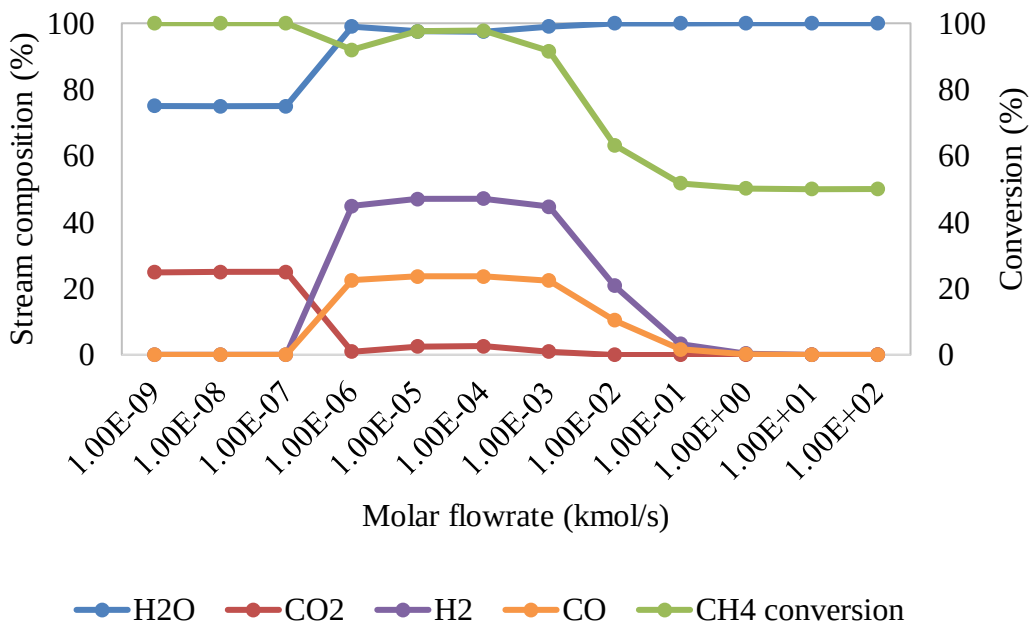

Fig. 4.6. Effect of molar flow rate on the conversion of methane.

4.6.3.2. Effect of methane concentration on the conversion of carrier

The effect of different methane dilutions in nitrogen was studied and is shown in Fig. 4.7. Complete conversion from NiO to Ni was observed when the methane concentration increased from 30% (balanced with N_2) to 100% of methane. This means an incomplete or partial conversion of methane could be anticipated when the methane concentration goes below 30%. As the methane concentration increased, the formation of final products (i.e. H_2O and CO_2) decreased, but the formation of intermediates (H_2 and CO) increased. This means that at higher methane concentration, the NiO limited and thus complete conversion could be anticipated. However, the presence of Ni and steam in the fuel reactor after the combustion of methane enhanced the formation of both H_2 and CO intermediates. These catalytic effects of Ni dictate that higher concentrations of methane result in a CLR rather than CLC.

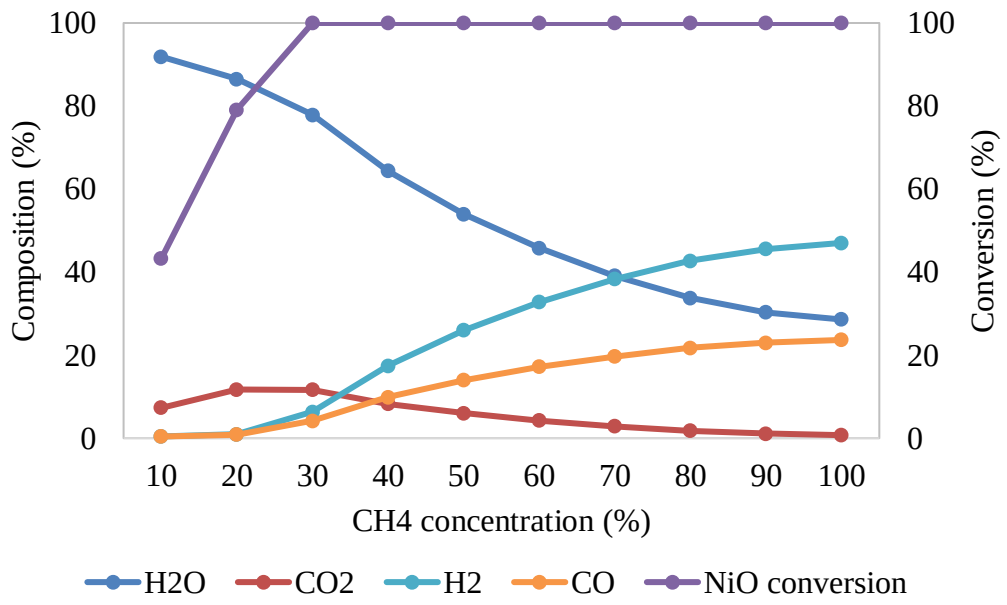

Fig. 4.7. Effect of different methane concentration on the conversion of carrier.

4.6.4. *Data validation*

To validate whether mass transfer existed in the fuel reactor of this study, the experimental conversion at a different methane concentration (balanced with N_2) was compared to the conversion when intrinsic and global kinetics were assumed in the literature [23]. The results are shown in Fig. 8. It can be seen that the increases in the methane concentration did not have a significant effect on the conversion of the global kinetic reported in the literature; however, the reported conversion of intrinsic kinetic increased as the methane concentration increased. Therefore, by comparing the conversion obtained from this study, it can be seen that the Aspen Plus conversion followed the conversion of intrinsic kinetics. This indicated that no significant mass transfer effect existed in this study when the methane concentration varied from 10% to 40% (balanced with N_2).

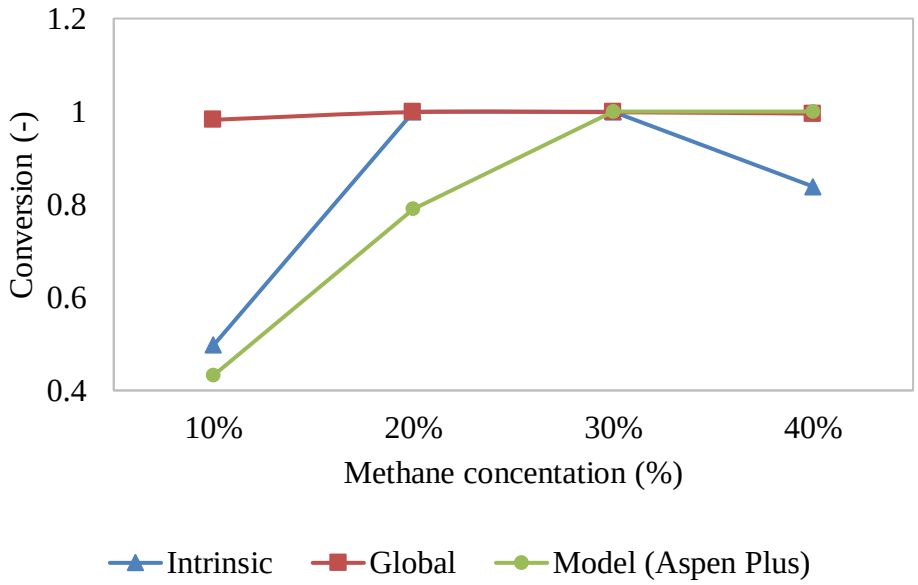

Fig. 4.8. Comparison of conversion between intrinsic [23], global [23] and Aspen Plus power law models.

The thermodynamic results obtained from this study (Fig. 4.3) were compared to the ones reported in literature [20], where the effect of temperature on the thermodynamic equilibrium of the produced gases is shown in Fig. 4.9. As the temperature increased (700^{o}C-1200^{o}C) formation of intermediates such as CO and H_2 increased. This increasing trend agreed with the reported results in literature.

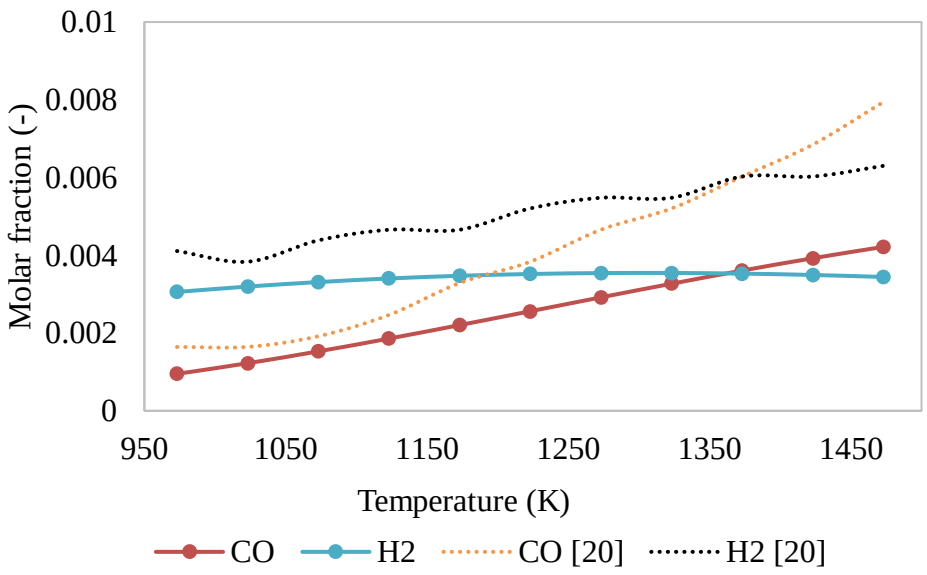

Fig. 4.9. Comparison of produced intermediates (CO, H_2) between this study and reported data in [20].

4.7. Conclusion

Aspen Plus computer software was used to provide a comprehensive evaluation and sensitivity analysis of the methane chemical looping combustion process using nickel oxide supported by alumina. A micro-reactor system was considered in the CLC of methane to carefully study the effect of different limitations such as formation of carbon, formation of nickel alumina spinel, and mass transfer on the conversions of methane and carrier. The results showed that when the temperature varied from 700°C to 1200°C, and by using the RGibbs reactor as a fuel reactor the maximum conversion of methane was predicted to be 99.44%, the formation of carbon monoxide and hydrogen increased too. The variation of pressure in the fuel reactor (20 bar to 40 bar) favored a complete conversion of methane to carbon dioxide and water; however, the formation of intermediates was minimal. Several non-catalytic gas-solid and catalytic gas-gas reactions were identified in the Aspen Plus computer software and assessed. The main outcomes

were a complete conversion from methane to carbon dioxide and water, while no intermediates were obtained using the non-catalytic gas-solid reaction. Moreover, the conversion of methane decreased from 100% to almost 50% as the entering molar flow rate increased from 1×10^{-4} kmol/s to 1 kmol/s because of a decreased residence time within the reactor. Incomplete or partial conversion of methane was anticipated when the methane concentration fell below 30%, but a complete conversion of the carrier (NiO to Ni) was anticipated when the methane concentration went above 40%. A comparison between the reported experimental conversion in the literature and the conversion obtained in this study suggested that no significant mass transfer effect on the kinetics was observed.

4.8. Acknowledgements

The authors acknowledge the financial support received from the Natural Sciences and Engineering Research Council (NSERC) of Canada ─ Industrial Research Chairs (IRC) program, Canadian Natural Resources Limited (CNRL), and Devon Energy Corporation Canada. The authors would also like to acknowledge the Ministry of Education (MOE) in the Kingdom of Saudi Arabia. The authors greatly appreciate the contribution of Ms. Mélanie Roux and Ms. Marion Vaussy in the modelling work of this study.

4.9. References

[1] J. Leggett,W. J. Pepper, R. J. Swart, J. Edmonds, L. G. Meira Filho, I. Mintzer, I., M. X. Wang, Emissions scenarios for the IPCC: an update. Climate change, (1992) 69-95.

[2] J. L. Míguez, J. Porteiro, R. Pérez-Orozco, D. Patiño, S. Rodríguez, Evolution of CO_2 capture technology between 2007 and 2017 through the study of patent activity, Appl. Energy, 211 (2018) 1282-1296.

[3] D. Y. Leung, G. Caramanna, M. M. Maroto-Valer, An overview of current status of carbon dioxide capture and storage technologies, Renewable Sustainable Energy Rev. 39 (2014) 426-443.

[4] P. Luis, Use of monoethanolamine (MEA) for CO_2 capture in a global scenario: Consequences and alternatives, Desalin. 380 (2016) 93-99.

[5] A. Sanna, F. Vega, B. Navarrete, M. M. Maroto-Valer, Accelerated MEA degradation study in hybrid CO_2 capture systems, Energy Procedia. 63 (2014) 745-749.

[6] R. Porrazzo, G. White, R. Ocone, Aspen Plus simulations of fluidised beds for chemical looping combustion, Fuel. 136 (2014) 46-56.

[7] M. Gupta, I. Coyle, K. Thambimuthu, CO_2 capture technologies and opportunities in Canada. In 1st Canadian CC&S Technology Roadmap Workshop 18 (2003) pp 19.

[8] J. Adanez, A. Abad, F. Garcia-Labiano, P. Gayan, F. Luis, Progress in chemical-looping combustion and reforming technologies, Prog. Energy Combust. Sci. 38-2 (2012) 215-282.

[9] M. M. Hossain, H. I. de Lasa, Chemical-looping combustion (CLC) for inherent CO_2 separations—a review, Chem. Eng. Sci. 63-18 (2008) 4433-4451.

[10] A. Abad, J. Adánez, F. García-Labiano, L. F. de Diego, P. Gayán, Modeling of the chemical-looping combustion of methane using a Cu-based oxygen-carrier, Combust. Flame. (2010) 602–615.

[11] I. A. Bakare, S. A. Mohamed, S. Al-Ghamdi, S. A. Razzak, M. M. Hossain, H. I. de Lasa, Fluidized bed ODH of ethane to ethylene over VOx–MoOx/c-Al_2O_3 catalyst: Desorption kinetics and catalytic activity, Chem. Eng. J. (2015) 207–216.

[12] H. Jin, M. Ishida, A new type of coal gas fueled chemical-looping combustion, Fuel. (2004) 2411-2417.

[13] V. Frick, M. Ryden, H. Leion, T. Mattisson, A. Lyngfelt, Screening of supported and unsupported Mn-Si oxygen carriers for CLOU (chemical-looping with oxygen uncoupling), Energy. (2015) 544.554.

[14] Y. Zhang, B. Jin, X. Zou, H. Zhao, A clean coal utilization technology based on coal pyrolysis and chemical looping with oxygen uncoupling: Principle and experimental validation, Energy. (2016) 181-189.

[15] B. Jiang, B. Dou, Y. Song, C. Zhang, B. Du, H. Chen, C. Wang, Y. Xu, Hydrogen production from chemical looping steam reforming of glycerol by Ni-based oxygen carrier in a fixed-bed reactor, Chem. Eng. J. (2015) 459-467.

[16] M. Ortiz, P. Gayán, L. F. de Diego, F. García-Labiano, A. Abad, M. A. Pans, J. Adánez, Hydrogen production with CO_2 capture by coupling steam reforming of methane and chemical-looping combustion: Use of an iron-based waste product as oxygen carrier burning a PSA tail gas, J. Power Sources. (2011) 4370-4381.

[17] C. Zhou, K. Shah, H. Song, J. Zanganeh, E. Doroodchi, B. Moghtaderi, Integration Options and Economic Analysis of an Integrated Chemical Looping Air Separation Process for Oxy-

fuel Combustion, Energy Fuels. (2015) 1741-1755.

[18] J. F. Boston, P. M. Mathias, Phase Equilibria in a Third Generation Process Simulation, 2nd International Conference on Phase Equilibria and Fluid Properties in the Chemical Process Industries, Berlin (West). (1980) 17-21.

[19] S. R. Son, S. D. Kim, Chemical-looping combustion with NiO and Fe_2O_3 in a thermobalance and circulating fluidized bed reactor with double loops, Ind. Eng. Chem. Res. 45-8 (2006) 2689-2696.

[20] I. Iliuta, R. Tahoces, G. S. Patience, S. Rifflart, F. Luck, Chemical-looping combustion process: Kinetics and mathematical modeling, AIChE. 56-4 (2010) 1063-1079.

[21] M. M. Tijani, A. Aqsha, N. Yu, N. Mahinpey, Determination of redox pathways of supported bimetallic oxygen carriers in a methane fuelled chemical looping combustion system, Fuel. 233 (2018) 133-145.

[22] P. Cho, T. Mattisson, A. Lyngfelt, Carbon formation on nickel and iron oxide-containing oxygen carriers for chemical-looping combustion, Ind. Eng. Chem. Res. 44-4 (2005) 668-676.

[23] M. M. Tijani, A. Aqsha, N. Mahinpey, Synthesis and study of metal-based oxygen carriers (Cu, Co, Fe, Ni) and their interaction with supported metal oxides (Al_2O_3, CeO_2, TiO_2, ZrO_2) in a chemical looping combustion system, Energy. 138 (2017) 873-882.

CHAPTER FIVE: Reactivity assessment of a 50 MW methane-fueled chemical looping combustion process using a bimetallic (Ni-Cu) oxygen carrier

International Journal of Greenhouse Gas Control. To Be Submitted (2018)

5.1. Presentation of the article

This chapter presents an article that investigates a pilot plant for the methane CLC process using bimetallic carriers (Ni-Cu) supported with zirconia. The article examines a case study that involved producing 50 MW of power, considering all units needed in a real-case scenario, such as air and fuel reactors unit, power generation units, heating and pressure changing units. The design of reactors and hydrodynamics were calculated using the most reliable formulas in literature as a starting point to construct the process flowsheet in Aspen Plus computer software. The results showed that decreases in the conversion of both reactors (air and fuel reactors) anticipated when the entering molar flows increased. A slight dependency of loading percentage on the conversion of methane was found in the fuel reactor, but a 39% increase in conversion was observed in the air reactor. The CLC process to produce 50 MW of power in this study was compared to two other processes described in the literature, and it was found that the CLC process was more efficient than these other processes.

The work of this article was performed by Tijani, M. M. Dr. Siegler, H. provided assistance, guidance, and co-supervision. Prof. Mahinpey, N. supervised and refined the outcome of this work.

Reactivity assessment of a 50 MW methane-fueled chemical looping combustion process using a bimetallic (Ni-Cu) oxygen carrier

This article will be submitted to the International Journal of Greenhouse Gas Control Journal in 2018

Mansour Mohammedramadan Tijani, Hector De la Hoz Siegler, Nader Mahinpey

Department of Chemical and Petroleum Engineering, Schulich School of Engineering, University of Calgary, Calgary, AB, T2N 1N4, Canada

5.2. Abstract

A well-known global issue is the emission of green-house gases (GHGs), which has the potential to result in irreversible and disastrous damage at a global scale. The emission portion of carbon dioxide (CO_2) is one of the highest (~64.3%) among the GHGs. Carbon capture is a key technology to reduce CO_2 emissions to the atmosphere. The chemical looping combustion (CLC) process produces a concentrated stream of CO_2 through the indirect combustion of fuel with oxygen. At complete combustion, water and CO_2 are separated by condensation. Hence, the produced CO_2 can be compressed or transported to storage or utilization. In this study, a case study to produce 50 MW of power was investigated in terms of the reactivity achieved and its economic efficiency. The cross-sectional area of both fuel and air reactors was estimated to be 11.50 m^2 (diameter = 3.83 m). The solids holdup was estimated to be 17.58 tonnes and 5.86 tonnes in the fuel and air reactors, respectively. The pilot plant process simulation in Aspen Plus revealed that minimal effect of temperature (700 K to 1100 K) was observed on the conversion of reduction reaction. Moreover, as the temperature and bimetallic precursor's loading percentage increased, the degree of oxidation increased. Both air and fuel reactors produced heat due to exothermic oxidation and reduction reactions; however, the net power produced from the air reactor unit was

38.73% greater than that in the fuel reactor unit. The efficiency of the studied case was found to be higher than both the IGCC and PC power plants.

5.3. Introduction

Carbon dioxide emission to the atmosphere is considered a major contributor to climate change. Reduction of carbon dioxide emissions can be achieved through carbon capture technology. In power plants, capturing carbon dioxide is performed either through pre-combustion or post-combustion CO_2-capture technologies. The oxy-fuel combustion of fuel produces a highly concentrated stream of CO_2 that does not require any further expensive capturing units. Unlike pre-combustion and post-combustion technologies, oxy-fuel combustion is still an industrially immature technology due to major challenges related to sustainability and the affordability of pure oxygen during the combustion step. To overcome these challenges, numerous studies have been conducted specifically in chemical looping combustion (CLC), as a promising new oxy-fuel technology, in order to come up with a sustainable oxygen supply through multicycles of fuel combustion. However, the capital cost and amount of solid inventories needed in the reactor system are the main obstacles to commercializing this technology.

Oxygen carriers are solid materials used in the CLC process to provide the oxygen needed for the combustion process. These materials are usually metals that have an affinity to be oxidized when exposed to air in the air reactor (AR) and reduced when exposed to fuel in the fuel reactor (FR). Both AR and FR are connected in a loop, which is called the reactor system of the CLC process. Oxygen carriers provide either stoichiometric or non-stoichiometric oxygen to indirectly combust fuel to produce heat and then power. Transition metals such as Mn, Fe and Co have been studied for their capability to be used in CLC processes as they exhibit different oxidation states, thus possibly carrying more oxygen.

An assessment of the Ni/Al_2O_3 oxygen carrier was conducted on a biomass and co-fueled gasification CLC where it was found that energy efficiency reached 60.16% in summer and 57.46% in winter at the optimum oxygen-to-carbon ratio of 0.42 [1]. A non-isothermal changing grain size model was implemented for the redox reaction in both AR and FR, where it was found that temperature inside the particles was dependent on particle size, reaction time and gas film heat transfer; however, the temperature inside the particles was not dependent on either porosity, activation energy, or type of supports [2]. The particle size of oxygen carriers plays an important role in the FBR-CLC system. Jun and Gamwo [3] found that a low fuel conversion rate observed in a multiphase CFD-based model was due primarily to the fast and large rising bubbles in the bed, and also that a nano-size oxygen carriers' particle could increase the fuel conversion rate. The activation energy of the reduction reaction for the CLC of methane in a fixed-bed reactor was reported by Iliuta *et al* [4] as 23.6 kJ/mol (partial oxidation to CO) and 77.4 kJ/mol (reduction of CH_4 to CO_2 and H_2), which means methane combustion took place to produce H_2 and CO in a two-step reaction while another reaction took place to produce CO_2 and H_2 without forming CO. Experimental investigation of the active-site loading percentage in both oxidation and reduction reactions of Ni/bentonite was concluded with an optimum loading percentage of 57.8% (among 26.0% to 78.4%) and temperature of 750°C or 800 °C (between 650°C and 900°C) for the reduction reaction. Where the oxidation reaction rate as the loading percentage (21.6% to 74.0%) and temperature (850°C to 1000°C) increased, the rate increased as well [5]. Porrazzo *et al* [6] investigated optimization of the solid inventories in the CLC reactor system to produce 10 kWth by using two approaches: 2D-CFD and Aspen Plus computer software at two different kinetics levels (k_i = 0.71 and 0.1, high and low, respectively). It was found that decreasing the entering superficial gas velocity of fuel led to a decrease in the mass fraction of fuel and an increase in the

gas conversion level for both models. Wang *et al* [7] implemented the cluster structure dependent (CSD) drag coefficient model into the CFD calculations of the CLC AR as a multi-scale chemical reaction model to address the effects of clusters on the chemical reaction. It was found that the chemical reaction was more influential than the mass transfer in the AR, especially when the air/fuel ratio increased from 0.85 to 1.05, resulting in an around 16% decrease in the error between the experiment and simulations [7].

The design and operation of the reactor system in CLC need to be determined and optimized in order to improve the whole CLC process. Different reactor systems have been proposed in the literature such as rotary, fixed, fluidized-bed reactors. A 2% increase in the optimal performance of the rotary reactor system was obtained when both AR and FR were maintained at a thermal equilibrium [8]. Modelling the CLC reactor system as series of both/either CSTRs and PFRs was common before the introduction of FBR in Aspen Plus. Dense and lean phases in the AR were modelled by Porrazzo *et al* [9] who found that -693.8 kW total heat duty was needed for combustion of methane at the optimum air-to-fuel ratio of 1.25 and 3.5 m height of the AR. Interconnected AR as CFB and two-stage FR as bubbling fluidized-bed (BFB) reactors for CLC process were simulated in the Dyssol computer software by Haus *et al* [10] to validate simulation with experiments. Within an error range of 5-10%, steady state was reached in 20s and as the fluidization velocity increased in the FR, oxygen carriers were found more in the AR. Hartge *et al* [11] conducted an experiment on the role of mixing in the performance of circulating fluidized-bed (CFB) reactors, choosing a semi-empirical 3-D combustion approach. The pressure drop in the CFB was found to be 6 kPa, where the role of gas and solid mixing in CFB reactors was important and the reactivity of solid reactants could be increased by a factor of 10. Jafari *et al* [12] developed a hydrodynamic model for the simulation of fluidized-bed reactors by the sequential

modular approach to simulate the non-ideality, where a good agreement between experiments and the proposed model was found. Also, prediction of real performance with different entering superficial gas velocities and Geldart A&B type of particles was accomplished when the proposed model implemented. The multistage RPLUG CLC reactor system in Aspen Plus was investigated by Meng *et al* [13] to increase char conversion. Char was converted into syngas at the optimum volume of ½ for the two-stage and ¼ for the four-stage of the single-stage volume and as the optimum reactor volumes increased, an insignificant increase in the energy output was reported. A cyclone is usually attached to the existing AR stream to separate the oxidized oxygen carriers from depleted air. A proposed design for a cyclone was presented by Puettmann [14], where a 0.02 bar pressure drop, diameter of 1 m, height of 3.1 m, and a vortex finder diameter of 0.41 m were considered. The solid mass flow rate in the cyclone was then reported to be reduced up to 99.94%.

Some researchers have undertaken energy and exergy analyses of a methane CLC power plant in terms of key operation variables. Hassan *et al* [15] reported that Ni-based oxygen carriers, fuel and air flow rates, pressure, waste heat recovered and the fraction of inactive inert in the oxygen carriers affected the energy and exergy; however, a 6-8% gain in efficiency compared to conventional CO_2 capture technology was achieved, where the maximum proposed power plant thermal efficiency was found to be between 50 and 52%. Optimum operating conditions for coal CLC process were estimated by Ohlemüller *et al* [16] in a 100 kW_{th} pilot plant, where the total demand of oxygen carriers was reduced by up to 19.7% at the optimum operating condition of 0.23 bar pressure drop, 977 °C temperature, 1800 kg/h circulating mass flow, 37.5 kg/h steam flow, and 100% separation efficiency of the FR cyclone. Early attempts to simulate the CFBR in Aspen Plus were made in 1998 when Sotudeh-Gharebaagh *et al* [17] studied the combustion of coal with the flowsheet divided into three sub-flowsheets: lower, upper and sep-flowsheets. Good

agreement of the proposed model with the other 13 different sets of operating conditions for a 0.8 MWth CFBR pilot plant was found with less than 3% of uncertainty for coal combustion efficiency. Energy generation at a pre-commercial scale of 100 MWth methane-fuel CLC process was performed by Peltola *et al* [18] to scale up this process, with a 42.8% efficiency achieved without CO_2 purification and compression at a methane conversion of 99%. Wang and Fu [19] conducted thermodynamic analyses of a solar-hybrid trigeneration system integrated with methane CLC, using Aspen Plus with an assumed direct constant solar radiation of 1000 W/m^2; overall system energy and exergy efficiencies were found to be 7% and 4% respectively, higher than conventional trigeneration systems. Also, the solar share was around 32% where the net SCLC-to-exergy efficiency and the saving rate of solar collection area could reach 24% and 63%, respectively.

Previous studies on the reactivity and economic assessment of monometallic oxygen carriers have shown some challenges related to inventories cost of oxygen carriers and the high loading percentage (>40%) needed to achieve around 40% overall process efficiency. Use of supported bimetallic oxygen carriers in the CLC process has been experimentally demonstrated where the addition of a second precursor could lower the activation energy. Also, some oxygen carriers have shown low oxygen capacity but high thermal stability such (e.g. iron), while others have shown relatively high oxygen capacity, but tend to sinter at high temperatures or deposit carbon, which decreases their reactivity in a long cyclic operation. Hence, there is a need to study supported bimetallic transition metals oxygen carriers using different precursor-combinations to come up with the optimum precursor-combination while maintaining high chemical and thermal stabilities. Thus, the aim of this study is to investigate, and simulate the use of a supported bimetallic oxygen carrier (Ni-Cu/ZrO_2) in the methane-fueled chemical looping combustion process to produce 50

MW of power in a pilot plant. This investigation addresses the techno-economic assessment and effectiveness of using the Ni-Cu/ZrO_2 carrier when considering both chemical stability (e.g. redox reaction rates, deactivation rate) and thermal stability (e.g. attrition index, power production). The outcomes of this study will be beneficial in the power generation field by determining the overall feasibility of the methane-fueled chemical looping combustion process when bimetallic oxygen carriers are used.

5.4. Theoretical Approach

5.4.1. Hydrodynamics: Air Reactor (AR) and Fuel Reactor (FR)

The bed voidage (ε_{mf}) at minimum fluidization velocity in both AR and FR is estimated using the Wen and Yu correlation, as follows [20]:

$$\varepsilon_{mf} = (0.071/\Psi)^{1/3} \tag{5.1}$$

where; Ψ is solid particle sphericity (-).

The minimum fluidization velocity in both AR and FR is calculated [21]:

$$u_{mf} = \frac{(\Psi d_p)^2}{150\mu}\left(g(\rho_s - \rho_g)\right)\frac{\varepsilon_{mf}^3}{1-\varepsilon_{mf}} \tag{5.2}$$

where; d_p: oxygen carriers' particle diameter (m), μ: dynamic viscosity of fluidizing fluid (kg/m.s), g: gravity acceleration (m/s^2), ρ_s: density of solid oxygen carrier (kg/m^3), and ρ_g: density of fluidizing fluid (kg/m^3).

To estimate the range of the operating velocity (i.e. pneumatic/bubbling bed) in both reactors, the terminal velocity in both reactors needs to be determined. The relationships that express terminal velocity as a dependent of Reynold's number are [21]:

$$\begin{cases} \mathrm{Re} < 0.4 & u_t = g\left(\rho_s - \rho_g\right) d_p^2 / 18\mu \\ 0.4 < \mathrm{Re} < 500 & u_t = \left(\frac{1.78 \times 10^{-2} \left(g\left(\rho_s - \rho_g\right) \right)^2}{\mu\, \rho_g} \right)^{1/3} d_p \end{cases} \tag{5.3}$$

Computer software POLYMATH v6.0 is used to solve the above nonlinear equation.

The mass flows of *Air* in AR and *Fuel* in FR are obtained as follows [22]:

$$\dot{m}_{air} = \frac{\dot{m}_o\, \lambda}{0.233} \tag{5.4}$$

$$\dot{m}_o = M_{O_2} \frac{\dot{m}_{fuel}}{M_{fuel}} S_r \tag{5.5}$$

$$\lambda = \frac{0.21\left(1 - x_{O_{2,ex}}\right)}{0.21 - x_{O_{2,ex}}} \tag{5.6}$$

$$\dot{m}_{fuel} = P_{fuel} / H_i \tag{5.7}$$

where; $\dot{m}_{air}$: mass flow rate of air in AR (kg/s), $\dot{m}_o$: oxygen mass flow rate (kg/s), λ: air ratio in AR (-), M_{O_2}: molar mass of oxygen (kg/kmol), $\dot{m}_{fuel}$: mass flow rate of fuel in FR (kg/s), S_r: stoichiometric ratio of oxygen to fuel (-), M_{fuel}: molar mass of fuel (kg/kmol), $x_{O_{2,ex}}$: existing volume fraction of oxygen in air leaving AR (-), P_{fuel}: fuel power (W), and H_i: fuel heating value (J/kg).

The cross-sectional area of AR and FR was calculated using the following expressions [22]:

$$A_{i,AF} = \frac{\dot{m}_{air}\, v_{a,air}\, T_{AR}}{u_{iAR}\, T_a} \tag{5.8}$$

$$A_{i,FR} = \frac{\dot{m}_{fuel}\, v_{a,fuel}\, R_r\, T_{FR}}{u_{i,FR}\, T_a} \tag{5.9}$$

where; $A_{i,AR}$: cross-sectional area of AR *i* donates to cross-sectional area at different velocity (i.e. mf, t or 0), $v_{a,air}$: specific volume of air at ambient temperature (m^3/kg), T_{AR}: operating temperature of AR (K), u_{iAR}: AR gas velocity *i* donates to different velocity (i.e. mf, t or 0), T_a:

ambient temperature (K), $A_{i,FR}$: cross-sectional area of FR *i* donates to cross-sectional area at different velocity, $v_{a,fuel}$: specific volume of fuel at ambient temperature (m^3/kg), R_r: recirculation ratio of total gas fed to FR and fuel flow, T_{FR}: operating temperature of AR (K), and $u_{i,FR}$: FR gas velocity *i* donates to different velocity.

The entering gas superficial velocity (m/s) in both AR and FR was then estimated using Eqns. (5.8) and (5.9). The solid inventory W_k (kg) was obtained using the following formula [22]:

$$W_k = \frac{\Delta P_k \, A_k}{g} \tag{5.10}$$

where; ΔP_k and ΔP_k: pressure drop across the reactor k subscript refers to either AR or FR (Pa = kg m^{-1} s^{-2}), and g: gravitational acceleration (m/s^2).

The bed voidage $\varepsilon_{0,k}$ (-) at the operating velocity $u_{0,k}$(m/s) was calculated using Eq. (5.2) where u_{mf} and ε_{mf} were replaced with $u_{0,k}$ and $\varepsilon_{0,k}$.

Finally, the bed height h_k (m) was calculated using [21]:

$$h_k = \frac{W_k}{\rho \, A_k \, (1-\varepsilon_{0,k})} \tag{5.11}$$

5.4.2. Reactions and kinetics

The kinetic power law model was considered in the evaluation of both oxidation and reduction reactions. The kinetic parameters of the oxidation and reduction reactions were adopted from [23]. A model that was based on the equilibrium was considered for the formation of carbon because the formation of carbon on oxygen-free carriers started occurring at high temperature (>850°C). The oxidation and reduction reactions as well as kinetic parameters were:

- Oxidation reaction:

$$Ni\text{-}Cu/ZrO_2 + O_2 \rightarrow NiO\text{-}CuO/ZrO_2 \tag{5.12}$$

$$\text{Kinetics: } k_0 = 60.64\ (1/\text{min}), E_o = 37.83\ \text{kJ/mol},\ n = 1$$

- Reduction reaction:

$$2NiO\text{-}CuO/ZrO_2 + CH_4 \rightarrow 2Ni\text{-}Cu/ZrO_2 + CO_2 + 2H_2O \quad (5.13)$$

Kinetics: $k_0 = 16.30\ (1/\text{min}), E_o = 23.71\ \text{kJ/mol},\ n = 1$

$$CH_4 \xleftrightarrow{Ni-Cu/ZrO2} C + 2H_2 \quad (5.14)$$

5.5. Design and simulation criteria

The reactor system used in this study consisted of two interconnected fluidized-bed reactors. The air reactor (AR) was operated as circulating fluidized-bed reactor, and the fuel reactor (FR) as bubbling fluidized-bed reactor. The transfer of solid carriers from the AR to FR was assumed to be by the entering superficial gas velocity of the carrier/oxidative gas, where the transfer of solid carriers from the FR to AR was assumed to be by gravity. Therefore, no equipment to transfer solid carriers between the two reactors was needed in the simulation study. A summary of the physical/process values used to estimate the hydrodynamic parameters in both AR and FR is shown in Table 5.1, while summary of hydrodynamics and sizing of reactors is shown in Table 5.2.

5.6. Process Flowsheet

The process flowsheet of this study is shown in Fig. 5.1. The process flowsheet consisted of two main units: AR unit and FR unit. The AR unit oxidized the carriers to produce heat that was later used to produce power (AR power generation unit). This power generation unit consisted of two countercurrent heat exchangers and two high-pressure (100 bar) steam turbines. A similar system was constructed in Aspen Plus for the FR unit, but the FR power generation unit consisted of five high-pressure steam turbines. There was also a condenser attached to the exiting stream of the FR unit to separate the produced carbon dioxide from water.

Table 5.1 Physical and process values estimated or assumed

Parameter: Symbol (unit) \ Reactor	AR	FR
Particles shape factor: Ψ (-)	1	1
Viscosity of gas: μ_g (cP)	0.0182	0.0110
Density of gas: ρ_g (kg/m^3)	1.2050	0.6560
Gravitational acceleration: g (m/s^2)	9.81	9.81
Density of carrier: ρ_c (kg/m^3)	4966	4966
Diameter of particle: d_p (m)	0.001	0.001
Specific volume: v (m^3/kg)	0.8299	1.5244
Reactor temperature: T (K)	1327	990
Ambient temperature: T_a (K)	298	298
Stoichiometric ratio: S_r (-)	2	---
Recirculation ratio: R_r (-)	---	1
Molar fraction of existing oxygen: $x_{O_{2,ext}}$(-)	0.0460	---
Power: P (MW)	---	50
Lower heating value: H_i (MJ/kg)	---	50
Inlet pressure: P_{inlet} (bar)	1	1
Pressure drop: ΔP (kPa)	5	15
Molar mass of oxygen: M_{O2} (kg/kmol)	32	---
Molar mass of air: M_{air} (kg/kmol)	29	---
Molar mass of fuel: M_{Fuel} (kg/kmol)	---	16

Table 5.2 Hydrodynamic parameters and size of AR and FR reactors

Parameter	AR	FR
Minimum fluidization velocity: U_{mf} (m/s)	2.16	3.58
Terminal velocity: U_t (m/s)	17.71	18.02
Reactor cross-sectional area: A (m^2)	11.50	11.50
Entering superficial gas velocity: U_0 (m/s)	71.02	5.96*
Bed mass: W_k (ton)	5.86	17.58
Reactor diameter: D (m)	3.83	3.83

* increases by a stoichiometric factor of 3 after the reaction

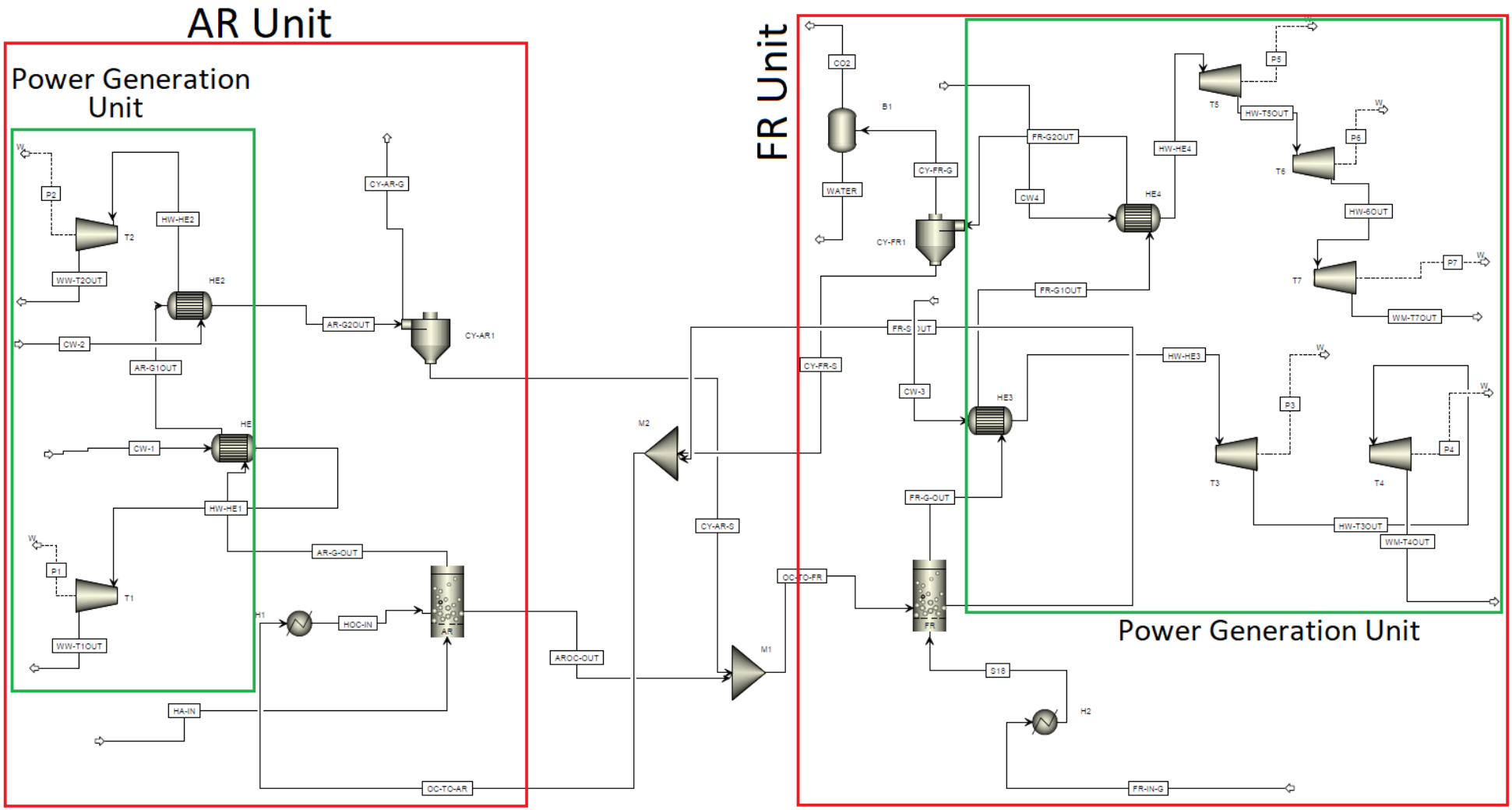

Fig. 5.1. Aspen Plus process flowsheet of the air reactor unit.

5.7. Results and Discussion

The effects of inlet molar flow, bimetallic carrier loading percentage, and inlet gas temperature on the conversion were investigated. The oxidation and combustion efficiency of AR and FR as well as power produced and consumed in this pilot plant study were also investigated and are discussed below.

5.7.1. Effect of inlet molar flow rates

The effect of air and methane inlet molar flow rates on the conversion is shown in Fig. 5.2.

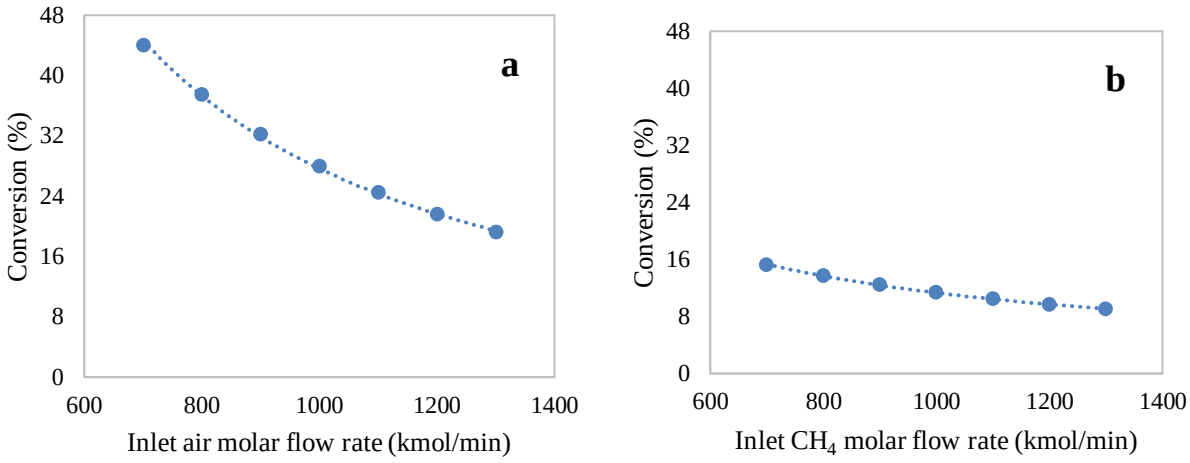

Fig. 5.2. Effect of inlet molar flows on conversion (a) AR, (b) FR.

The maximum conversion reported for the oxidation reaction was 44.05% at an inlet molar flow rate of 700 kmol/min. As the molar flow rate increased, conversion decreased. However, the inlet methane molar flow rate showed no significant effect on conversion. The maximum conversion was found to be 15.28%. As the methane molar flow rate increased from 700 kmol/min to 1300 kmol/min, conversion decreased from 15.28% to 9.03%. The decrease in conversion as the inlet molar mass flow rate increased was due to the residence time. As the molar flow rate of

either air or methane increased, the residence time decreased, meaning less time for reactants to spend in the reactor, which then led to decline of conversion.

5.7.2. Effect of bimetallic loading percentage on conversion

The effect of bimetallic loading percentage on oxidation and reduction reactions conversion is shown in Fig. 5.3. As the loading percentage of bimetallic precursor (Ni-Cu) deposited on support (ZrO_2) increased from 10-10/80 % to 35-35/30 %, an increase of around 39% in oxidation conversion was observed. However, no significant effect was observed of the loading percentage on the reduction reaction (around 0.098% increase), indicating independency of loading percentage on the conversion of methane. This independency was possibly due to the relative low operating temperature of the FR unit (990 K), which might hinder the conversion of the reduction reaction.

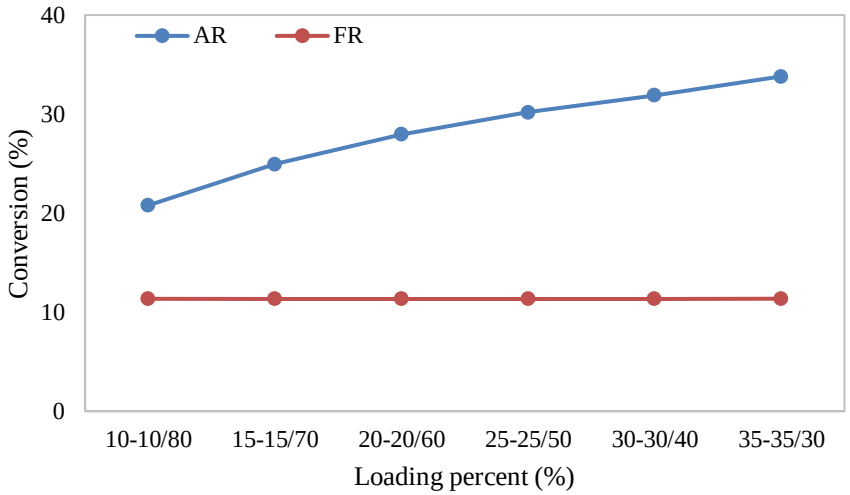

Fig. 5.3. Effect of loading percentage on conversion of AR and FR.

5.7.3. Effect of inlet gas temperature on conversion

The inlet gas temperature increased from 600K to 1100K to assess the effect of inlet gas temperature on the conversion of oxidation and reduction reactions. The results are shown in Fig. 5.4. A linear relationship was found between air and methane inlet temperatures and conversion. As the inlet gas temperature increased, conversion increased. The maximum reported conversions at 1100 K were found to be 38.89% and 11.59% for air and methane respectively. Although both oxidation and reduction reactions were exothermic, increasing the gas inlet temperature increased the conversion of both reactions, but with a greater increase of the oxidation reaction than the reduction reaction. This could indicate that the circulation rate of the solids was not limited by the reactor heat balance.

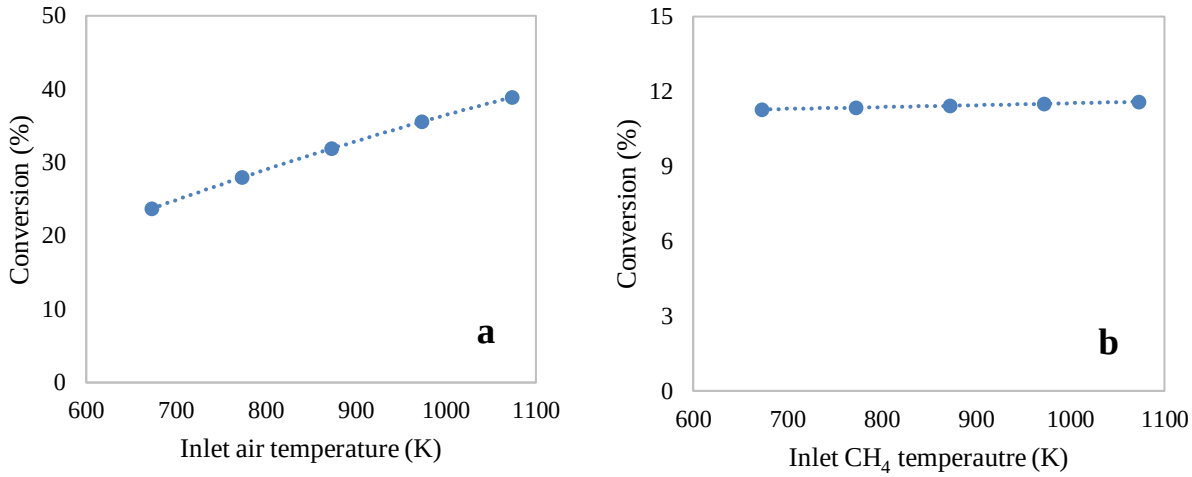

Fig. 5.4. Effect of inlet gas temperature on the conversion (a) AR, (b) FR.

5.7.4. Process efficiency and power analysis

The efficiency of the oxidation reaction and the reduction reaction (i.e. combustion) can be estimated using the following equations [24, modified]:

$$\eta_o \text{ or } \eta_c = \frac{F_{out} \sum(n_i \, x_{out,i})}{F_{in}(m_i \, x_{in,i})} \tag{5.15}$$

$$m = \sum n_i \tag{5.16}$$

where: η_o is the efficiency of oxidation (-), η_c is the efficiency of combustion (-), F_{in} and F_{out} are the molar flows at the inlet and outlet, respectively (kmol/min), n_i is the i^{th} component stoichiometry at the outlet (-), $x_{out,i}$ is the molar fraction of gas species i at the outlet (-), m_i is the i^{th} component stoichiometry at the inlet (-), and $x_{in,i}$ is the molar fraction of gas species i at the inlet (-).

The oxidation efficiency of the AR was found to be 67.82% where the combustion efficiency of FR was 15.14%. The higher oxidation efficiency suggests better heat removal from the AR than FR while maintaining the heat balance of the process.

The produced/consumed power of each unit in the pilot plant is summarized in Table 5.3.

Table 5.3 Pilot plant power production and consumption

	Net produced	Net consumed
AR unit (MW)	140	107.1
FR unit (MW)	325	304.8
Total (MW)	465	411.9
Process net duty (MW)	*-53.1*	

The net power produced by the pilot plant study was 53.1 MW, with 61.96% more power production in the AR unit. This result agreed with estimated AR and FR efficiency. The overall process efficiency of this study (CLC) was compared to the Combined Cycle Power Plant (CCPP) and Pulverized Coal (PC) power plants as shown in Fig. 5.5. The CLC power plant of this study showed very promising results as it reported 19.89% better efficiency compared to the CCPP power plant and 48.14% better efficiency than the Pulverized Coal power plant.

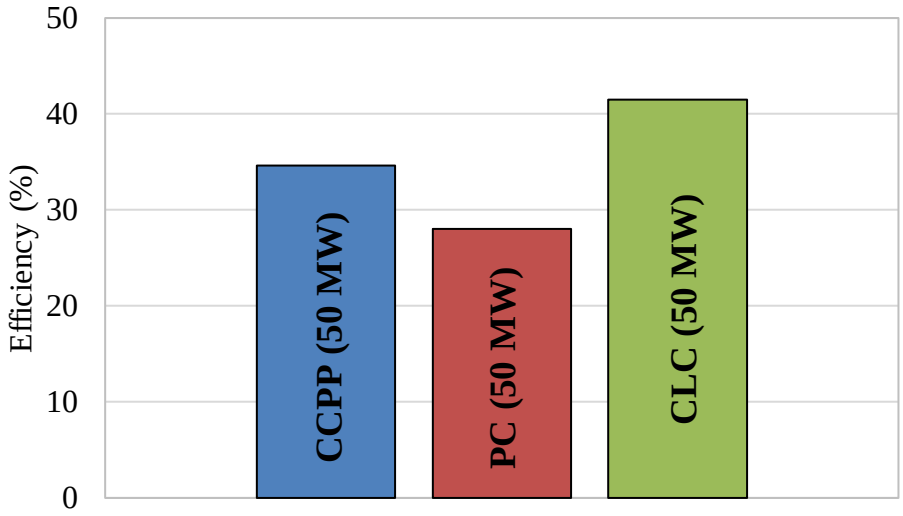

Fig. 5.5. Efficiency of CCPP [25], Pulverized Coal (PC) [26], and this study CLC power plants.

5.8. Conclusion

A pilot plant using the chemical looping process was investigated. Both AR and FR, as well as the hydrodynamics of circulating and bubbling fluidized-bed reactors, were studied and assessed to produce 50 MW of power. Assuming that the oxidation and reduction reactions as kinetically controlled, the increase of the inlet molar flows decreased the residence time and conversion of oxidation and reduction reactions. Moreover, independency of loading percentage on the conversion of methane was found. The actual power produced was 53.1 MW and the efficiency of the process was higher than the competing CCPP and PC power plant processes.

5.9. Acknowledgments

The authors wish to acknowledge the financial support provided by Canadian Natural Resources Limited (CNRL), Devon Corporation Canada, and the Natural Sciences and Engineering Research Council of Canada (NSERC). The authors would also like to acknowledge the financial support received from the Ministry of Education (MOE) in Saudi Arabia. Helpful discussion about Aspen Plus with Dr. Ehsan Mostafavi and Mr. Babak Labbaf is acknowledged and appreciated.

5.10. References

[1] Fan, J., Hong, H., Zhu, L., Jiang, Q., & Jin, H. (2017). Thermodynamic and environmental evaluation of biomass and coal co-fuelled gasification chemical looping combustion with CO_2 capture for combined cooling, heating and power production. Applied Energy, 195, 861-876.

[2] García-Labiano, F., Luis, F., Adánez, J., Abad, A., & Gayán, P. (2005). Temperature variations in the oxygen carrier particles during their reduction and oxidation in a chemical-looping combustion system. Chemical Engineering Science, 60(3), 851-862.

[3] Jung, J., & Gamwo, I. K. (2008). Multiphase CFD-based models for chemical looping combustion process: fuel reactor modeling. Powder Technology, 183(3), 401-409.

[4] Iliuta, I., Tahoces, R., Patience, G. S., Rifflart, S., & Luck, F. (2010). Chemical-looping combustion process: Kinetics and mathematical modeling. AIChE journal, 56(4), 1063-1079.

[5] Ryu, H. J., Bae, D. H., Han, K. H., Lee, S. Y., Jin, G. T., & Choi, J. H. (2001). Oxidation and reduction characteristics of oxygen carrier particles and reaction kinetics by unreacted core model. Korean Journal of Chemical Engineering, 18(6), 831-837.

[6] Porrazzo, R., White, G., & Ocone, R. (2016). Fuel reactor modelling for chemical looping combustion: From micro-scale to macro-scale. Fuel, 175, 87-98.

[7] Shuai, W., Huilin, L., Zhenhua, H., Feixiang, Z., Liyan, S., & Qinghong, Z. (2014). Modeling of reactive gas–solid flows in riser reactors using a multi-scale chemical reaction model. Chemical Engineering Science, 116, 773-780.

[8] Iloeje, C., Zhao, Z., & Ghoniem, A. F. (2015). Analysis of thermally coupled chemical looping combustion-based power plants with carbon capture. International Journal of Greenhouse Gas Control, 35, 56-70.

[9] Porrazzo, R., White, G., & Ocone, R. (2014). Aspen Plus simulations of fluidised beds for chemical looping combustion. Fuel, 136, 46-56.

[10] Haus, J., Hartge, E. U., Heinrich, S., & Werther, J. (2017). Dynamic flowsheet simulation of gas and solids flows in a system of coupled fluidized bed reactors for chemical looping combustion. Powder Technology, 316, 628-640.

[11] Hartge, E. U., Luecke, K., & Werther, J. (1999). The role of mixing in the performance of CFB reactors. Chemical engineering science, 54(22), 5393-5407.

[12] Jafari, R., Sotudeh-Gharebagh, R., & Mostoufi, N. (2004). Modular simulation of fluidized bed reactors. Chemical engineering & technology, 27(2), 123-129.

[13] Meng, W. X., Banerjee, S., Zhang, X., & Agarwal, R. K. (2015). Process simulation of multi-stage chemical-looping combustion using Aspen Plus. Energy, 90, 1869-1877.

[14] Puettmann, A., Hartge, E. U., & Werther, J. (2012). Application of the flowsheet simulation concept to fluidized bed reactor modeling. Part II—Application to the selective oxidation of n-butane to maleic anhydride in a riser/regenerator system. Chemical Engineering and Processing: Process Intensification, 57, 86-95.

[15] Hassan, B., Ogidiama, O. V., Khan, M. N., & Shamim, T. (2017). Energy and exergy analyses of a power plant with carbon dioxide capture using multistage chemical looping combustion. Journal of Energy Resources Technology, 139(3), 032002.

[16] Ohlemüller, P., Alobaid, F., Gunnarsson, A., Ströhle, J., & Epple, B. (2015). Development of a process model for coal chemical looping combustion and validation against 100kWth tests. Applied Energy, 157, 433-448.

[17] Sotudeh-Gharebaagh, R., Legros, R., Chaouki, J., & Paris, J. (1998). Simulation of circulating fluidized bed reactors using ASPEN PLUS. Fuel, 77(4), 327-337.

[18] Peltola, P., Ritvanen, J., Tynjälä, T., & Hyppänen, T. (2013). Model-based evaluation of a chemical looping combustion plant for energy generation at a pre-commercial scale of 100MWth. Energy conversion and management, 76, 323-331.

[19] Wang, J., & Fu, C. (2016). Thermodynamic analysis of a solar-hybrid trigeneration system integrated with methane chemical-looping combustion. Energy Conversion and Management, 117, 241-250.

[20] Wen, C. Y., & Yu, Y. H. (1966). A generalized method for predicting the minimum fluidization velocity. AIChE Journal, 12(3), 610-612.

[21] Fogler, H. S., & Brown, L. F. (1981). Reactors. In ACS Symp. Ser (Vol. 168, pp. 31-75).

[22] Lyngfelt, A., Leckner, B., & Mattisson, T. (2001). A fluidized-bed combustion process with inherent CO_2 separation; application of chemical-looping combustion. Chemical Engineering Science, 56(10), 3101-3113.

[23] Tijani, M. M., Aqsha, A., Yu, N., & Mahinpey, N. (2018). Determination of redox pathways of supported bimetallic oxygen carriers in a methane fuelled chemical looping combustion system. Fuel, 233, 133-145.

[24] Wang, S., Lu, H. L., Tang, Y., & Li, D. (2013). Modeling of a Chemical Looping Combustion Process in Interconnected Fluidized Beds with a Cu-Based Oxygen Carrier. Chemical Engineering & Technology, 36(9), 1503-1510.

[25] Ramakrishnan, K. (2014). Optimization and Process modelling of Municipal Solid Waste using Plasma Gasification for Power Generation in Trichy, India.

[26] Gonzalez-Salazar, M. A., Kirsten, T., & Prchlik, L. (2017). Review of the operational flexibility and emissions of gas-and coal-fired power plants in a future with growing renewables. Renewable and Sustainable Energy Reviews, 82(1), 1497-1513.

CHAPTER SIX: Conclusions and recommendations for future work

6.1. Conclusions

The main objective of this work was to synthesize chemically and thermally stable oxygen carriers for the chemical looping combustion process in order to study the viability of a pilot plant to produce clean power without emitting carbon dioxide to the atmosphere. To achieve this objective, the study was divided into four different parts. In the first part, synthesis of supported monometallic oxygen carriers was conducted, examining the effect of different operating conditions on the reactivity of oxygen carriers (redox reactions) using the thermogravimetric analyzer (TGA).

The second part applied and considered the optimum operating conditions obtained from part 1 as well as the interpretation of phase changes. The synthesis of supported bimetallic oxygen carriers was carried out. The reactivity of carriers such as oxygen capacity, surface area, phases during the redox reaction, and intrinsic and global kinetics were investigated.

The third part consisted of constructing and examining the methane CLC process in terms of kinetics and thermodynamics to obtain information needed to scale up the process. A micro reactor system was used to investigate use of a nickel-based oxygen carrier for the methane CLC process. Issues found in parts 1 and 2 such as carbon deposition, formation of intermediate phases and mass transfer effects on kinetics were addressed and assessed.

The final part of the thesis discussed a case study for the scale-up of the methane CLC process using Aspen Plus computer software. A complete process flowsheet was constructed and examined using experimental and modelling information obtained from parts 2 and 3. The hydrodynamics, kinetics, and power production were investigated in order to assess the feasibility of using supported bimetallic oxygen carriers for the methane CLC process. The effects of entering

flows, temperature, and metal loading percentage on the conversion of air (air reactor) and methane (fuel reactor) were explored. Overall process efficiency was estimated and compared to the competing CCPP and PC power production plants.

From the above-mentioned studies, several specific conclusions were made:

- The use of supported monometallic oxygen carriers resulted in interaction between active-sites and supports to form intermediates such as $CoAl_2O_4$ and $NiAl_2O_4$.
- The oxidation reaction of all samples was exothermic because the rate decreased with increasing the reaction temperature (800-^{o}C950^{o}C), while the reduction reaction was endothermic because as the reaction temperature increased (800-^{o}C950^{o}C), the rate increased.
- The reaction temperature between 900°C and 950°C showed the highest oxygen capacity among all tested reaction temperatures.
- Supported bimetallic complexes formed after the reduction reaction among precursors with weak chemical stability. This was shown to reduce the reactivity of supported bimetallic carriers due to their interaction with supports.
- The reactivity of supported bimetallic carriers remained stable once the chemical stability between precursors maximized.
- The supported bimetallic Ni-Co/ZrO_2, Ni-Cu/ZrO_2, and Ni-Fe/ZrO_2 samples showed stable oxygen capacities when the reaction temperature varied, and no noticeable interaction between precursors and supports observed.
- The maximum obtainable conversion for the methane CLC process using RGibbs micro-reactor was 99.44% with noticeable formation of intermediates (i.e. H_2 and CO).

- As the entering molar flows increased, the methane conversion decreased by 50%; however, no formation of intermediates was observed using a set of non-catalytic gas-solid reactions.
- For the case study to produce 50 MW of power, the increases in the entering molar flows resulted in less residence time for reactants inside the reactor, which reduced the conversion in both reactors (i.e. air and fuel reactors). As the metal loading percentage increased, the conversion in the air reactor increased; however, independency of the metal loading percentage on the conversion of the fuel reactor was observed.
- The case study of the methane CLC pilot plant process had an overall efficiency of 41.48% while the other reported efficiencies for CCPP and PC power plants were 34.60% and 28%, respectively.

6.2. Recommendations for future work

Recommendation for future work include:

1) Pelletization of the synthesized oxygen carriers is an important parameter to test and assess. Mass transfer may become significant when the oxygen carriers are pelletized; therefore, additional mass transfer study should be undertaken.
2) Methane was used to research the CLC process in this study. Natural gas could be used instead to study the effect of other gases present along with methane. For example, the deactivation rate of oxygen carriers can be studied for natural gas since most natural gas sources produce natural gas with a small percentage of sulfur.
3) Bench-scale experiments should be conducted to help address possible challenges such as pressure drops and hotspots in both air and fuel reactor units.

4) A gas analyzer unit coupled with the thermogravimetric analyzer (TGA) can be used to estimate and determine the rate of gases evolved during the CLC redox reaction. This can help in evaluating the rate of consumption/production of intermediates and final product of gases.
5) Integration of the CLC process with others such as carbon conversion or syngas production may help in optimizing both processes and possibly gaining more profits.
6) It would be interesting to find out what is the effect of bi- and tri-support combinations on the redox reaction, formation of carbon, and stability of the synthesized oxygen carriers.
7) The fluidization properties of the synthesized oxygen carriers are a point of interest. The attrition index, sintering, and agglomeration of particles can be tested or assessed for both powder-like and pelletized oxygen carriers.

APPENDIX A: Uncertainty analysis for experiments

Various lab instruments were used in this study, including but not limited to: TGA, XRD, H_2-TPR, BET, weight balances, and BET. Each type of equipment produces uncertainty in measurement, which can be called the measurement/instrumental error. Another source of error found is associated with data analysis using different theories with their assumptions. The main instrument used in this study was the TGA. The TGA was calibrated before any experiment was conducted, using the technique of melting point of different metals to calibrate the thermocouple. The error found with measuring the temperature was ± 1°C. The instrumental errors of other equipment (i.e. XRD, H_2-TPR) were obtained and found to be around 1-2%. The balances used in this study were calibrated and then a reference balance was used to calculate the measurement error, which was found to be ± 0.022 g. The BET instrument used in this study was only able to estimate the error associated with the data analysis, which was less than 1% for all samples tested. The measurement error in this study was estimated using the following formula:

$$SE_{\bar{x}} = \sigma/\sqrt{n} \tag{A.1}$$

where; $SE_{\bar{x}}$ is the standard error of the mean [-], σ is the sample standard deviation [-], n is the number of repetition [-].

Each experimental run was at least duplicated (unless stated) to get insight about the experimental errors associated with the equipment.

The error associated with estimating the kinetic parameters (E_A & k_0) in this study was calculated using the non-linear least square method, which was a built-in function in MATLAB computer software. The error was found to be 23% - 13% with 95% confidence level.

APPENDIX B: Details about how the kinetics parameters estimated in Chapters 2 and 3

The steps involved in estimating the kinetic parameters of the TGA raw data are as follows:

1) Calculations of conversion (X), reaction rate (dX/dt), and the shrinking core model rate of reaction. Equation 2.3 used to calculate the rate (dX/dt), and the shrinking core model term ($(1-X)^{2/3}$).

Table B.1 Calculations of the TGA raw data

TGA time (min)	TGA mass (mg)	Reaction time (min)	X (-)	rate (dX/dt)	$(1-X)^{2/3}$
16	9.912466576	0	0	0	1
16.5	9.870185477	0.5	0.701409213	0.418060936	0.446735984
17	9.857585076	1	0.910439681	0.104718242	0.200175269
17.5	9.854428856	1.5	0.962798802	0.042394817	0.11143919
18	9.853151072	2	0.983996211	0.032007579	0.063506067
18.5	9.85218636	2.5	1	0	0
19	9.85218636	3	1	0	0
19.5	9.85218636	3.5	1	0	0
20	9.85218636	4	1	0	0
20.5	9.85218636	4.5	1	0	0
21	9.85218636	5	1	0	0
21.5	9.85218636	5.5	1	0	0
22	9.85218636	6	1	0	0
22.5	9.85218636	6.5	1	0	0
23	9.85218636	7	1	0	0
23.5	9.85218636	7.5	1	0	0
24	9.85218636	8	1	0	0
24.5	9.85218636	8.5	1	0	0
25	9.85218636	9	1	0	0
25.5	9.85218636	10	0	0	0

2) Plotting of rate (dX/dt) versus the shrinking core model term $(1-X)^{2/3}$ gives the intercept (k_{scm}) at the giving reaction temperature (Fig. B.1). Repetition for all reaction

temperatures was carried out, and a summary of the rate constant at all temperatures is shown in Table B. 2.

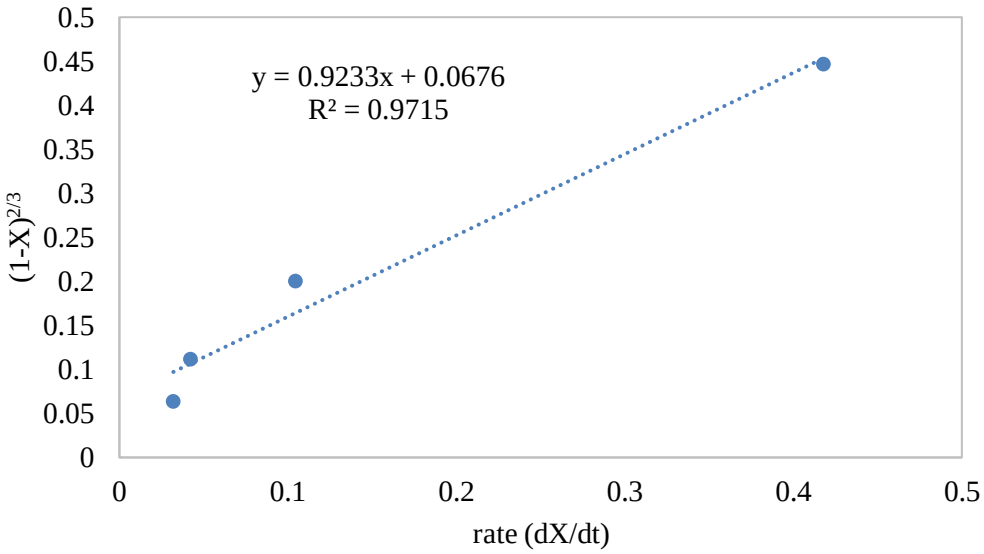

Fig. B.1. Reaction rate versus $(1\text{-}X)^{2/3}$) in the shrinking core model.

Table B.2 Summary of the reaction rate constant at different temperatures

Temperature (^{o}C)	kscm	1/T	ln(kscm)
800	0.9233	0.00093184	-0.0798011
850	0.9659	0.00089035	-0.0346743
900	0.9806	0.00085241	-0.0195906
950	0.9955	0.00081756	-0.0045302

3) Finally, using the Arrhenius equation (Eq. 2.5), the kinetic parameters were obtained by plotting ln(kscm) versus (1/T) as it is shown in Fig. B.2. The slope represented the $\left(-\frac{E}{RT}\right)$ term and the intercept represented the $\ln(k_0)$ term.

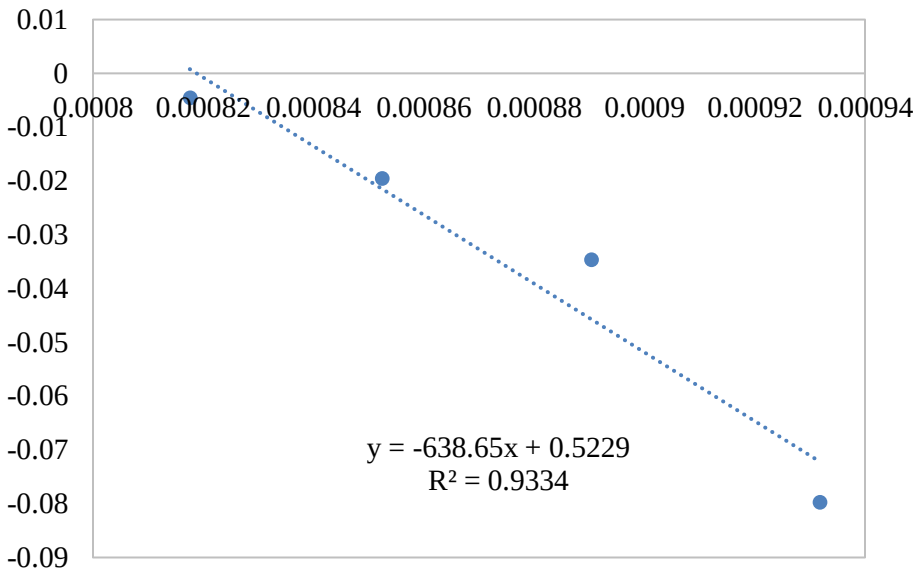

Fig. B.2. Plot of ln(k_{scm}) versus the reciprocal of temperature.

APPENDIX C: Polymath (v6.1) code used in chapters three and five calculations

```
pi(min) = 0
pi(max) = 50
f(pi) = ((3/(pi^2))*(pi*coth(pi-1)))-eta
pi(0) = 1
eta = 1
```

```
f(ut) = ut-((1.78E-2)*(eta^2)/(rhog*mu))^(1/3)*dp
ut(0) = 0.01
ut(min) = 0
ut(max) = 10
eta= g*(rhos-rhog)
g=9.81
dp=0.001
rhos=4966
rhog=1.205
Re=(rhog*dp*ut)/mu
mu=1.10E-5
```

```
f(ut) = ut-((4*g*dp*(Re^b1))/(3*a1))*((rhos/rhog)^(1/2))
ut(0) = 0.1
ut(min) = 0
ut(max) = 100
g=9.81
dp=0.000401
rhos=4966
rhog=1.1839
Re=(rhog*dp*ut)/mu
mu=0.0000394
a1=24
b1=1
```

APPENDIX D: License to reprint

D.1 License to reprint and reuse Chapter 2

Copyright Clearance Center RightsLink®

Home | Create Account | Help

Title: Synthesis and study of metal-based oxygen carriers (Cu, Co, Fe, Ni) and their interaction with supported metal oxides (Al2O3, CeO2, TiO2, ZrO2) in a chemical looping combustion system

Author: Mansour Mohammedramadan Tijani,Aqsha Aqsha,Nader Mahinpey

Publication: Energy

Publisher: Elsevier

Date: 1 November 2017

LOGIN

If you're a copyright.com user, you can login to RightsLink using your copyright.com credentials.

Already a RightsLink user or want to learn more?

Quick Price Estimate

I would like to...	reuse in a thesis/dissertation
I would like to use...	full article
My format is...	both print and electronic
I am the author of this Elsevier article...	Yes
I will be translating...	No
My currency is...	CAD - $
Quick Price	Click Quick Price

QUICK PRICE CONTINUE

This service provides permission for reuse only. If you do not have a copy of the content, you may be able to purchase a copy using RightsLink as an additional transaction. Simply select 'I would like to..... 'Purchase this content'.

Unclear about who you are?

Exchange rates under license from XE.com.
To request permission for a type of use not listed, please contact Elsevier Global Rights Department.

Are you the author of this Elsevier journal article?

D.2 License to reprint and reuse Chapter 3

Copyright Clearance Center RightsLink®

Home | Create Account | Help

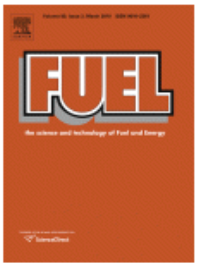

Title: Determination of redox pathways of supported bimetallic oxygen carriers in a methane fuelled chemical looping combustion system

Author: Mansour Mohammedramadan Tijani,Aqsha Aqsha,Ningyu Yu,Nader Mahinpey

Publication: Fuel

Publisher: Elsevier

Date: 1 December 2018

LOGIN

If you're a copyright.com user, you can login to RightsLink using your copyright.com credentials.

Already a RightsLink user or want to learn more?

Quick Price Estimate

I would like to...	reuse in a thesis/dissertation
I would like to use...	full article
My format is...	both print and electronic
I am the author of this Elsevier article...	Yes
I will be translating...	No
My currency is...	CAD - $
Quick Price	Click Quick Price

QUICK PRICE | CONTINUE

This service provides permission for reuse only. If you do not have a copy of the content, you may be able to purchase a copy using RightsLink as an additional transaction. Simply select 'I would like to..... 'Purchase this content'.

Unclear about who you are?

Exchange rates under license from XE.com.
To request permission for a type of use not listed, please contact Elsevier Global Rights Department.

Are you the author of this Elsevier journal article?